IMPACT OF CONVECTION AND LIGHTNING ON THE TROPOSPHERIC CHEMISTRY COMPOSITION OVER NORTH AMERICA AND AIR QUALITY STUDIES OVER EAST ASIA

A Dissertation
Presented to
The Academic Faculty

by

Chun Zhao

In Partial Fulfillment
of the Requirements for the Degree
Doctor of Philosophy in the
School of Earth and Atmospheric Sciences

Georgia Institute of Technology
May 2009

IMPACT OF CONVECTION AND LIGHTNING ON THE TROPOSPHERIC CHEMISTRY COMPOSITION OVER NORTH AMERICA AND AIR QUALITY STUDIES OVER EAST ASIA

Approved by:

Dr. Yuhang Wang, Advisor
School of Earth and Atmospheric Sciences
Georgia Institute of Technology

Dr. Athanasios Nenes
School of Earth and Atmospheric Sciences
Georgia Institute of Technology

Dr. Judith Curry
School of Earth and Atmospheric Sciences
Georgia Institute of Technology

Dr. Armistead (Ted) Russell
School of Civil and Environmental Engineering
Georgia Institute of Technology

Dr. Greg Huey
School of Earth and Atmospheric Sciences
Georgia Institute of Technology

Date Approved: 03-25-2009

To my wife, Xiaohui

ACKNOWLEDGEMENTS

I deeply appreciate the tremendous support that I have received from many individuals during the process of obtaining my Ph.D. I thank my advisor, Dr. Yuhang Wang, for his long-term support and guidance with his scientific enthusiasm. My group members, Dr. Tao Zeng, Dr. Junsang Nam, Dr. Qing Yang, Dasa Gu, Burton Gray, Sunny Choi, Zhen Liu, Ja-ho Koo, and Charles Smeltzer gave me great encouragement and valuable suggestions. I thank Dr. Judith Curry, Dr. Greg Huey, Dr. Athanasios Nenes, and Dr. Armistead Russell for their taking time to serve on my thesis committee and for helpful discussions. My research has also been assisted by Dr. Armistead Russell, Dr. Yongtao Hu, Dr. Yunsoo Choi, Dr. Randall Martin, Dr. Rong Fu, Dr. Ming Luo, Dr. John Kain and many others. I also thank numerous former and current colleagues and friends at EAS Georgia Tech, particularly, Dr. Wei Liu, Dr. Changsub Shim, Dr. Yasuko Yoshida, Dr. Yan Huang, Dr. Wenhong Li, Peng Zhao, Bo Yan, Zhijun Zhao, Jin Liao, and Wenxian Zhang. I thank Dr. Yunfei Fu at the University of Science and Technology of China for leading me to the scientific field. Above all, I have been supported by the tremendous love of my family: my wife, Xiaohui Ge, my parents, my in-laws. Finally, my deep appreciation goes to my church family for their spiritual encouragement and support throughout the completion of my study.

While writing this Acknowledgement, I have thought about the thousands of hours I have spent researching, debugging, plotting, writing, and preparing this thesis. I enjoyed every minute and the knowledge gained. The degree earned will be a sufficient reward for the endeavor.

TABLE OF CONTENTS

LIST OF TABLES

LIST OF FIGURES

Page

LIST OF SYMBOLS AND ABBREVIATIONS

Symbols

E	A posteriori NO_x emissions
E_a	A priori NO_x emission
E_t	Top-down NO_x emissions
E_{priori}^{fuel}	A priori fossil fuel NO_x emission
E_{priori}^{soils}	A priori soil NO_x emission
ε	Relative error of E
ε_a	Relative error of E_a
ε_t	Relative error of E_t

Abbreviation

AK	Averaging kernel
ASDC	Atmospheric Science Data Center
CAPE	Convective available potential energy
CG	Cloud-to-ground
CO	Carbon monoxide
CTM	Chemical transport model
C_2H_6	Ethane
C_3H_8	Propane
DAAC	Distributed Active Archive Center
DAO	Data Assimilation Office
DFS	Degree of freedom
DOAS	Differential Optical Absorption Spectroscopy

EANET	Acid Deposition Monitoring Network in East Asia
EPA	Environmental Protection Agency
FDDA	Four-dimensional data assimilation
GEIA	Global Emissions Inventory Activity
GEOS-Chem	Global Goddard Earth Observing System – Chemistry (model)
GEOS-4 or 5	GEOS assimilated meteorological fields
GES-DISC	Goddard Earth Sciences Data and Information Services Center
GFED	Global Fire Emissions Database
GOES	Geostationary Satellite Server
GOME	Global Ozone Monitoring Experiment
GPCP	Global Precipitation Climatology Project
GSFC	Goddard Space Flight Center
HNO_3	Nitric acid
hPa	Hecto Pascal
IC	Intracloud
INTEX-NA	Intercontinental Chemical Transport Experiment-North America
INTEX-B	Intercontinental Chemical Transport Experiment (Phase B)
IPCC	Intergovernmental Panel on Climate Change
ISCCP	International Satellite Cloud Climatology Project
ITCZ	Intercontinental Transport and Chemical Transformation
MDA8	Maximum daily 8-hour average
MGLY	Methylglyoxal
MLS	Microwave Limb Sounder
MM5	Fifth-Generation NCAR/Penn State Mesoscale Model
MODIS	Moderate Resolution Imaging Spectroradiometer

MOPITT	Measurement of Pollution in the Troposphere
MYJ	Mellor-Yamada-Janjic
NCAR	National Center for Atmospheric Research
NCEP	National Center Environmental Prediction
NEI99	EPA 1999 National Emission Inventory
NLDN	National Lightning Detection Network
NMHC	Non-methane hydrocarbon
NNRP	NCEP/NCAR reanalysis product
NO	Nitric oxide
NO2	Nitrogen dioxide
NOx	Nitrogen oxides (NO+NO2)
NRT	Near Real Time
OH	Hydroxyl radical
O3	Ozone
OMI	Ozone Monitoring Instrument
Pa	Pascal
PAN	Peroxyacetyle nitrate
PBL	Periodic boundary layer
ppbv	Parts per billion by volume
pptv	Parts per trillion by volume
PV	Potential vorticity
REAM	Regional chEmical trAnsport Model
SAGE	Stratospheric Aerosol and Gas Experiment
SCIAMACHY	SCanning Imaging Absorption spectrometer for Atmospheric CHartographY

SMOKE	Sparse Matrix Operator Kernel Emissions model
SONEX	SASS (Subsonic Assessment) Ozone and NO_x Experiment
TES	Tropospheric Emission Spectormeter
3-D	Three-dimensional
TOMS	Total Ozone Mapping Spectrometer
UT	upper troposphere
VISTAS	Visibility Improvement of State and Tribal Association of the Southeast
VOCs	Volatile organic compounds
UMF	Updraft mass flux
WRF	Weather Research Forecasting model

SUMMARY

A Regional chEmical trAnsport Model (REAM) was developed and applied to study several critical meteorological factors and anthropogenic emissions contributing to the spatial distribution of air pollutants in the troposphere over North America and East Asia, two of the biggest polluted regions in the world. We used diverse satellite measurements as well as in-situ surface and aircraft measurements. The REAM model was applied over North America to examine the uncertainties in modeling the effect of convective transport and lightning NO_x production on upper tropospheric chemical tracer distributions. To assess the model uncertainties, two different cumulus convective parameterizations, KF-eta and Grell, were incorporated into REAM from the meteorological models, WRF and MM5, respectively. The KF-eta scheme in WRF-REAM, which includes entrainment and detrainment processes, produces more outflows of pollutants in the mid-troposphere and more efficient scavenging of soluble HNO_3 in the free troposphere than the Grell scheme in MM5-REAM. Consequently, the results from WRF-REAM are in closer agreement with aircraft measurements. The inclusion of entrainment and detrainment processes in the KF-eta scheme also partly leads to lower cloud top heights (10-12 km in WRF versus up to 16 km in MM5), in better agreement with GOES satellite measurements, and hence smaller amounts of estimated lightning NO_x and lower emission altitudes. Both models suggest that lightning NO_x production enhances the concentration of upper tropospheric NO_2 by a factor of > 5 (~100 pptv) and increases O_3 by up to ~20 ppbv.

East Asia, in particular China, contributes significantly to the global NO_x budget. NO_x emission inventories over China, based on the bottom-up approach, are thought to be quite uncertain. Assimilated inversion on a daily basis using OMI tropospheric NO_2 columns was developed and applied in the REAM model to constrain fossil fuel NO_x emissions over East Asia. The iterative nature of the assimilated inversion improves upon the widely-used monthly-mean inversion by accounting for the chemical feedbacks of changed NO_x emissions and reducing the dependence of the a priori emissions. The derived fossil fuel NO_x emission inventory shows that rapid economic growth associated pollutant emissions in China are concentrated over three connected plains in the east, which could generate a large amount of O_3 pollutant. We analyzed an observed episode (June 9-14, 2004) of highly elevated O_3 concentrations over East China using the REAM model. During this episode, the high-O_3 region extended over an area > 1 million km^2, which hosts a population of > 800 million people. Model results indicate that controlling anthropogenic NO_x emissions effectively reduces the area of high-ozone exposure. However, this convergence of O_3 over the East China plains occurs mostly in the late spring and early summer before the onset of the East Asian summer monsoon. During the summer monsoon season, the pollutant levels are largely limited. Diverse satellite measurements from May to August 2006 were analyzed using the REAM model to investigate the impact of the East Asian summer monsoon on the air quality over China. The observed migration of O_3 and CO indicate that the summer monsoon significantly affects the air quality over the southeastern China and that the influence extends to the central East China from June to July. Regions with enhancements of CO and O_3 over the southeastern China disappear after the onset of the summer monsoon and re-emerge in

August after the monsoon wanes. Pre-monsoon high O_3 concentrations over the southern China are due to photochemical production from pollutant emissions and transport from the stratosphere. Model results suggest that transport from the stratosphere and long-range transport from East China and South/Central Asia all make significant contributions to O_3 over West China.

CHAPTER 1

INTRODUCTION

1.1 Overview

Distributions of air pollutants and their precursors in the troposphere are driven largely by meteorological conditions (e.g., wind, cloud convection, lightning, and precipitation) and emissions such as those of NO_x from anthropogenic sources (e.g., fossil fuel combustion) and natural sources (e.g., soil and lightning). As the top two most polluted regions in the world, East Asia and North America significantly contribute to climate change on both regional and global scales. Therefore, it is necessary to investigate the vertical and horizontal distributions of the air pollutants in the troposphere over these two regions to better quantify the interaction between air pollution and climate change, which remains until now largely uninvestigated [IPCC, 2007].

1.1.1 Impact of convection and lighting NO_x production on the distribution of tropospheric chemical tracers over North America

Convection and associated lightning NO_x production are two important meteorological processes affecting the production and distribution of tropospheric chemical tracers [e.g, Y. Wang et al., 2001; Doherty et al., 2005; Hudman et al., 2007; Choi et al., 2005, 2008a]. Convection redistributes trace gases vertically and significantly affects atmospheric chemical and transport processes during long-range transport [e.g., Y. Wang et al., 2000, 2001; Doherty et al., 2005; Hess, 2005; Folkins et al., 2006; Kiley et al., 2006; Hudman et al., 2007]. Q. Li et al. [2005] and Choi et al. [2008b] showed the importance of convection in ventilating air pollutants from the continental boundary layer

of the United States (US) and providing a conduit for US pollution to the West Atlantic Ocean.

Lightning is a major source of NO_x (NO_2+NO) in the upper troposphere. NO_x is thought to be produced during the return stroke stage of a cloud-to-ground flash and the leader stage of an intra-cloud flash [e.g., Price et al., 1997]. Lightning NO_x significantly enhances tropospheric NO_2 columns, particularly over the ocean, where NO_2 columns are more sensitive to lightning NO_x production due to the less impact of surface NO_x emissions [e.g., Choi et al. 2005, 2008a; Martin et al., 2006; Bertram et al., 2007]. It also increases the concentrations of O_3 and PAN in the free troposphere [e.g., Labrador et al., 2004; Hudman et al., 2007].

1.1.2 Air pollution over East Asia

During the past two decades, the rapid economic growth in China has resulted in a significant increase in the emissions of pollutants and their precursors over East Asia [e.g., Streets et al., 2000, 2003; Richter et al., 2005]. These emissions lead to the enhancement of the regional greenhouse effect and elevated pollutant concentrations near the surface (e.g., NO_x and O_3) [IPCC, 2007].

Mainly originating from fossil fuel combustion, lightning, and soils emissions, NO_x is a major pollutant in the troposphere and plays a key role in tropospheric chemistry. A surface NO_x emission inventory is widely developed either using the bottom-up approach, which uses compilations of emission statistics and source factors, or using the top-down approach, based on the satellite measured tropospheric NO_2 columns [e.g., Streets et al., 2003; Martin et al., 2006]. Recently, both approaches found that the anthropogenic NO_x emissions over China keep increasing at an annual rate of 6-10% over

the last decade [e.g., Richter et al., 2005; Zhang et al., 2007; Stavrakou et al., 2008]. Because of the large amount of the anthropogenic NO_x emissions, high O_3 episodes have been observed more and more frequently in China, mostly over East China. East China hosts the economic engine of the country with > 60% of the industry and population and most of the major cities (110-120^{o}E, 25-42^o N) [e.g., Lam et al., 2001; Ma et al., 2002; Gao et al., 2005; Z. Wang et al., 2006; H. Wang et al., 2006].

However, the convergence of pollutants (e.g., O_3 and CO) driven by the anthropogenic emissions over the East China plains occurs mostly in the late spring and early summer before the onset of the East Asian summer monsoon. In East Asia, summer monsoon is a major atmospheric system affecting air-mass transport, convection, and precipitation [Hoskins and Rodwell, 1995; Rodwell and Hoskins, 2001; Ding et al., 2005]. Surface observations in limited locations showed that the ground O_3 levels over East China could be strongly perturbed by the monsoonal flow with clean oceanic air-mass transported from the tropical Pacific in summer [e.g., Tanimoto et al., 2005; Z. Wang et al., 2006; J. Li et al, 2007]. Tanimoto et al. [2005] indicated that exchanges between continental and oceanic air masses driven by the East Asian summer monsoon play a central role in producing the summer minimum of surface O_3 over East Asia and the latitudinal differences in O_3 seasonality observed at the Acid Deposition Monitoring Network in East Asia (EANET) sites. Recently, diverse satellite measurements also showed that the East Asian monsoon largely affects the chemical composition of the troposphere on continental and regional scales [e.g., Randel and Park, 2006; Fu et al., 2006; Jiang et al., 2007; Park et al., 2007].

1.2 Scope of this work

The objectives of this study are four-fold: 1) to assess the uncertainties in modeling the impact of convection and lighting processes on the production and distribution of tropospheric chemical tracers over North America; 2) to constrain the surface NO_x emissions over East Asia with satellite measurements using a new assimilated inversion method; 3) to examine the significance of the ground O_3 pollution over China and its potential controlling effect; 4) to investigate the impact of the East Asian summer monsoon on the air quality over China. A Regional chEmical trAnsport Model (REAM) was developed and applied to accomplish these objectives along with diverse satellite measurements as well as in-situ surface and aircraft measurements.

In this thesis, each research objective or project is presented as a separate chapter.

Chapter 2 presents the **Impact of Convective Transport and Lightning NO_x Production over North America: Dependence on Cumulus Parameterizations.** The uncertainty in modeling convection and lightning parameterizations were assessed using two different cumulus convective schemes, KF-eta and Grell, incorporated into REAM from the meteorological models, WRF and MM5, respectively. The associated lightning NO_x production is parameterized in the two schemes respectively as well.

Chapter 3 is entitled **Assimilated Inversion of NO_x Emissions over East Asia using OMI NO_2 Column Measurements.** Assimilated inversion on a daily basis was developed and implemented in the REAM model using OMI tropospheric NO_2 columns to constrain fossil fuel NO_x emissions over East Asia.

Chapter 4 describes work on **East China Plains: A "basin" of Ozone Pollution.** Episodes of highly elevated ozone over East China were analyzed using the REAM

model to identify the feature of the ozone pollution and its potential controlling effect over China.

Chapter 5 investigates **The Impact of the East Asian Summer Monsoon on the Air Quality over China: The view from space.** Tropospheric O_3 and CO concentrations retrieved from diverse satellite measurements were analyzed using the REAM model to investigate the impact of the East Asian summer monsoon on the air quality over China.

And **Chapter 6: Summary and Future Research** presents the summary and main findings of this work and recommendations for future research.

CHAPTER 2

[1]IMPACT OF CONVECTIVE TRANSPORT AND LIGHTNING NOX PRODUCTION OVER NORTH AMERICA: DEPENDENCE ON CUMULUS PARAMETERIZATIONS

2.1 Introduction

Tropospheric distributions of trace gases are driven in part by meteorological conditions. Convection and associated lightning NO_x production are two important meteorological processes affecting the production and distribution of tropospheric chemical tracers [e.g, Y. Wang et al., 2001; Doherty et al., 2005; Hudman et al., 2007; Choi et al., 2005, 2008a]. Convection redistributes trace gases vertically and significantly affects atmospheric chemical and transport processes during long-range transport [e.g., Y. Wang et al., 2000, 2001; Doherty et al., 2005; Hess, 2005; Folkins et al., 2006; Kiley et al., 2006; Hudman et al., 2007]. Q. Li et al. [2005] and Choi et al. [2008b] showed the importance of convection in ventilating air pollutants from the continental boundary layer of the United States (US) and providing a conduit for US pollution to the West Atlantic Ocean.

Simulations of convective transport have large uncertainties. Several studies found substantial divergences among Chemical Transport Model (CTM) simulations

---

[1] This Chapter is for "Impact of convective transport and lightning NO_x production over North America: Dependence on cumulus parameterizations" published at Atmospheric Chemistry and Physics Discussion in 2009. Authors are C. Zhao, Y. Wang, Y. Choi, and T. Zeng.

arising from the difference in various cumulus parameterizations [e.g., Prather and Jacob, 1997; Prather et al., 2001; Collins et al., 2002; Doherty et al., 2005]. To properly evaluate model simulations of convective transport and lightning NO_x production, extensive atmospheric measurements are needed. One such dataset is the Intercontinental Chemical Transport Experiment – North America (INTEX-NA) collected during summer (July 3 to August 15) 2004 over North America [Singh et al., 2006], in which a large number of cases for active convection and large amounts of lightning NO_x production were measured [e.g., Human et al., 2007; Bertram et al., 2007].

Lightning is a major source of NO_x (NO_2+NO) in the upper troposphere. NO_x is thought to be produced during the return stroke stage of a cloud-to-ground flash and the leader stage of an intra-cloud flash [e.g., Price et al., 1997]. The lightning flash rate is often parameterized as functions of meteorological variables such as convective updraft mass fluxes (UMF), convective available potential energy (CAPE), convective cloud top height, and precipitation rate [e.g., Price et al., 1993; Allen et al., 1999; Choi et al., 2005, 2008a]. Lightning NO_x significantly enhances tropospheric NO_2 columns, in particular, over the ocean, where NO_2 columns are more sensitive to lightning NO_x production due to less impact of surface NO_x emissions [e.g., Choi et al. 2005, 2008a; Martin et al., 2006; Bertram et al., 2007]. It also increases the concentrations of O_3 and PAN in the free troposphere [e.g., Labrador et al., 2004; Hudman et al., 2007]. Hudman et al. [2007] found that lightning enhanced O_3 concentration by ~10 ppbv and PAN by 30% in the upper troposphere based on the INTEX-NA measurements over the eastern North America and western North Atlantic during summer 2004 using the GOES-CHEM model. Still, lightning remains the most uncertain source of NO_x with a global range from

1 to 20 Tg N/yr [Price et al., 1997]. Recent satellite measurements including NO_2 columns from the SCanning Imaging Absorption spectroMeter for Atmospheric CHartographY (SCIAMACHY) were used to show lightning enhanced NO_2 over the North Atlantic Ocean, and to constrain the global lightning NO_x emissions in the range of 4 - 8 Tg N/yr [Martin et al., 2006, 2007].

Both convective transport of tracers and lightning NO_x production are sensitive with underlying meteorological fields. A key factor is the convective parameterization used [Emanuel et al., 1994]. To study these uncertainties and their impact on trace gas simulations, we use a Regional chEmical trAnsport Model (REAM) with meteorological fields generated by two different convective parameterizations based on KF-eta [Kain et al., 2003] and Grell [Grell et al., 2002] convection schemes, respectively. Two meteorological models, the Weather Research and Forecasting (WRF) model [Skamarock et al., 2005] and the Fifth-Generation NCAR/Penn State Mesoscale Model (MM5) [Grell et al., 1995] are used out of necessity since no shallow convection scheme is provided for using with the Grell scheme (for deep convection only) in WRF. The other configurations of the two models are set to be the same, except that the KF-eta scheme is used in WRF and the Grell scheme is used in MM5. When compared to the convective transport and lightning NO_x features measured during INTEX-NA, the model difference can be attributed to mostly the difference of the convective parameterization schemes, not to the difference in the other formulations of the meteorological models.

In this work, we evaluate the simulated convective transport and lighting NO_x production using the INTEX-NA aircraft and satellite measurements to assess their dependence on model cumulus parameterizations. In section 2.2, we describe the REAM

model and the measurements used in the study. The convective impact on tropospheric tracers is analyzed in section 2.3. The lightning impact is examined in section 2.4. Conclusions are given in section 2.5.

2.2 Model and Observations

2.2.1 Model description

The REAM model driven by MM5 assimilated meteorological fields (MM5-REAM) was described by Choi et al. [2008a]. Previously, this model was applied to investigate a number of tropospheric chemistry and transport problems at northern mid latitudes [Choi et al., 2005, 2008a,b; Jing et al., 2006; Wang et al., 2006; Gillus et al., 2007] and in the polar regions [Zeng et al., 2003, 2006; Wang et al., 2007]. In this work, the REAM model is developed to use the WRF assimilated meteorological fields (WRF-REAM). Large changes are apparent in the free tropospheric chemical distributions when WRF fields are used in place of MM5. We find that these changes are due mostly to the underlying convection schemes used.

The model has a horizontal resolution of 70 km with 23 vertical layers below 10 hPa. Meteorological fields are assimilated using either MM5 or WRF constrained by the NCEP reanalysis products (NNRP). The horizontal domain of MM5 or WRF has 5 extra grids beyond that of REAM on each side to minimize potential transport anomalies near the boundary. Most meteorological field inputs are archived every 30 minutes except those related to convective transport and lightning parameterizations, which are archived every 5 minutes. Chemical initial and boundary conditions for chemical tracers in REAM are obtained from the global simulation for the same period using the GEOS-CHEM

model driven by GOES-4 assimilated meteorological fields [Bey et al., 2001]. Anthropogenic and biogenic emission algorithms and inventories are adapted from the GEOS-CHEM model [Choi et al., 2005, 2008a]. One exception is that the emissions of NO_x, CO, and ($\geq C_4$ alkanes) over the US are prepared by Sparse Matrix Operator Kernel Emissions (SMOKE) model (http://cf.unc.edu/cep/empd/products/smoke/index.cfm) for 2004 projected from VISTAS 2002 emission inventory, since we found that these emissions are more consistent with INTEX-NA measurements than the default inventories in GEOS-CHEM. Biomass burning emissions are included following Turquety et al. [2007].

Sub-grid convective transport in WRF-REAM and MM5-REAM is developed to be consistent with the KF-eta and Grell schemes implemented in WRF and MM5, respectively. Both convective schemes simulate moist updrafts and downdrafts. One notable difference is that the KF-eta scheme includes cloud entrainment and detrainment during convection but the Grell scheme does not. Consequently, the vertical distribution of convective mass fluxes and the height of convection are simulated differently between the two schemes. These differences are reflected in the vertical distributions of chemical tracers and are evaluated with INTEX-NA measurements in this study.

The lightning NO_x production rate is parameterized as a function of convective mass fluxes and convective available potential energy (CAPE) as described by Choi et al. [2005] to ensure its consistency with model dynamics. The cloud-to-ground lightning flash rates are parameterized on the basis of the National Lightning Detection Network (NLDN) observations in summer 2004 supplied by the Global Hydrology Resource Center at the NASA Marshall Space Flight Center (http://ghrc.nsstc.nasa.gov/). The

IC/CG flash ratio is calculated following Wang et al. [1998]. A key parameter in this calculation is the cumulus cloud top height. It is assumed that IC and CG flashes have the same energy [Ott et al., 2003; Choi et al., 2005]. Lightning NO_x is distributed vertically following the mid-latitude profile by Pickering et al. [1998]. Based on the INTEX-NA measurements, the lightning NO_x production rate is set to be 250 moles NO/flash.

2.2.2 Chemical Observations

2.2.2.1 Aircraft observations

The Intercontinental Chemical Transport Experiment – North America (INTEX-NA) aims at understanding the transport and transformation of gases and aerosols on transcontinental and intercontinental scales and their outflow of pollution over North America [Singh et al., 2006]. In this study, the measurements of C_2H_6, C_3H_8, HNO_3, NO_2, and O_3 from DC-8 are used. The NO measurements on the DC-8 are not used due to its limited sensitivity only suitable for measuring mixing ratios larger than 100 pptv [Singh et al., 2007]. C_2H_6 and C_3H_8 are measured with 1 pptv detection limit and 2-10% nominal accuracy. HNO_3 is measured with 5-10 pptv detection limit and 10-15% nominal accuracy. NO_2 is measured with 1 pptv detection limit and 10% nominal accuracy. O_3 is measured with 1 ppbv detection limit and 5% nominal accuracy. All the instruments on DC-8 are described in detail by Singh et al. [2006]. One-minute merge data from DC-8 from July 1st to August 14th 2004 are used (http://www-air.larc.nasa.gov/cgi-bin/arcstat). Some compounds were measured by two different techniques such as HNO_3. When both measurements are available, the average values are used.

2.2.2.2 Satellite measurements

2.2.2.2.1 Tropospheric NO_2 columns

SCIAMACHY instrument was onboard the ENVISAT satellite with a spatial resolution of 30x60 km^2 and a temporal resolution of 6-day global coverage. Tropospheric columns of NO_2 retrieved from SCIAMACHY and its uncertainties are calculated by Martin et al. [2006]. The retrieval uncertainties are due to spectral fitting, spectral artifact from the diffuser plate, the removal of stratospheric column, and air mass factor calculation. The measurements with the cloud fraction larger than 30% are excluded in the study in order to reduce the impact of cloud on satellite retrieval. A more detailed description regarding the tropospheric NO_2 columns from SCIAMACHY and its validation with INTEX-NA measurements can be found in Martin et al. [2006].

2.2.2.2.2 Cloud top pressure

The operational data collection phase of the International Satellite Cloud Climatology Project (ISCCP) began in July 1983 and the dataset provides a global cloud climatology processed based on the images from an international network of weather satellites [Rossow and Schiffer, 1991]. The measurements of cloud top pressure over North America provided by the ISCCP DX dataset with 3-hourly 30 km sampled pixels processed from the images of GOES-10 and GOES-12 satellites are used to evaluate the model simulated cumulus cloud top heights. The measurements with the cloud top pressure larger than 500 hPa are excluded in the study to filter out the low cloud information.

2.3 Uncertainties in modeling convective impacts on tropospheric trace gases distributions

2.3.1 Dependence of convective transport on cumulus parameterization

Figure 2.1a shows the spatial distributions of the mean updraft mass fluxes of deep convection at three typical pressure levels (800, 500, and 300 hPa) from WRF and MM5 simulations with KF-eta and Grell convection schemes, respectively, for July and August 2004. WRF and MM5 simulate generally similar spatial distributions of mass fluxes with strong convection events over the western and southeastern US, Mexico, and the western North Atlantic Ocean. One clear difference is that the updraft fluxes at 500 and 800 hPa are much higher in WRF than MM5. The mass fluxes in WRF are not as spatially concentrated over western-central US and are more over the Southeast than MM5. Figure 2.1b shows the vertical profiles of mass fluxes from the two models averaged over North America (domain shown in Fig. 2.1a). The difference is large. The updraft fluxes in WRF are much larger than MM5 at 300-900 hPa. The downdraft fluxes of WRF occur at lower altitudes than MM5. Entrainment and detrainment only in WRF are high in the lower and upper troposphere. The larger updraft fluxes as well as entrainment and detrainment in WRF lead to larger wet scavenging of soluble species than MM5. The convection top simulated by MM5 is higher than that by WRF. While not that significant in pressure coordinates, the altitude difference is quite large, leading to large difference in the distribution of pollutant outflow and lightning NO_x.

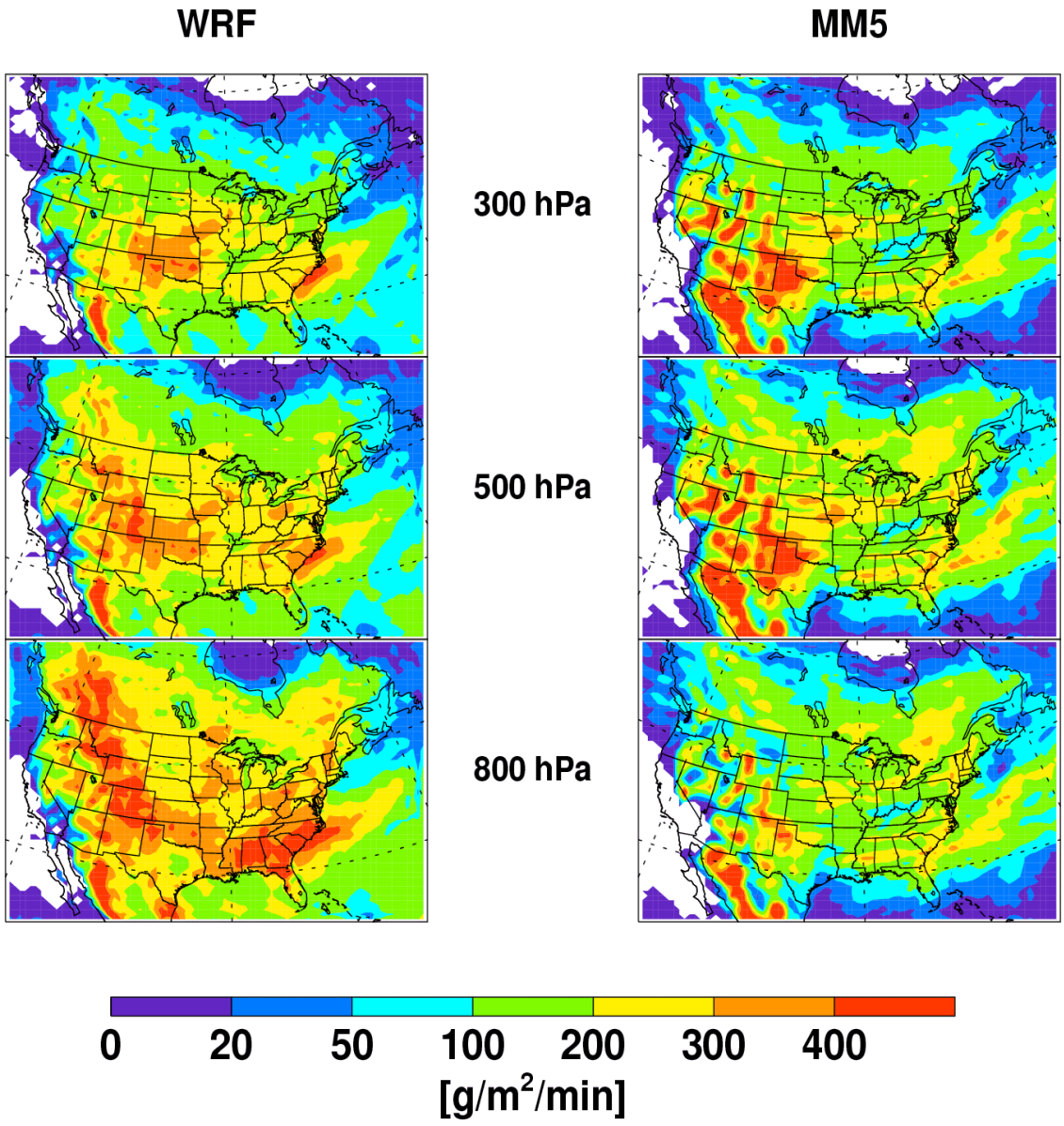

Figure 2.1a Mean deep convective updraft mass fluxes from WRF and MM5 simulations for July and August 2004.

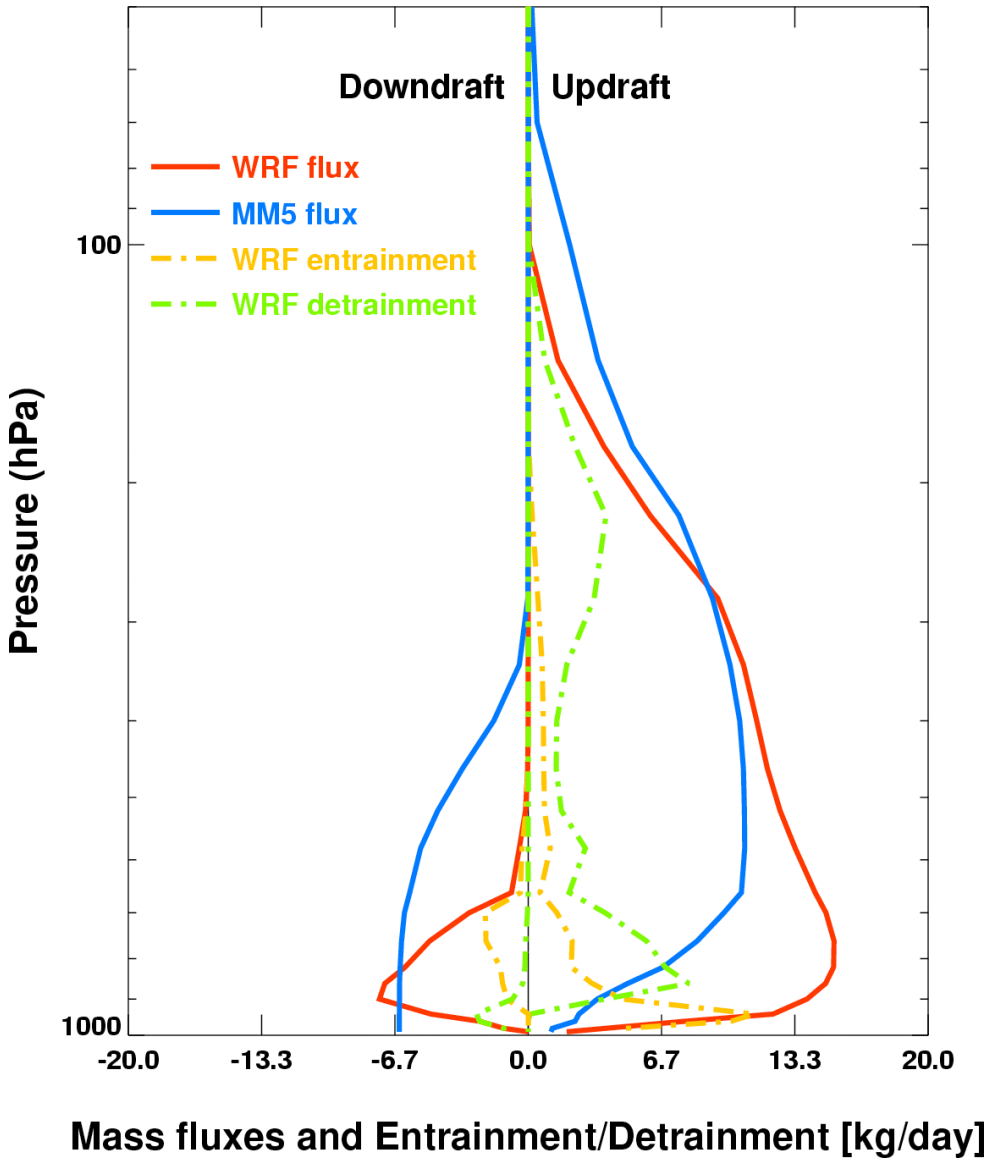

Figure 2.1b Vertical profiles of mean mass fluxes of deep convection from WRF and MM5 simulations, and the average entrainment and detrainment fluxes from the WRF simulation for July and August 2004 over North America (shown in Fig. 2.1a). Positive (negative) fluxes are updrafts (downdrafts).

2.3.2 Convective impact on exports of pollutants

Convective transport lifts non-soluble pollutants from the boundary into the free troposphere. As a result, concentrations increase at higher altitudes and decrease at lower altitudes. In model simulations, the change of concentrations as a function of altitude reflects the strength of convective transport. Here we use C_3H_8 as an example. Figure 2.2 shows the relative changes of C_3H_8 drived by convection at the surface and four typical pressure levels (800, 500, 300, and 150 hPa) for July and August 2004 in the two models. Both models show decreases of C_3H_8 at the surface and 800 hPa. At 500 hPa, convective transport increases C_3H_8 in WRF-REAM particularly over the Southeast because of entrainment and detrainment and updraft flux convergence. MM5-REAM, in contrast, shows a general convection-driven decrease. At higher altitudes, both models show increasing concentrations due to convection. However, the largest increase is at 300 hPa in WRF-REAM but at 150 hPa in MM5-REAM. The maximum outflow altitude is higher in MM5-REAM because the convective top is higher in MM5 (Fig. 2.1b).

Simulated C_3H_8 concentrations are 15-35% higher in WRF-REAM than MM5-REAM at 3-8 km, in better agreement with the INTEX-NA observations (not shown). To minimize the effects of emission uncertainties and the large vertical gradient of C_3H_8 in this analysis, we investigate the convective effects on C_2H_6/C_3H_8 ratios [Wang and Zeng, 2004]. The chemical lifetime of C_3H_8 (2 weeks) is shorter than C_2H_6 (>1 month). Long-range transport of C_3H_8 is less efficient and we expect to see a larger convective transport effect on C_3H_8 than C_2H_6.

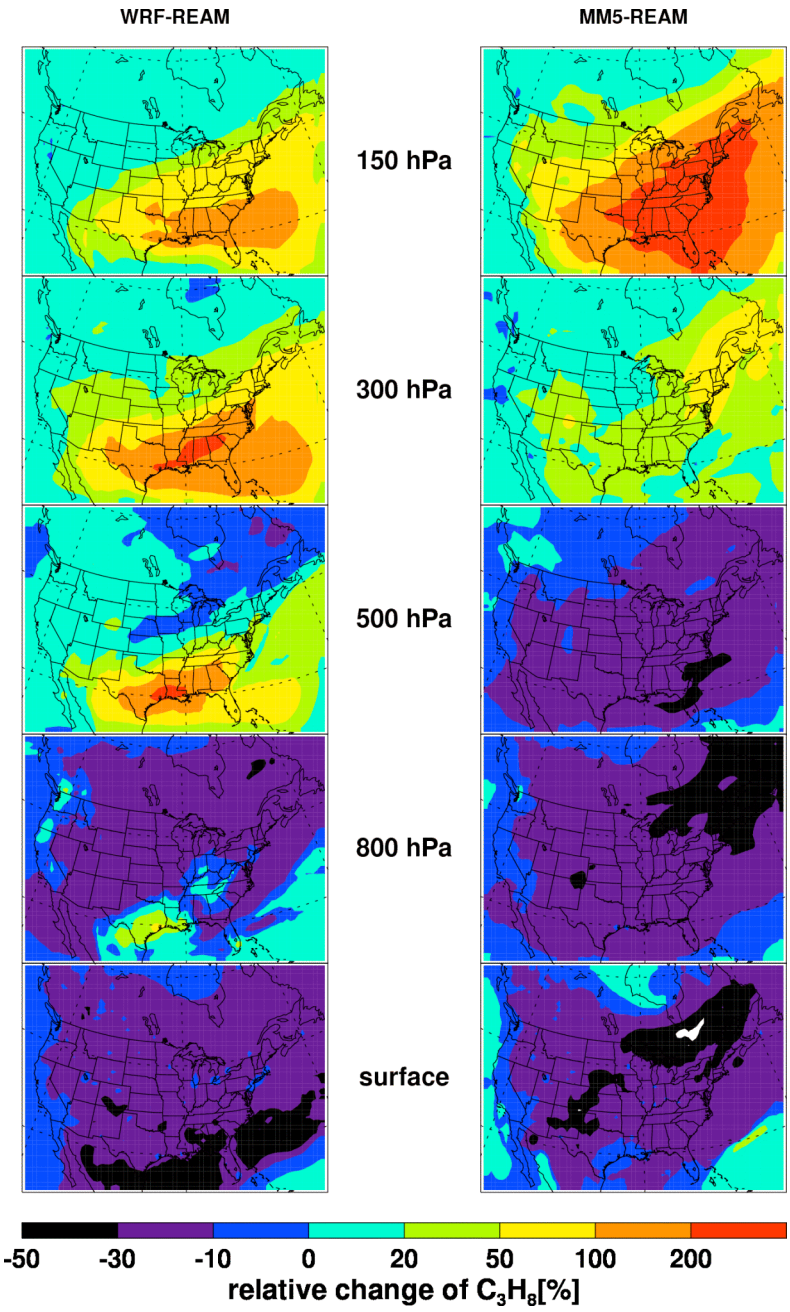

Figure 2.2 Percentage changes of C_3H_8 in the standard model simulations from the model simulations without convective transport for July and August 2004 at the surface, and 150, 300, 500, and 800 hPa. Results for WRF-REAM and MM5-REAM are shown.

We compare the median profiles of C_2H_6/C_3H_8 over the outflow region of the western North Atlantic in both models with the INTEX-NA measurements in Figure 2.3. We also show the sensitivity results when convective transport is turned off in the model. The observations show the lowest median C_2H_6/C_3H_8 ratio of 4-5 in the boundary layer. The observed ratio reaches a maximum of 9 at 3 km and gradually decreases to 4-5 at 11 km. Generally speaking, the ratio of C_2H_6/C_3H_8 increases in the troposphere as a result of differential chemical aging and atmospheric mixing [Wang and Zeng, 2004]. Therefore, the ratio of C_2H_6/C_3H_8 tends to increase from the boundary to the free troposphere. The observed decrease of C_2H_6/C_3H_8 ratio reflects the effects of convective transport, which mixes upper tropospheric (high C_2H_6/C_3H_8 ratio) air mass with low C_2H_6/C_3H_8 ratio air mass lifted from the boundary layer into the free troposphere. We note that the amount of mixing is determined by flux vertical convergence, not by the direct fluxes shown in Fig. 2.1a. The measurement variability is larger in the lower troposphere, reflecting a mixture of fresh continental air with low C_2H_6/C_3H_8 ratios and aged marine air with high C_2H_6/C_3H_8 ratios over the western North Atlantic.

Among the model simulations, both standard models reproduce the general profiles of the observed C_2H_6/C_3H_8 ratio; the profile from WRF-REAM is in closer agreement with the measurements. MM5-REAM median profile is at the upper bound of the measurements at 4-9 km. More telling of the model difference is in the sensitivity simulations. Without convective transport, the simulated median C_2H_6/C_3H_8 ratios in WRF-REAM would be a factor 2-3 too high compared to the measurements. In MM5-REAM, the effect of convective transport is evident only in the upper troposphere (above 7 km) as indicated in Fig. 2.2. The lack of convective mixing in MM5-REAM results in

overestimates of the C_2H_6/C_3H_8 ratio in the free troposphere at 3-9 km. The convective effect in MM5-REAM becomes larger than WRF-REAM above 11 km. There is no direct in situ observation to evaluate the model performance above 11 km. What we will show in section 2.4.1 is that the convective cloud top is overestimated in MM5 compared with GOES satellite observations, particularly over the western North Atlantic. WRF simulations are in closer agreement with the observations.

We also examine the effects of convective scavenging of soluble HNO_3. We assume that HNO_3 is removed in convective updrafts in the model [e.g., Wang et al., 2001]. This wet scavenging pathway effectively removes HNO_3 lifted from the boundary. However, HNO_3 produced from lightning NO_x is not scavenged in this process. With entrainment (such as in WRF-REAM), background HNO_3 entrained into cumulus clouds is also removed. Without entrainment scavenging, upper tropospheric HNO_3 concentrations can be high from lightning NO_x. In general, simulated HNO_3 concentrations are lower in WRF-REAM than MM5-REAM and are in better agreement with the INTEX-NA measurements although both model simulations of median HNO_3 profiles are within the standard deviations of the measurements (Appendix A). WRF simulates higher convective mass fluxes than MM5 and also includes entrainment fluxes (Fig. 2.1b). Both factors contribute to larger wet scavenging in WRF-REAM.

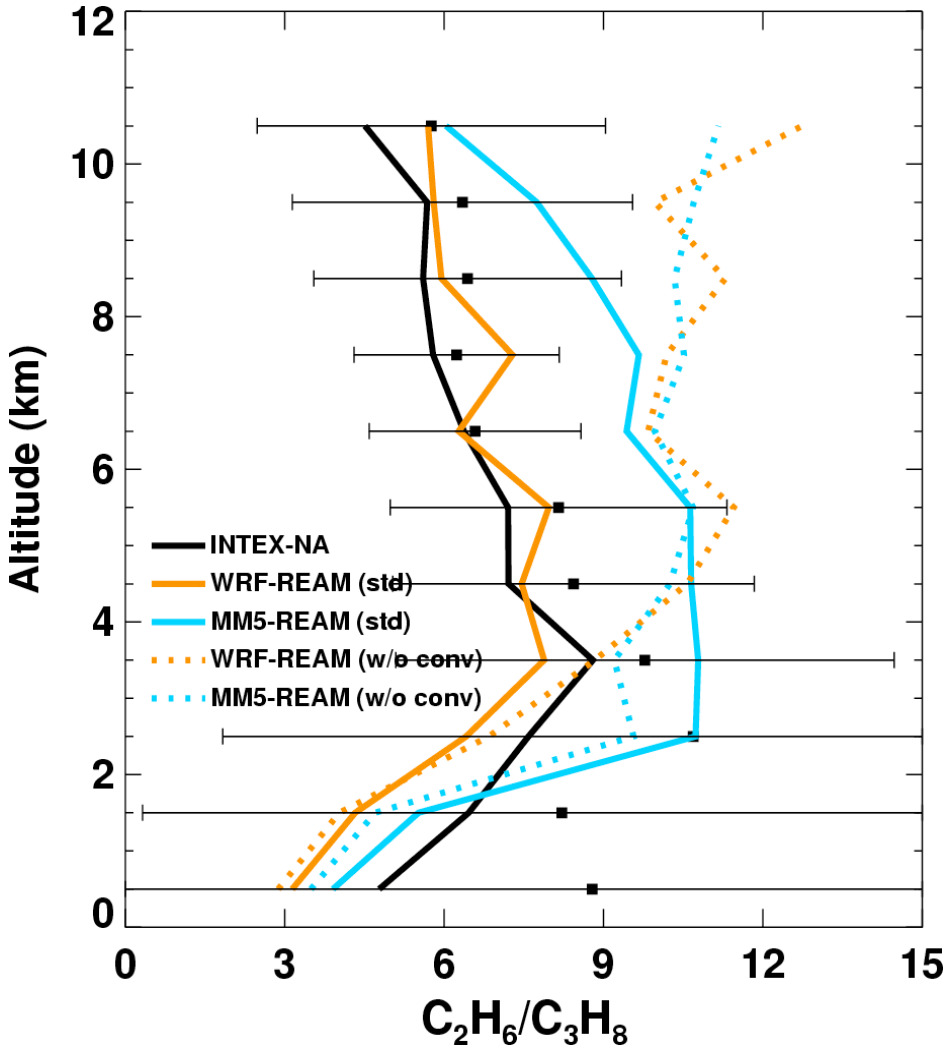

Figure 2.3 Observed and simulated vertical profiles of median C_2H_6/C_3H_8 ratio in the outflow regions over the western North Atlantic. Black squares show the observed means at 1-km interval. The horizontal bars show the standard deviations. "std" denotes the standard simulation. "w/o conv" denotes the simulation where convective transport is turned off.

2.4 Uncertainties in modeling lightning NO_x production and its impact on tropospheric O_3

2.4.1 Cumulus cloud top and lightning NO_x production

We compare model simulated tropospheric NO_2 columns with SCIAMACHY measurements for July and August 2004 [Martin et al., 2006] to illustrate the difference of lightning NO_x production between the two models (Fig. 2.4). The temporal resolution of SCIAMACHY is low; it covers the globe every 6 days. After filtering out measurements with cloud fractions > 30%, there are only about 2 measurements over the eastern US. Therefore, the comparison here is qualitative in nature. Some of the overestimates in the models can be traced back to simulated lightning influence in one of the measurement days. WRF-REAM and MM5-REAM simulations are very similar when lightning NO_x is excluded. When including lightning NO_x, WRF-REAM simulated NO_2 columns are lower than MM5-REAM and are closer to the limited observations. The spatial correlation is also higher in WRF-REAM (R=0.73) than MM5-REAM (R=0.58). Lightning NO_x production is lower in WRF-REAM than MM5-REAM. For example, NO_2 columns above 12 km are mainly due to lightning NO_x. They are much lower in WRF-REAM than in MM5-REAM (Fig. 2.4). Over the western North Atlantic, NO_2 columns above 12 km account for 10% of the total column in WRF-REAM but ~50% in MM5-REAM. Specifying a lower NO_x production rate per flash in MM5-REAM than WRF-REAM can correct the high bias in MM5-REAM. However, the correction will also lead to large underestimations in MM5-REAM compared to INTEX-NA aircraft measurements (to be discussed in the next section).

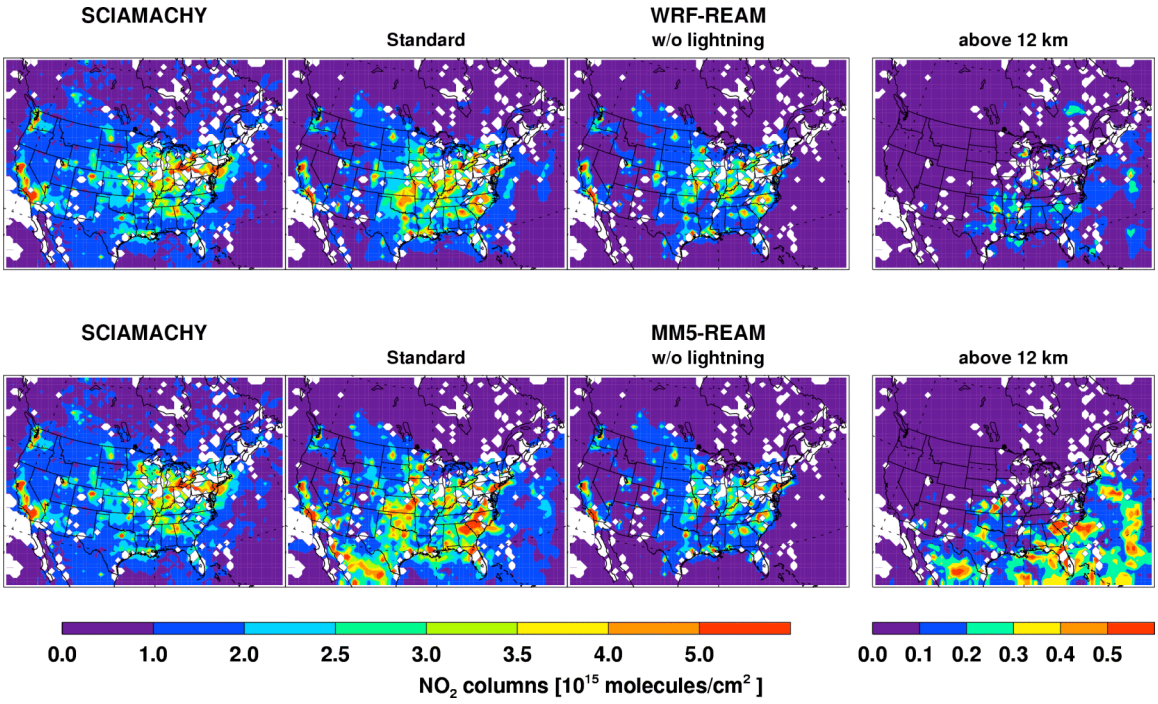

Figure 2.4 Tropospheric NO_2 columns derived from SCIAMACHY measurements [*Martin et al.*, 2006] and simulated by WRF-REAM and MM5-REAM for July and August 2004. Tropospheric columns from the standard simulation and a sensitivity simulation without lightning NO_x are shown. Also shown are the tropospheric columns above 12 km in the standard simulation. Only the measurements with cloud fractions < 30% and the corresponding simulation results are used. White areas indicate that no measurement data are available.

The large difference in simulated lightning NO_x production between WRF-REAM and MM5-REAM is due mainly to the difference in the simulated cumulus cloud top heights. The simulated vertical distribution of lightning NO_x follows the mid-latitude profile by Pickering et al. [1998]. Figure 2.5 shows the lightning NO_x distributions in the two models averaged over North America. MM5-REAM simulates the lightning NO_x maximum at ~15 km much higher than that in WRF-REAM at ~12 km. It is important to note that even though MM5-REAM simulates much more total lightning NO_x than WRF-REAM, two models simulate similar lightning NO_x production at 2-12 km, which will explain why two models simulate similar lightning impact on the upper tropospheric (8-12 km) NO_2 and O_3 concentrations shown in the next section. Our lightning NO_x parameterization is based on the observed cloud-ground (CG) flash rates from the NLDN network [Choi et al., 2005, 2008a]. The intra-cloud (IC) lightning flash rates are estimated in the model as a function of the freezing altitude and cumulus cloud top height [Wang et al., 1998]. A higher cloud top height generally leads to higher lightning NO_x production.

We therefore evaluate model simulated cumulus cloud top heights with the measurements by GOES-10 and GOES-12 satellites from the DX cloud dataset of the ISCCP [Rossow and Schiffer, 1991] in Figure 2.6. Clearly, the problem is in MM5 results, where cloud top pressures are underestimated over the Gulf of Mexico, the southeastern US and the western North Atlantic. The overestimates of cloud top heights lead to higher IC/CG flash ratios and overestimates of lightning NO_x production in these regions (Fig. 2.4). It also becomes apparent that lightning NO_x in MM5-REAM is injected too high in altitude (Fig. 2.5). Convection in WRF KF-eta scheme reaches to a

lower altitude in part because entrainment from drier free tropospheric air and detrainment reduce the buoyancy in the convective updraft. Without entrainment and detrainment, the updraft reaches to 16 km (rather than 10-12 km in WRF) in MM5. Satellite measurements of NO_2 (indirectly) and cloud top pressure (directly) indicate that KF-eta scheme in WRF is more realistic.

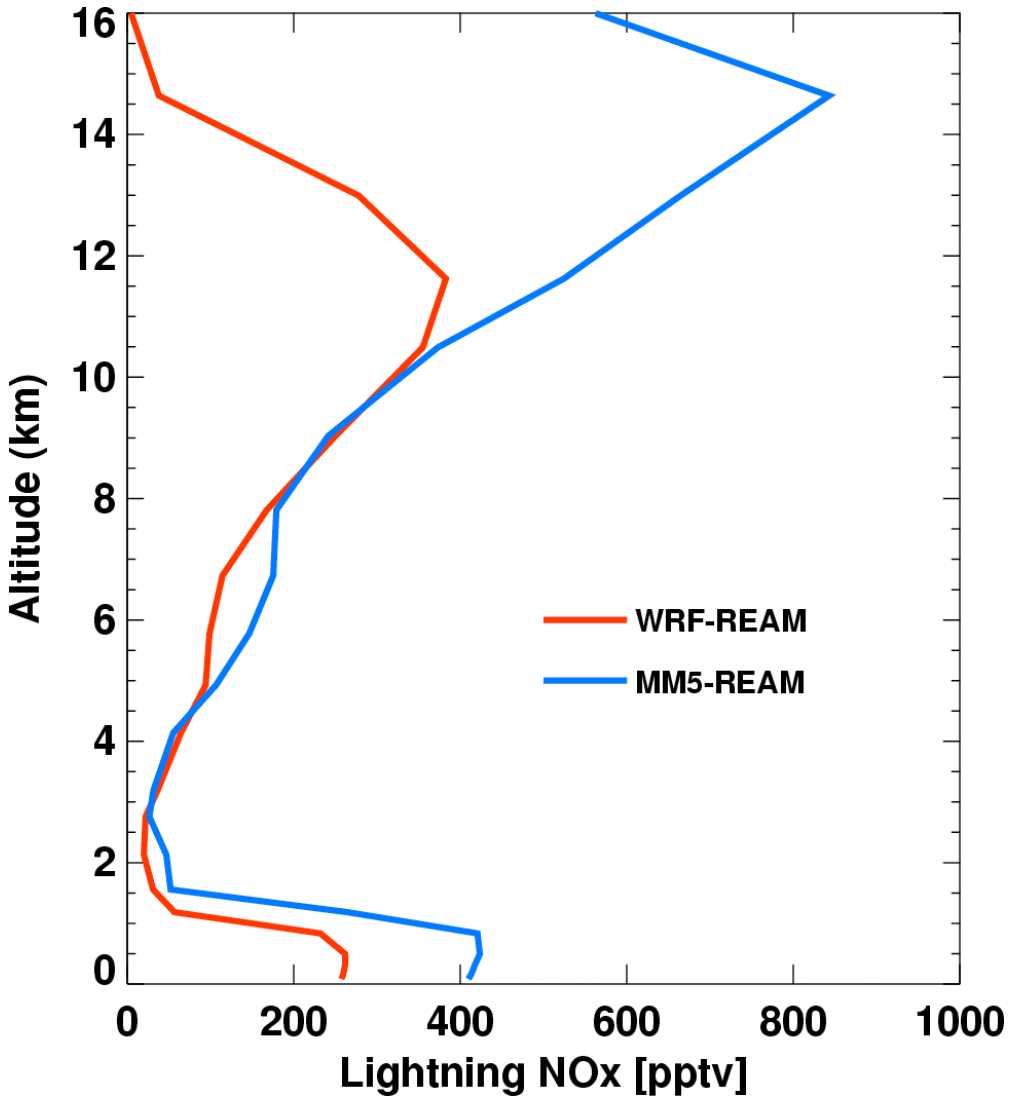

Figure 2.5 Mean lightning NO_x mixing ratio profiles in WRF-REAM and MM5-REAM for July and August 2004 averaged over North America.

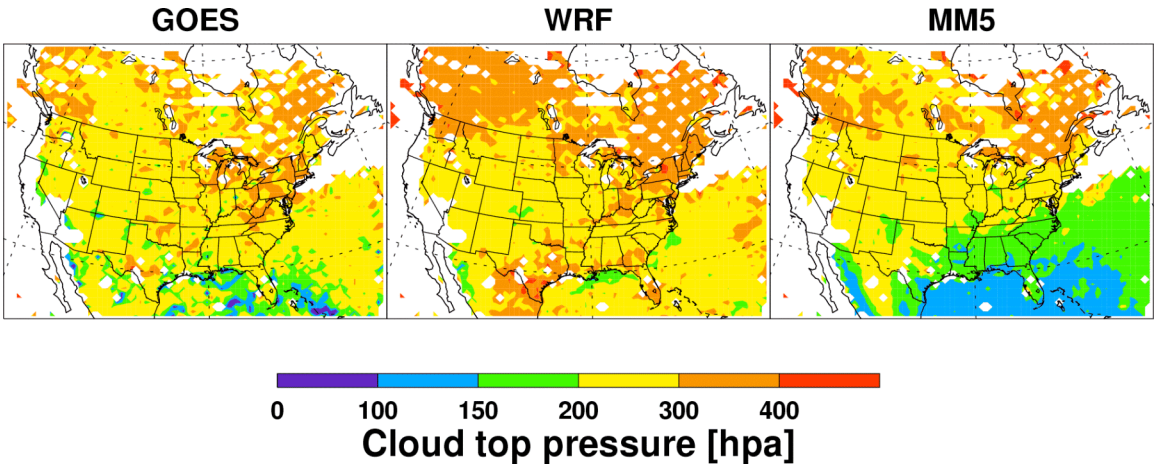

Figure 2.6 Mean cumulus cloud top pressures measured by GOE-10 and GOE-12 satellites and simulated by WRF and MM5 for July and August 2004. Measurement data > 500 hPa (and corresponding model results) are excluded to filter out the low cloud information.

2.4.2 Effects of lightning NO_x during INTEX-NA

The large model difference in lightning NO_x is not necessarily reflected in the comparison with aircraft NO_x measurements because the flight ceiling of DC-8 is 12 km. Figure 2.7 show the comparisons of upper tropospheric NO_2 at 8-12 km along the DC-8 flight tracks. The difference between WRF-REAM and MM5-REAM is not as significant as we found in Figures 4-6 because of the similar lightning NO_x emissions from the two models at 2-12 km (Fig. 2.5). Upper tropospheric NO_x in both models are driven by lightning, which increases NO_2 mixing ratios by a factor of up to 5 (~100 pptv). Both models simulate larger lightning impacts over the southeastern US than the Northeast and the eastern Canada. Measurements indicate that model underestimates lightning NO_x production in the latter regions. Similar underestimates are also found in previous studies

[e.g., Hudman et al., 2007]. Figure 2.1a shows that convective mass fluxes in the upper troposphere in both WRF and MM5 are generally low over those regions. Measurements by the NLDN network also show lower CG flashes there. Therefore, the model underestimates may reflect a higher NO_x production rate per flash in the northern regions than the southeastern US.

Lightning NO_x is a major source of O_3 in the upper troposphere and significantly affects the budget of tropospheric O_3. Hudman et al. [2007] found lightning can increase upper troposphere O_3 concentrations by ~10 ppbv and Cooper et al. [2006] found an increase of 11-13 ppbv during INTEX-NA. We find, here, that, O_3 concentrations are increased by up to ~20 ppbv (Fig. 2.7). The average O_3 enhancement is ~10 ppbv. Despite the difference in the underlying meteorological fields, simulated O_3 concentrations and their sensitivities to lighting NO_x are similar between WRF-REAM and MM5-REAM since lightning enhancements of NO_2 are similar between the two models at 8-12 km. The enhancements of O_3 by lightning NO_x improve model simulations compared to INTEX-NA measurements. Upper tropospheric O_3 concentrations are affected by lightning mainly over the southeastern US and eastern Canada. Tropospheric O_3 production from surface emissions of NO_x and volatile organic compounds (VOCs) and transport from the stratosphere also make significant contributions to upper tropospheric O_3 [Choi et al., 2008a].

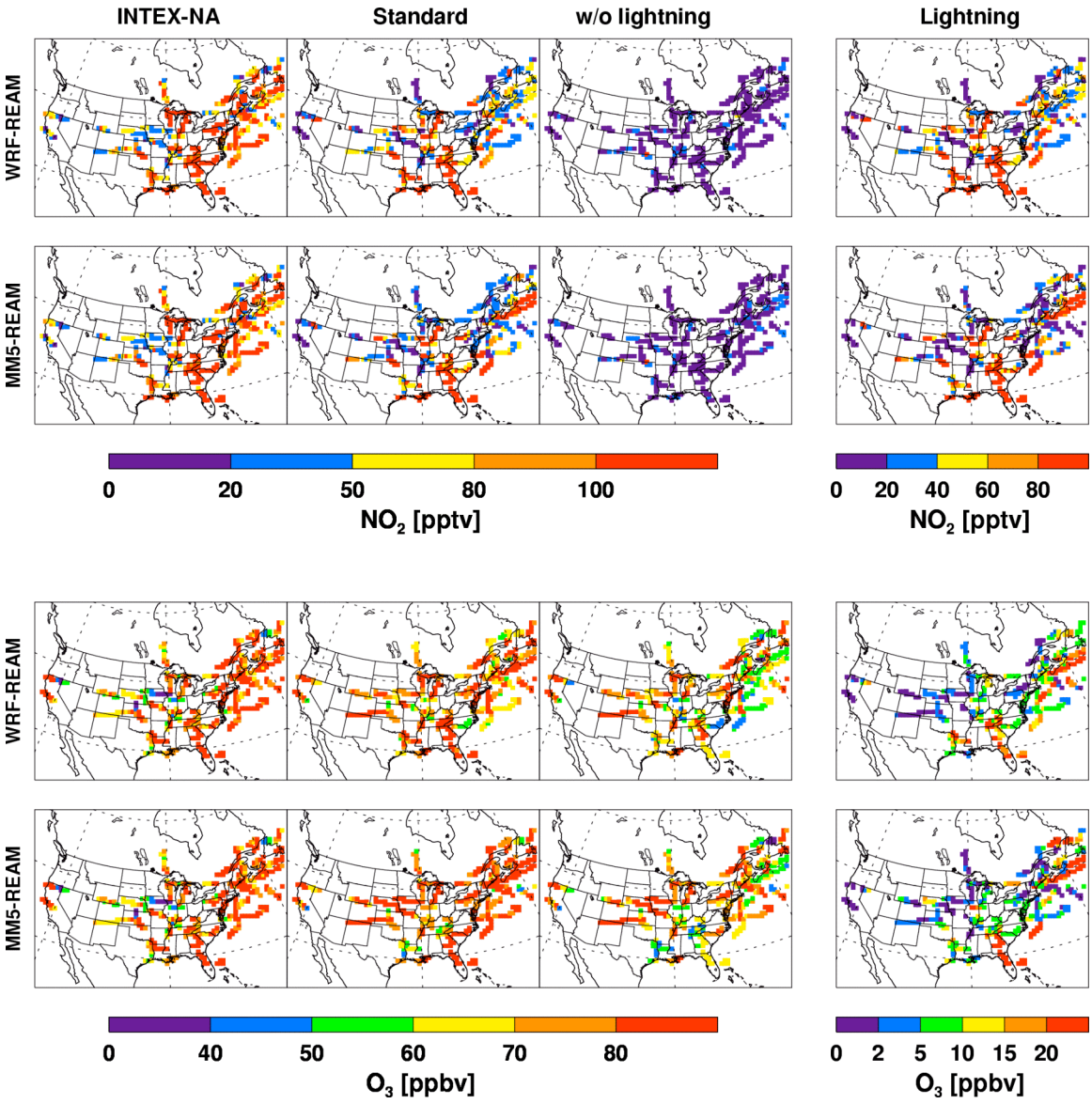

Figure 2.7 Observed and simulated upper tropospheric NO_2 and O_3 concentrations along DC-8 flight tracks at 8-12 km during the INTEX-NA experiment. Results from the standard simulations and sensitivity simulations without lightning NO_x using WRF-REAM and MM5-REAM are shown. The impacts of lightning (rightmost column) are estimated by subtracting the sensitivity results from the standard model results.

2.4.3 Relative contributions of surface and lightning emissions to tropospheric NO_x

The relative importance of the different odd nitrogen sources in the troposphere has been investigated in previous studies [e.g., Lamarque et al., 1996; Levy et al., 1999; Allen et al., 2000; Grewe et al., 2001; Tie et al., 2001]. Grewe et al. [2001] investigated the origins of the upper tropospheric NO_x and summarized the previous work. They suggested contribution ranges of 15-60% for lightning and 7-60% for surface emissions to upper tropospheric NO_x over the northern mid-latitude in July. The wide ranges reflect the different treatments of emissions, chemistry, and transport in the models. In our simulations, WRF-REAM and MM5-REAM show similar results up to 12 km. Lightning contribution to NO_x increases from ~10% in the boundary layer to up to 70% in the upper troposphere (8-12 km). In contrast, the surface emission contributions decrease from 80% in the boundary layer to ~10% at 8-12 km (Appendix A). Above 12 km, the two models clearly diverge. WRF-REAM simulates ~50% and MM5-REAM simulates ~90% of the lightning contribution. The NO_x concentrations at 12-15 km from the MM5-REAM simulation more than double those from WRF-REAM simulation due to lightning. The divergence between WRF-REAM and MM5-REAM above 12 km reflects the lightning NO_x vertical profiles in Figure 2.4. The NO_x concentrations due to surface emissions from MM5-REAM simulation are ~50% higher than that from WRF-REAM simulation because of the absence of the dilution from entrainment and detrainment and the higher cloud top height in MM5 simulation. We also estimate contributions of ~40 and 10% to total reactive nitrogen (NO_y) from lightning and surface emissions at 8-12 km, respectively (Appendix A). Previously, Allen et al. [2000] estimated a 13% contribution from lightning and 16% contribution from surface emissions for October-November 1997

during the SONEX experiment. More intensive summertime lightning is likely the reason for a larger impact in our results.

2.5 Conclusions

Two convective schemes, KF-eta scheme in WRF-REAM and Grell scheme in MM5-REAM, are used to evaluate the uncertainties in modeling convective transport and lightning NO_x production. When compared to the convective transport and lightning NO_x features measured during INTEX-NA, we find that the model difference can be attributed to mostly the difference of the convective parameterization schemes, not to the difference in the other formulations of the meteorological models.

The KF-eta scheme simulates larger updrafts in the lower troposphere, resulting in significantly more outflow at 3-9 km than the Grell scheme. A sensitivity chemical indicator affected by this outflow is C_2H_6/C_3H_8 ratio. While WRF-REAM shows large decreases (up to a factor of 2) of C_2H_6/C_3H_8 ratio at 3-9 km due to convective outflow, the change is relative small in MM5-REAM. In comparison, the two models are in agreement in the boundary layer and 10-11 km. INTEX-NA observations clearly indicate WRF-REAM simulations are in closer agreement with the observations. Larger mass fluxes as well as entrainment and detrainment in the KF-eta scheme in WRF-REAM also lead to more scavenging of soluble HNO_3 in the free troposphere than MM5-REAM. The simulated median profile of HNO_3 by WRF-REAM is in closer agreement with the measurements than MM5-REAM, although the observed variation is larger than the model difference.

Inclusion of entrainment and detrainment in the KF-eta scheme results in lower convective cloud top in WRF than MM5. The cloud top height directly affects the model estimates of intra-cloud lightning production. Consequently, WRF-REAM simulates less lightning NO_x than MM5-REAM and the maximum lightning NO_x altitude of 12 km in WRF-REAM is lower than 15 km in MM5-REAM. Measurements of tropospheric NO_2 columns from SCIAMACHY provide a qualitative comparison, which suggests that WRF-REAM is closer to the observations, although the lower temporal resolution and cloud presence over convective regions greatly reduced the number of valid measurements. Evaluation using the ISCCP cloud top height measurements from GOES satellites clearly demonstrated that MM5 simulated convective cloud tops are too high over the southeastern US and western North Atlantic.

It is interesting to note that the large model difference in lightning NO_x and convective transport occurs mostly above 12 km, where no in situ measurements were available from INTEX-NA. Despite the large differences discussed previously, the two models show similar agreement with upper tropospheric in situ NO_2 measurements. Over the observation regions of INTEX-NA, the two models show consistent results for the effects of lightning NO_x in the upper troposphere: (1) lightning enhances upper tropospheric NO_2 concentrations by more than a factor of >5 (~100 ppt) and NO_2 columns by a factor of >1.5 over the ocean; (2) lightning and surface emissions contribute ~70% (40%) and ~10% (10%), respectively, to the upper tropospheric NO_x (NOy); and (3) lightning NO_x increases O_3 concentrations by up to 20 ppbv with an average of 10 ppbv. These results are generally consistent with previous studies.

CHAPTER 3

[2]ASSIMILATED INVERSION OF NO_x EMISSIONS OVER EAST ASIA USING OMI NO_2 COLUMN MEASUREMENTS

3.1 Introduction

Ozone (O_3) is a key pollutant, a greenhouse gas, and an important factor in determining the oxidizing power of the atmosphere. It is largely controlled by nitrogen oxides (NO_x=NO+NO_2) in the troposphere. NO_x in the troposphere originates from fossil fuel combustion, lightning and soils. The traditional bottom-up approach to estimate NO_x emissions makes use of compilations of emission statistics and source factors. For fossil fuel sources, for example, emission factors are generally developed for industry, domestic, transport and power plants. In regions such as China, where emission statistics and characteristics are incomplete, the bottom-up inventory uncertainties could be large [e.g, Streets et al., 2003]. Global tropospheric NO_2 distributions were measured by several satellite instruments in the last decade. Many studies showed that satellite measurements provide important top-down constraints for improving emission inventories [e.g., Martin et al., 2003 and 2006; Y.X. Wang et al., 2007; Choi et al., 2008a].

China contributes significantly to the global NO_x budget, and its NO_x emission inventories based on the bottom-up approach are thought to be quite uncertain [e.g.,

---

[2] This Chapter is for "Assimilated inversion of NO_x emissions over East Asia using OMI NO_2 column measurements" published in Geophysics Research Letter in 2009. Authors are C. Zhao and Y. Wang.

Streets et al., 2003; Zhang et al., 2007]. Ma et al. [2006] compared NO_2 columns inferred from GOME over China with model results using three different bottom-up inventories of NO_x. They found that the model underestimated the GOME observations for China with a negative bias of 31%-67%. Y.X. Wang et al. [2007] found a low model bias of 40% with anthropogenic NO_x emissions taken from the Global Emission Inventory Activity (GEIA) [Benkovitz et al., 1996] for East China. They developed a top-down inventory of surface NO_x emissions for East China using GOME measurements for a 3-year period (1997, 1998, and 2000), and found that the a posteriori estimate of fuel combustion NO_x emissions for East China is 3.72 Tg N/yr, 15% higher than the a priori. A large underestimation of soil NO_x emissions was suggested by their study.

Due in part to the poor temporal resolutions available from GOME and SCIAMACHY satellite measurements, all previous applications of the top-down approach in optimizing NO_x emissions were on a monthly-mean basis [e.g., Martin et al., 2003; Y.X. Wang et al., 2007; Boersma et al., 2008]. The improvement in temporal and spatial resolutions of the recent OMI instrument [Boersma et al., 2007] provides an opportunity to apply an assimilated inversion on a daily basis to derive an optimized NO_x inventory, which allows for iterative adjustments of the NO_x emissions compared to one single inversion in the previously used monthly-mean approach. One important benefit of the daily assimilated inversion is that chemical feedbacks driven by changing NO_x emissions, such as the nonlinear feedback through OH [Stavrakou et al., 2008], are taken into account.

We develop and implement the daily assimilated inversion into a 3-D chemical transport model to derive optimized surface NO_x emissions over East Asia (80-150^{o}E, 10-

50°N) with the OMI NO_2 measurements in July 2007. The method is not meant to constrain the day-to-day variation of NO_x emissions. The a posteriori NO_x emissions from the daily assimilated inversion are compared with those from a priori inventories and monthly-mean inversions to demonstrate the advantages of the assimilated inversion. Two a priori emission inventories are used to investigate the sensitivity of the inversion results to the a priori inventory. Lastly, we derive the a posteriori fossil fuel NO_x emissions in the region. The a priori and monthly-mean and daily assimilated a posteriori emissions are evaluated using OMI measurements in August 2007.

3.2 OMI tropospheric NO_2 columns

OMI onboard the NASA Aura satellite has a daily global coverage, and passes cross the equator at 1:45 PM local time. The nadir horizontal resolution of OMI is 24x13 km^2. The retrieved tropospheric NO_2 columns and its uncertainties are available from two independent products: near-real time (NRT) tropospheric NO_2 columns retrieved by KNMI/NASA [Boersma et al., 2007] and OMI standard product at NASA Goddard Earth Sciences Data and Information Services Center (GES-DISC) [Bucsela et al., 2006]. Bucsela et al. [2008] found significant difference between the two products. Lamsal et al. [2008] found a seasonal component to the bias in the annual mean in the standard product over North America. Our analysis shows that the difference between the NRT product and the standard product is much less over East Asia than over North America in the summer of 2007. The reason is unclear. Therefore, we obtain the "best-estimates" of tropospheric NO_2 columns by averaging the columns from KNMI and GES-DISC weighted by their uncertainties. We did not attempt to recalculate the air mass factors in

either product. We use two methods to estimate the errors in the combined OMI columns. The first method is to estimate the errors as the root mean square of the uncertainties of the two retrievals. The second method is to estimate the error as the deviations of KNMI and GES-DISC retrievals from their means. We take the larger of the two estimates as the uncertainty for the combined OMI columns, which is around 40% over the polluted regions and reaches a factor of 1.5 over the ocean and clean continent such as western China. Only the OMI tropospheric NO_2 column data with cloud fractions of < 30% are used in the study.

3.3 REAM model

The REAM model driven by MM5 assimilated meteorological fields (using the NCEP reanalysis) is described by Choi et al. [2008a]. In this study, we use WRF in place of MM5, as we found REAM performance better with meteorological fields from WRF compared with satellites and in-situ measurements (discussed in Chapter 1). Previously, this model was applied to investigate a number of tropospheric chemistry and transport problems at northern mid latitudes [Choi et al., 2005 and 2008a,b; Jing et al., 2006; Y.H. Wang et al., 2006; Guillas et al., 2007] and in the polar regions [Zeng et al., 2003 and 2006; Y.H. Wang et al., 2007]. The REAM model has a horizontal resolution of 70 km with 23 vertical layers below 10 hPa. The time steps for transport and chemistry are 5 minutes and 1 hour respectively. Most meteorological inputs in REAM are updated every 30 minutes except those related to convective transport, which are updated every 2.5 minutes. The horizontal domain of WRF has 5 extra grids beyond that of REAM on each side to minimize potential transport anomalies near the boundary. Initial and boundary

conditions for chemical tracers in REAM are obtained from the global simulation for 2007 using the GEOS-CHEM model with assimilated meteorology (GEOS-5) [Bey et al., 2001]. We ran the daily inversion for July 2007 to obtain the a posteriori emissions. Biogenic emission algorithms are adapted from the GEOS-CHEM model. The lightning NO_x emission is parameterized as Choi et al. [2008b]. The anthropogenic emissions of tracers other than NO_x are taken from a recent bottom-up Asian emission inventory developed by Streets et al. for 2006 INTEX-B campaign (the detail can be obtained from http://www.cgrer.uiowa.edu/EMISSION_-DATA_new/index_16.html; hereafter referred to as Streets2006).

NO_x emissions from fossil fuel combustion are adopted from two recent independent inventories in order to investigate the effect of the a priori inventory on the inversion of NO_x emissions over East Asia. The inventories are Streets2006 and POET2000 prepared by Granier et al. [2005] for 2000 with a global coverage, respectively. The emissions over China from both inventories are scaled to 2007 with an annual increasing rate of 8%, which was also used in developing Streets2006 inventory (Person. Comm., D. D. Streets, 2008). Other studies have found an increase rate of 5-10% [e.g., Stavrakou et al., 2008]. In this manner, we obtain scaled-Streets 2007 and scaled-POET 2007 inventories. The algorithm of soil NO_x emissions follows Yienger and Levy [1995] as adopted by Y.H. Wang et al. [1998]. Few fires are observed by the Moderate Resolution Imaging Spectroradiometer (MODIS) [Kaufman et al.,1998] over East Asia in July 2007, and Y.X. Wang et al. [2007] suggested that the biomass burning source is a small portion of the total NO_x emissions over East China. Biomass burning NO_x is therefore excluded in the study.

We estimate the uncertainty of the a priori fossil-fuel combustion inventory as the difference between the scaled-Streets 2007 and scaled-POET 2007 inventories. The uncertainty of soil emissions is estimated as 300% since Y.X. Wang et al. [2007] concluded that the a priori soil emissions should be increased by a factor of 3 in summer over East China. The overall uncertainty of the a priori surface NO_x emissions is around 60% over most East Asia regions, but reaches 300% over the regions where the soil emissions dominate.

3.4 Results and Discussion

3.4.1 A priori surface NO_x emissions and corresponding tropospheric NO_2 columns

Model simulations are conducted using either the scaled-Streets 2007 or scaled-POET 2007 inventory (hereafter referred to as case A or case B, respectively). The total a priori surface NO_x emissions over East Asia are 11.6 and 11.1 Tg N/yr in cases A and B, respectively. The fossil fuel source accounts for > 90% of the totals. The distribution of the a priori surface NO_x emissions in case A is shown in Figure 3.1a. While the total emission amount is similar, the spatial correlation between these two inventories is moderate (R^2=0.4).

Figure 3.1b shows observed and simulated monthly mean tropospheric NO_2 columns over East Asia for July 2007. The model simulations show large NO_2 columns over East China, South Korea and Japan as observed. The difference between model simulations reflects the difference in fossil fuel combustion sources in cases A and B. It is clear that simulated spatial distributions over East China in both cases differ from the OMI measurements.

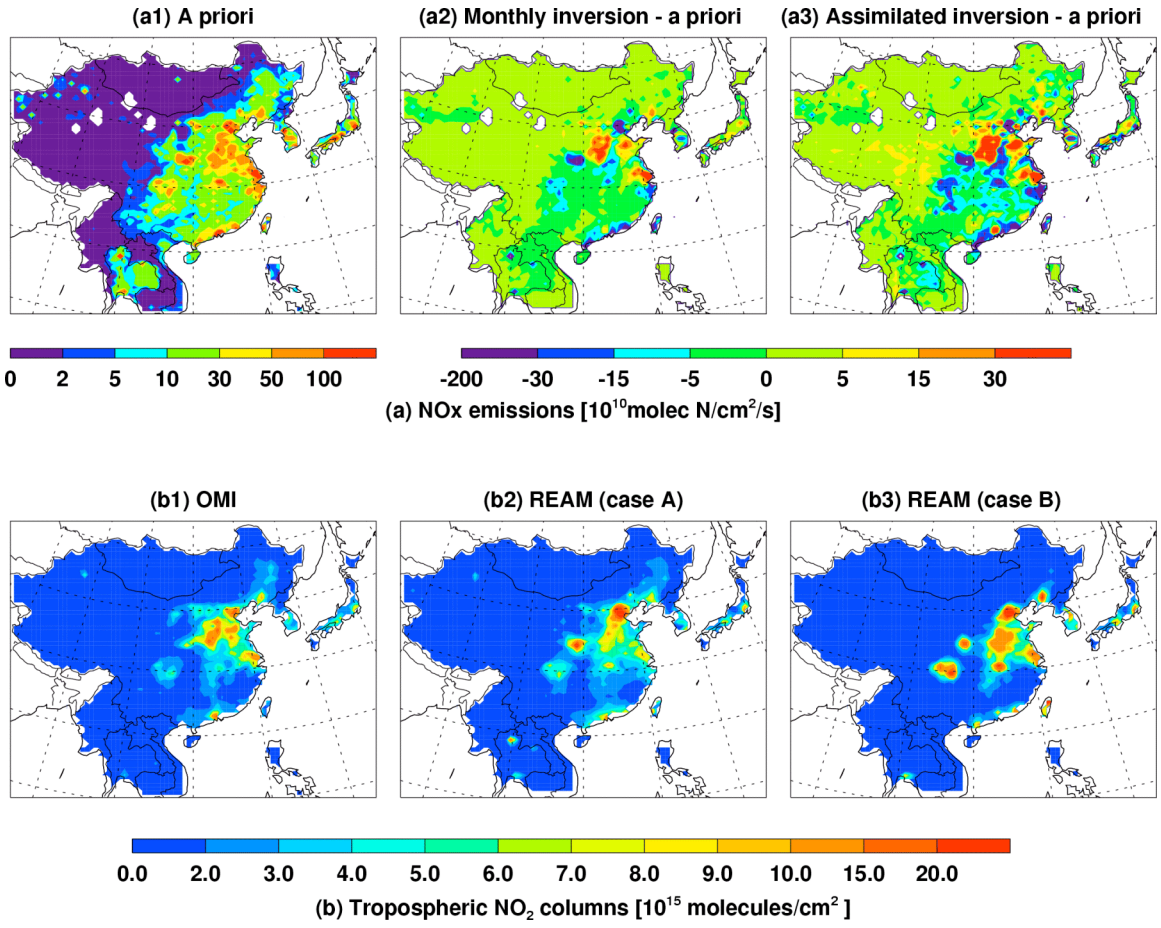

Figure 3.1 (a) A priori surface NO_x emissions (a1) for July 2007 in case A, and the corresponding changes in the a posteriori emissions from the a priori in the monthly (a2) and assimilated daily (a3) inversions. **(b)** Monthly mean tropospheric NO_2 columns over East Asia for July 2007 from OMI measurements (b1), and the corresponding REAM results with a priori NO_x emissions in case A (b2) and case B (b3). Only OMI data with cloud fractions of < 30% are used.

3.4.2 A posteriori surface NO_x emissions

We first apply previously used monthly-mean inversion method to estimate the top-down NO_x emission inventory by scaling the a priori emissions with the ratio of observed and simulated tropospheric NO_2 column in each grid box. The a posteriori emissions are then estimated as error weighted averages of the a priori and top-down emissions [e.g., Martin et al., 2003 and 2006; Y.X. Wang et al., 2007]. The uncertainty of the top-down emissions originates from the retrieval error (section 3.2) and the error of linking local NO_2 columns to local emissions on the basis of model simulations. The latter is estimated at 30% from Martin et al. [2003]. We compared the model simulated tropospheric NO_2 columns using either WRF or MM5 assimilated meteorological fields for July 2007. The monthly mean of absolute error is mostly < 30% with an average of 11% (Appendix B). The overall error of the top-down emissions over polluted areas is estimated at ~50%. The uncertainty of the a priori inventory is ~60% over the regions (section 3.3). Y.X. Wang et al. [2007] suggested that considering the contributions from non-surface sources (such as lightning and aircraft) as background NO_2 columns improves the top-down emission estimate. We follow the same approach here. The effect of lightning NO_x on inversion is small. In a sensitivity study, we use OMI measurements only when lightning NO_2 fraction is < 10% of the simulated tropospheric columns, the resulting a posteriori emissions do not change.

In the assimilated daily inversion, we use the same framework by Martin et al. [2003] outlined above. The inversion is applied daily using model results and OMI measurements to estimate the a posteriori emissions and errors. After the inversion, the updated emission inventory and its errors are used as the a priori in the model simulation

in the next day. Therefore, both the emission and its error are updated at the grids with OMI measurements each day. The weekend/weekday variation is accounted for in the inversion. The weekend/weekday emission ratios are initially set to be 1 and iteratively estimated through the daily inversion of OMI NO_2 measurements by comparing weekend emissions with weekdays. The computed ratios are used for the following weekend emissions. The ratio is as low as 0.7 over some urban regions, but is negligible over most regions of East China. The overall impact of the emission ratio deviations from 1 on the a posteriori NO_x emissions is small. The a posteriori emission convergence time scale is ~10 days (Appendix B). To further minimize the effect of single-day OMI measurements, we used the average of the a posteriori emissions (and their errors) of the last week as the a posteriori result of the assimilated inversion. More detailed description of the inversion procedure is provided in the auxiliary materials. Since the computer resource needed in the inversion is small compared to the 3-D model simulation, assimilated inversion does not increase the computing resource need.

We show here the difference between the a priori emissions and either monthly-mean or assimilated inversion results in case A (Fig. 3.1a). The assimilated inversion leads to more significant adjustments than the monthly-mean inversion. The total a posteriori surface NO_x emissions over East Asia are 11.2 and 11.0 Tg N/yr, respectively for monthly-mean and assimilated inversions, 3% and 5% less than the a priori total in case A (11.6 Tg N/yr). In case B (not shown), the total monthly-mean and assimilated a posteriori emissions are 9.8 and 10.6 Tg N/yr, respectively, 12% and 4% less than the a priori (11.1 Tg N/yr). The covariances (R^2 values) and root mean squared errors (RMSE) between simulated and OMI observed tropospheric NO_2 columns for July 2007 are listed

in Table 3.1. The inversions increase the R^2 values and decrease the RMSE compared to the a priori emissions. The assimilated inversion yields better statistics (R^2: 0.92; RMSE: 0.56-0.58x10^{15} molcecules/cm^2) compared to the monthly-mean inversions (R^2: 0.78-0.82; RMSE: 0.81-0.91x10^{15} molecules/cm^2). We find similar improvements when applying these a posteriori emissions to a different month of August 2007 (Table 3.1).

Table 3.1 Correlation statistics between OMI retrieved and REAM simulated tropospheric NO_2 columns with different surface NO_x emissions for July and August 2007.

	A priori				Monthly a posteriori[1]				Assimilated a posteriori[1]			
	Case A		Case B		Case A		Case B		Case A		Case B	
	Jul	Aug	Jul	Aug	Jul	Aug	Jul	Aug	Jul	Aug	Jul	Aug
R^2	0.61	0.54	0.53	0.48	0.82	0.81	0.78	0.76	0.93	0.90	0.92	0.90
RMSE (10^{15} molec/cm^2)	1.27	1.50	1.69	1.84	0.81	0.80	0.91	0.89	0.56	0.62	0.58	0.61

[1] The a posteriori emissions of NO_x of July are used in the simulations for August.

The spatial covariance between cases A and B improves to an R^2 value of 0.60 in the monthly-mean a posteriori emissions from 0.40 in the a priori emissions. In the assimilated inversions, the a posteriori emissions between the two cases are almost the same (R^2: 0.94), indicating that the assimilated inversion is insensitive to the a priori emissions unlike the monthly-mean inversion. In regions where a priori emissions are not known well, this is a significant advantage of the assimilated inversion method. The a posteriori emission uncertainties are reduced. The a posteriori error decreases until the emissions converge. 17% is estimated for the assimilated inversion compared to 60% and 36% for the a priori inventory and monthly-mean inversion, respectively. The uncertainty estimate for monthly inversion is an upper bound since we follow Martin et al. [2003] by assigning the daily retrieval error as the monthly-mean one.

3.4.3 Optimized fossil-fuel NO_x emission

Since the assimilated a posteriori NO_x emissions from two cases are almost the same, we use the assimilated a posteriori emissions in case A here. Partitioning between fossil fuel and soil emissions is not apparent from the column measurements. Since the change of total emissions is relatively small, we use the least-squares regression to linearly partition the a posteriori emissions based on the a priori fossil fuel and soil emissions, i.e., $E_{posteriori} = aE_{priori}^{fuel} + bE_{priori}^{soils}$ (more details in Appendix B). We obtain the a posteriori soil NO_x emissions of 1.6 Tg N/yr for July, a factor of 2.4 higher than the a priori value of 0.68 Tg N/yr. It accounts for ~14% of the total a posteriori emissions, significantly less than suggested by Y.X. Wang [2007] (Appendix B).

Subtracting the soil emissions, we obtain the a posteriori fossil fuel emissions. Over the regions with significant fossil fuel emissions, such as East China, the a posteriori emissions are essentially from fossil fuel combustion. The total a posteriori fossil fuel NO_x emission over East Asia is estimated as 9.5 Tg N/yr, 13% less than the a priori value of 10.9 Tg N/yr in case A. Table 3.2 lists the a priori and a posteriori total emissions over China, South Korea, Japan, and other countries in East Asia. Again the total emission change is relatively small. In both inventories, emissions from China account for ~80% of the regional total.

Table 3.2 A priori and assimilated a posteriori fossil fuel NO_x emissions over East Asia for 2007 (Tg N/yr).

	A priori	Assimilated a posteriori
China	8.48	7.48
South Korea	0.36	0.28
Japan	0.67	0.68
Other	1.40	1.03
Total	10.9	9.5

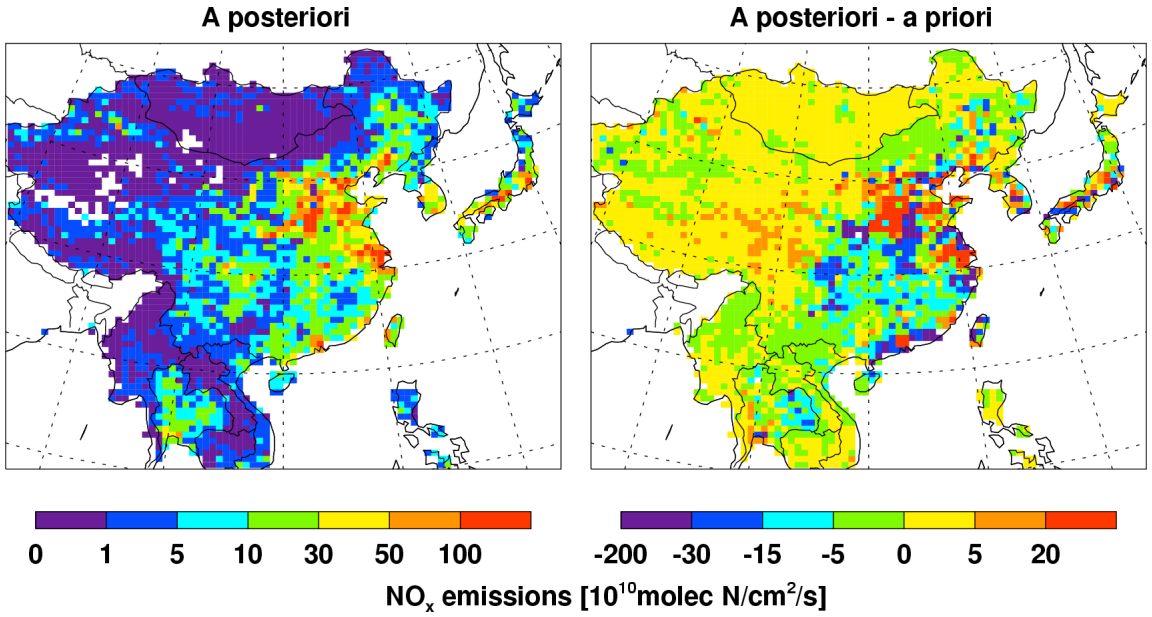

Figure 3.2 Assimilated a posteriori fossil fuel NO_x emissions over East Asia in case A (left), and the corresponding changes in the a posteriori emissions from the a priori (right).

The most significant change from the a priori emissions is in the spatial distribution. The a posteriori fossil fuel NO_x emissions and its spatial distribution changes from the a priori inventory are shown in Figure 3.2. Relative changes of 20-100% are found over the industrialized East China plains. Compared with the a posteriori results, the a priori inventory generally overestimates the emissions over the economically developed areas surrounding major urban centers and underestimates over the underdeveloped areas in East China. The bias likely reflects more stringent emission control policies and enforcements in urban regions and the presence of inefficient and unregulated local power and metallurgical plants in rural areas. A priori emissions from Shanxi, where coal production is prevalent, are underestimated throughout the province. A further study shows that the a posteriori emission distributions do not change if we expand the analysis period to other years (2005 and 2006) in summer.

3.5 Conclusions

We develop a new daily assimilated inversion method to improve the top-down constraints of NO_x emissions over East Asia based on OMI NO_2 measurements in July 2007. The iterative nature of the assimilated inversion accounts for the chemical feedbacks of NO_x emission changes and reduces the dependence of the a posteriori emissions on the a priori emissions, resulting in significant improvements over the monthly-mean inversion result. The spatial covariance (R^2) between observed and simulated NO_2 columns increases from 0.7-0.8 in monthly-mean inversion to 0.92; the RMSE is reduced by 30%. Similar improvements are found when these a posteriori emissions are applied to a different month. We find a relatively small contribution from

soil emissions, ~1.6 Tg N/yr or ~14% in July. Annualized contribution will be even smaller because of the temperature dependence of soil emissions. The assimilated a posteriori NO_x emissions from fossil fuel combustion over East Asia are 9.5 Tg N/yr, 13% lower than the a priori value of 10.9 Tg N/yr in case A. While the total emission change is small (less than the uncertainty of 17% in the assimilated a posteriori inventory), significant spatial distribution changes are found, especially over East China. The a priori fossil fuel NO_x emission inventory tends to overestimate the emissions over the economically developed areas and underestimate over the underdeveloped areas in East China. While the dichotomy of a prior inventory bias may indicate an issue with the bottom-up statistics used to derive the inventory, it may also reflect in part fossil fuel NO_x emission reductions resulting from the urban-centric air quality controls and enforcements in China.

CHAPTER 4

[3]EAST CHINA PLAINS: A "BASIN" OF OZONE POLLUTION

4.1 Introduction

Ozone (O_3), an important chemical compound of the earth's atmosphere, is a greenhouse gas contributing to global warming and poses health and ecology problems on the ground level [IPCC, 2007]. During the past two decades, the rapid economic growth in China results in a significant increase in the emissions of ozone precursors [e.g., Streets et al., 2000, 2003; Richter et al., 2005] and these emissions lead to the formation of elevated ozone near the surface. In recent years, more and more observations have found high ozone episodes in China, mostly over East China (110-120^{o}E, 25-42^{o} N) [e.g., Lam et al., 2001; Ma et al., 2002; Gao et al., 2005; Z. Wang et al., 2006; H. Wang et al., 2006].

East China hosts the economic engine of the country with > 60% of the industries and populations (Fig. 4.1a) and most of the major cities. Geographically, this region consists of three plains: North China Plain, Northeast Plain, and Chang Jiang Downstream Plain with high mountains and plateau to the west and ocean to the east (Fig. 4.1b). The elevation over most of the region is less than 200 m. A similar geographical feature exists over the "South Coast Basin" of California in the United States (US) (mountain regions to its east and ocean to its west). The "basin" feature contributes to

---

[3] This chapter is for "East China plains: A "basin" of ozone pollution" published in *Environmental Science and Technology* in 2009. Authors are C. Zhao, Y. Wang, and T. Zeng.

high ozone episodes there [Altshuller, 1983; Kumar et al., 1984]. As in the case of California, the East China plains also have large pollutant emissions [Street et al., 2003]. When the atmospheric circulation becomes favorable, widespread high ozone pollution can form over East China due to the recirculation of pollutants. Unlike the "South Coast Basin" of California, East China plains are much larger (> 1 million km^2) occupied by a larger population (> 800 million). Thus the environmental impact of ozone pollution is much greater. Unfortunately it is difficult to identify such "basin" feature of high ozone over East China since ground ozone monitoring sites in China are mostly in major cities and the measurement data are difficult to obtain for researchers outside China. In this work, we identify the "basin" feature using the simulations from a regional chemical transport model (REAM) and surface ozone measurements.

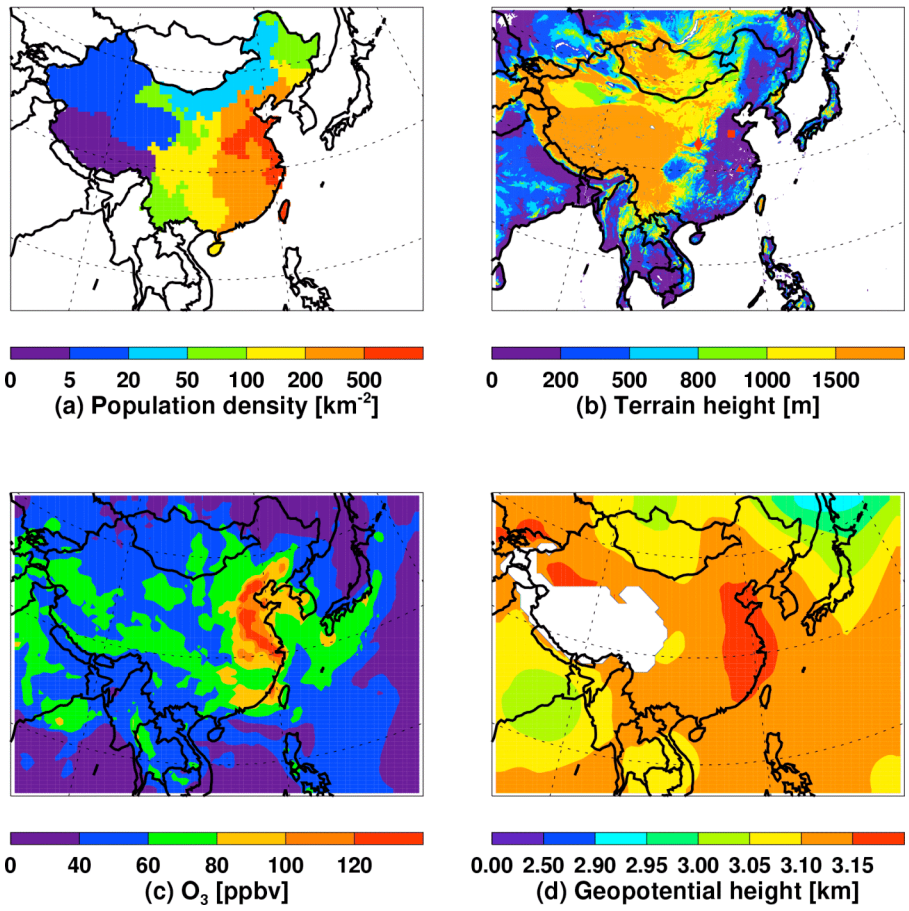

Figure 4.1 (a) Distribution of provincial population density in China in 2000; (b) Terrain height distribution over East Asia with a 5-km resolution. The red square, diamond, and triangle symbols represent the locations of Mt. Tai, Hua, and Huang, respectively; (c) Ground-level MDA8 ozone concentrations over East Asia on June 13 in 2004 from the VOC simulation; (d) Simulated 700-hPa geopotential height distribution on June 13.

4.2 Methods

4.2.1 Model

The 3-D regional chemical transport model (REAM) driven by MM5 assimilated meteorological fields was described by Choi et al. [2008a]. In this work, the REAM model is applied to ozone simulations over East Asia. The model has a horizontal resolution of 70 km with 23 vertical layers below 10 hPa. Meteorological fields are assimilated using MM5 constrained by the National Center for Environmental Prediction (NCEP) reanalysis products. The horizontal domain of MM5 has 5 extra grids beyond that of REAM on each side to minimize potential transport anomalies near the boundary. Most meteorological field inputs are archived every 30 minutes except those related to convective transport and lightning parameterizations, which are archived every 5 minutes. Chemical initial and boundary conditions for chemical tracers in REAM are obtained from the global simulation for the same period using the GEOS-CHEM model driven by GEOS-4 assimilated meteorological fields [Bey et al., 2001]. More detailed model description is provided in the supporting information.

4.2.2 Emissions

Biogenic emission algorithms and inventories are adapted from the GEOS-CHEM model [Choi et al., 2008a]. The anthropogenic emissions of tracers other than NO_x are taken from a recent bottom-up Asian emission inventory developed by Streets et al. for 2006 INTEX-B campaign (The detail can be obtained from http://www.cgrer.uiowa.edu/EMISSION_DATA_new/index_16.html). Anthropogenic NO_x emissions for 2004 are obtained by scaling the NO_x emissions derived in Chapter 3 for 2007 over East Asia with an annual increasing rate of 8% in China. The NO_x and CO

emissions from biomass burning are obtained from the Global Fire Emissions Database, Version 2 (GFEDv2.1) [Randerson et al., 2005].

Figure 4.2 compares the anthropogenic NO_x emissions over China to the US in 2004. The anthropogenic NO_x emission over the US is prepared by Sparse Matrix Operator Kernel Emissions (SMOKE) model (http://cf.unc.edu/cep/empd/products/smoke/index.cfm) for 2004 projected from the VISTAS 2002 US emission inventory. The estimated total NO_x emission over China is 6.2 Tg/yr, 20% higher than 5.2 Tg/yr over the US. While high NO_x emissions are mostly over major metropolitan regions over the US, high NO_x emissions are more spatially spread over East China, corresponding roughly to the connected China plains shown in Figure 4.1b.

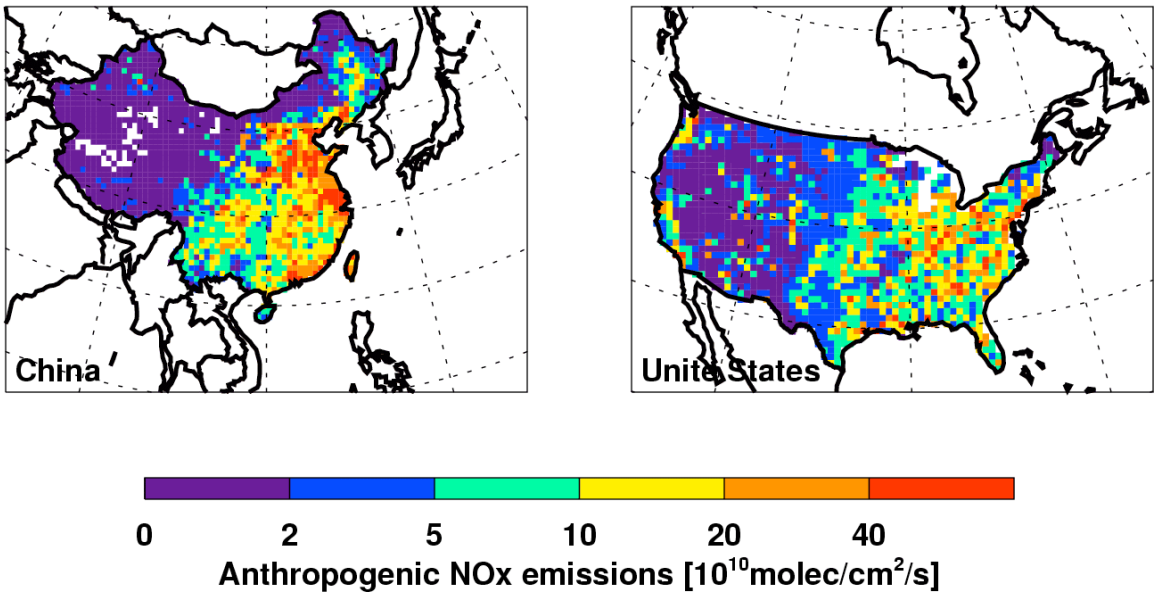

Figure 4.2 Distributions of anthropogenic NO_x emissions over China (left) and the United States (right) in 2004.

4.3 Results and Discussion

4.3.1 East China plains as a large ozone "basin"

In this work, we identify the "basin" feature using the simulations from a regional chemical transport model (REAM) [Choi et al., 2008a]. Measurements from three mountain (Mt.) sites over East China, Mt. Tai (117.10°E, 36.25°N, 1533 m above sea level (a.s.l), center of East China), Mt. Hua (110.09°E, 34.49°N, 2064 m a.s.l, west edge of East China), and Mt. Huang (118.15°E, 30.13°N, 1836 m a.s.l, south of East China) (Fig. 4.1b) [Z. Wang et al., 2006; J. Li et al., 2007] are used to confirm that the model simulations generally capture the observed pollution episodes. A larger episode on June 9-14 in 2004 is analyzed in this study. While the observation sites are limited, they do represent the regional feature of ozone over East China since they triangulate over the region and the sites at 1.5-2 km are high enough to avoid the influence of local pollutant

emissions or distribution features. The model simulation shows high ozone concentrations (> 80 ppbv) covering the East China plains in the June episode (Fig. 4.1c). The meteorological condition during this episode is typical for ozone episodes, a high pressure system controlling the region, which prevents the ventilation of ozone precursors (Fig. 4.1d).

The ozone measurements in May at the mountain sites were previously published [Z. Wang et al., 2006; J. Li et al., 2007] and were used in the model evaluation (Appendix C). The model errors for ozone simulation are within the recommended ranges of the U.S. Environmental Protection Agency (EPA) (Appendix C). The standard model simulation shows the general characteristics of the high ozone episodes in May, but significantly underestimates some ozone peaks during the episodes at the Mt. Tai, even though it captures the general timing of the episodes.

Ozone is produced by NO_x ($NO+NO_2$) in the presence of volatile organic compounds (VOCs). The emissions of NO_x over East China used in this model are constrained by satellite measurements (Appendix B). Anthropogenic emissions of VOCs, which include a large number of species, are subject to a much higher degree of uncertainty (~130%) over Asia [Streets et al., 2003]. Underestimation of VOCs emissions leads to underestimation of regional ozone [Y. Wang et al., 1998]. Our modeling analysis of observed NO, peroxyacetal nitrate (PAN), and VOCs in Beijing in August 2007 suggests that the model greatly underestimates VOCs that lead to PAN formation (not shown). Therefore, more VOCs are added in the model (hereafter referred to as the VOC simulation) in the form of methylglyoxal (MGLY) with the same emission distribution as propene over China. MGLY is produced from the oxidation of many VOCs and is an

effective PAN precursor. In a previous model analysis, it was significantly underestimated over urban regions such as those in East China compared to limited in-situ and satellite measurements [Fu et al., 2008]. The scaling factor of MGLY to propene emissions is determined such that PAN simulated in the model in Beijing is in agreement with the measurements. The additional MGLY emission improves the ozone simulations (next section) but its impact on the results presented in this study is limited (Appendix C).

The evaluation shows that the model performance at Mt. Tai is improved in VOC simulations, especially in producing the high ozone peaks (Appendix C). The effects at the other two mountain sites are insignificant, because ozone production in regions around these sites is sensitive to NO_x emissions whereas ozone production around Mt. Tai is sensitive to VOC emissions (next section). Therefore, we use the modeling results from the VOC simulation in this study. In the results shown, the difference between the VOC and standard simulations are small except the intensely polluted areas such as the vicinity of Beijing (Appendix C) where ozone production is sensitive to VOC emissions (next section). Due to the restriction of the agreement between two institutes in China and Japan, we were asked not to show the measurement data in June in this work. The model performance during the June episode is similar to that shown for May, and the simulated results are also better correlated with the measurements with the correlation coefficients of 0.60, 0.54, and 0.80 for Mt. Tai, Hua, and Huang, respectively.

The simulated hourly ozone concentrations at three mountain sites on June 5-16, 2004 are shown in Figure 4.3. Among the three mountain sites, Mt. Tai is located in an area with a high population density (Fig. 4.1a) and the regional emissions nearby are also higher (Fig. 4.2). Ozone exceeds 80 ppbv from June 9 to 14, reaching up to 120 ppbv.

The VOC simulation has higher ozone concentrations than in the standard simulation especially during the high ozone episode because of ozone production sensitivity to VOCs in the surrounding area. The rapid decrease of ozone to 50 ppbv on June 15 is driven by the onset of Asian summer monsoon [J. Li et al., 2007], when relatively clean maritime air is transported to the region. Mt. Hua is located at the western edge of the Northeast Plain. The surrounding population and regional emissions are lower than the other two sites. As a result, the average ozone concentrations during the episode from June 9 to 14 are lower than Mt. Tai. Mt. Huang is located to the south of the Chang Jiang Downstream Plain. The model simulation shows that the episode started in the northern plains and then migrated southward. As a consequence, ozone concentrations at Mt. Huang are significantly higher on June 12-14 than the first half of the episode, reaching a maximum of ~140 ppbv, much higher than the summer average of ~45 ppbv [J. Li et al., 2007].

We also conducted another simulation, in which anthropogenic NO_x emissions over China are removed in the model. In this sensitivity simulation, O_3 concentrations mainly reflect the transport of ozone produced in the other regions of the world and from the stratosphere and are significant lower than the standard simulation. It demonstrates that the high ozone episodes are not driven by ozone transport from the regions outside China or the stratosphere but from the ozone production inside China. The larger impact of anthropogenic NO_x emissions at Mt. Huang than Mt. Tai reflects in part ozone production sensitivity to NO_x emissions in areas around Mt. Huang, whereas ozone production around Mt. Tai is more sensitive to VOC emissions (next section). The local ozone production sensitivity is modulated by regional recirculation of ozone.

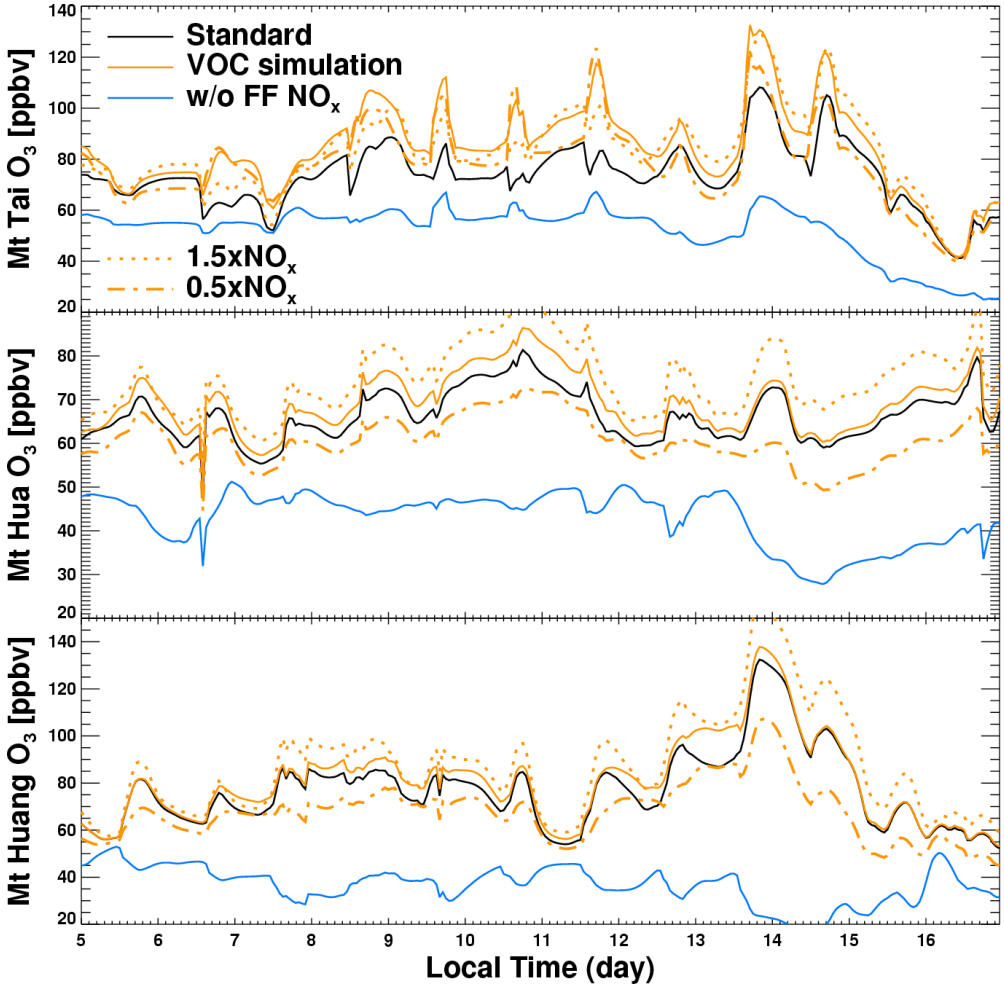

Figure 4.3 Simulated hourly O_3 concentrations on June 5-16 in 2004 at three mountain sites (top to bottom: Mt. Tai, Hua, and Huang). Five model results are shown: the standard simulation (black line), three VOC simulations (standard - solid orange line, 50% increase of Chinese NO_x emissions - dotted orange line, and 50% decrease of Chinese NO_x emissions – dashed orange line), and the simulation without anthropogenic NO_x emissions over China (blue line).

The high ozone peaks (up to 140 ppbv) at the mid night of June 14 at the three mountain sites are simulated as observed. These high ozone peaks at mid night reflect the amounts of high ozone produced photochemically on June 13 in polluted regions. The spatial distribution of the maximum daily 8-hour average (MDA8) ozone concentrations on June 13 over China from the VOC simulation is shown in Figure 4.1c. The ozone "basin" feature of East China is evident. The whole East China suffers from high ozone concentrations with average MDA8 value of 93 ppbv, which normally occurs in the urban and suburban regions in the U.S. [NARSTO]. This episode is fostered by the synoptic meteorological condition. A high pressure system locates over East China from June 11 to 13 (Fig. 4.1d). Under the control of the stable high pressure system which suppresses the ventilation of pollutants from the boundary layer, photochemistry produces large amounts of ozone in the polluted regions, and the meteorological condition favors the recirculation of high ozone through the connected East China plains.

4.3.2 Effectiveness of NO_x emissions control

Ozone production is driven mainly by NO_x and volatile organic carbons (VOCs). Photochemically, ozone production is either sensitive to NO_x emissions or to VOCs emissions. One way to diagnose the ozone production sensitivity is through the ratio of CH_2O/NO_y [Sillman, 1995], where NO_y is the sum of total reactive nitrogen. The critical value determined by Sillman et al. [1995] is 0.28. Above this value, ozone production is sensitive to NO_x emissions; otherwise, it is sensitive to VOC emissions. Figure 4.4 shows that the simulated CH_2O/NO_y ratios are > 0.6 over most regions of East China except the intensely polluted areas such as the vicinity of Beijing, indicating ozone production over a large part of East China is sensitive to NO_x emissions. Both standard and VOC

simulations show similar results (Appendix C). The NO_x-sensitive region over China is consistent with Tie et al. [2007] in summer. Ozone at Mt. Tai located in the VOC-sensitive region is less sensitive to NO_x emissions than at the other two mountain sites located in the NO_x-sensitive region (Fig. 4.3).

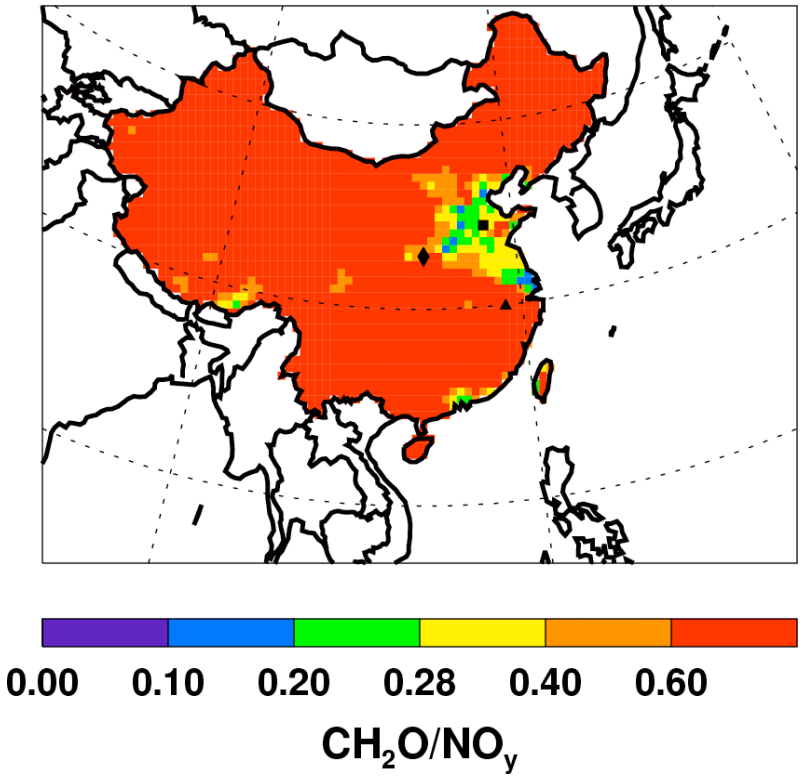

Figure 4.4 REAM simulated mean daytime ratios of CH_2O/NO_y for June 2004 over China in the VOC simulation. The black square, diamond, and triangle symbols represent the locations of Mt. Tai, Hua, and Huang, respectively.

We apply the model to evaluate the effectiveness of reducing NO_x emissions in controlling regional ozone over East China. The changes of the MDA8 ozone concentrations from two sensitivity results (Case 1: increasing anthropogenic NO_x emissions by 50%; Case 2: decreasing by 50%) from the VOC simulations are shown in Figure 4.5. Both the magnitude and the coverage of the high ozone over the East China plains on June 13 are significantly affected by the change of the NO_x emissions, since ozone production over most regions of East China are sensitive to NO_x emissions. The MDA8 ozone concentrations over East China change by +9% (an increase of 5-15 ppbv) and -16% (a decrease of 10-40 ppbv) with 50% increase and decrease of anthropogenic NO_x emissions, respectively. More sensitive to NO_x emissions than MDA8 ozone concentrations are the areas affected by high ozone concentrations. If we use the U.S. EPA MDA8 ozone standard of 75 ppbv, the areas with high ozone concentrations correspond linearly and increase or decrease by 50% from 1.3 million km^2 as the changes of the anthropogenic NO_x emissions in the model.

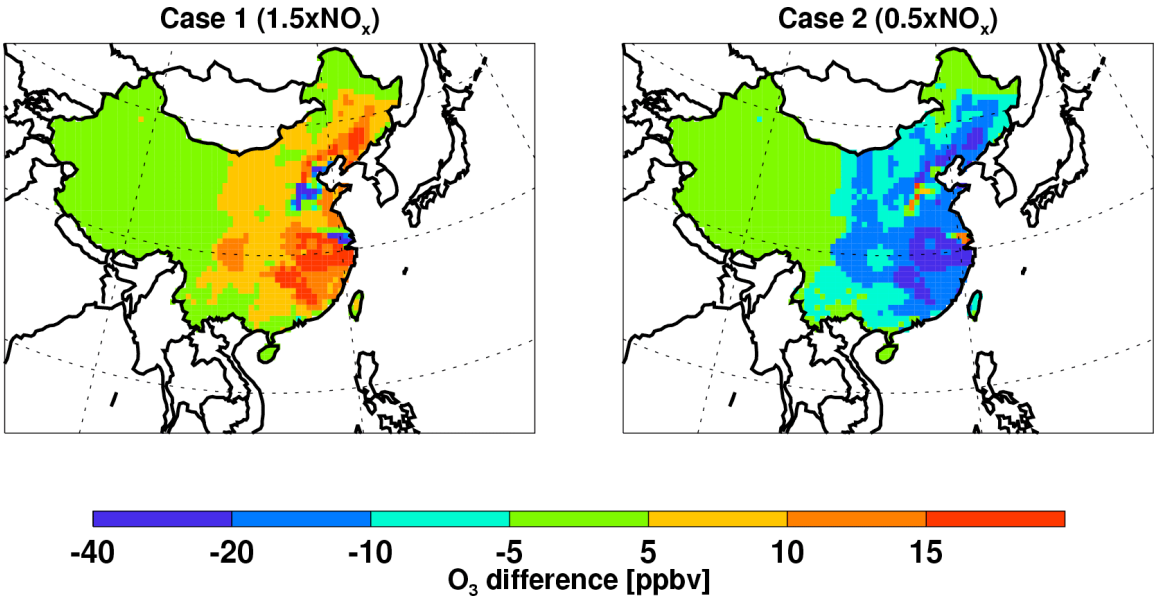

Figure 4.5 Changes of ground-level MDA8 O_3 concentrations over China on June 13 in 2004 from the VOC simulations by increasing (Case 1) or decreasing (Case 2) the anthropogenic NO_x emissions over China by 50%.

4.4 Conclusion

Satellite measurements indicate the NO_x emissions over East China have been increasing at an annual rate of 6-10% [Richter et al., 2005; Zhang et al., 2007]. The estimated total fossil fuel NO_x emission in China is 35% higher than in the U.S. in 2004. The high emission regions in China are more widespread than in the United States. The geographically flat East China plains coupled with high anthropogenic emissions lead to high-ozone episodes, which affect > 60% of the population in China. The "basin" feature of the connected plains allows the recirculation of pollutants over the high-emission

regions under high-pressure systems. Model sensitivities indicate that ozone concentrations are very responsive to NO_x emission reductions in terms of high-ozone areas and hence population exposure.

CHAPTER 5

[4]IMPACT OF EAST ASIAN SUMMER MONSOON ON THE AIR QUALITY OVER CHINA: THE VIEW FROM SPACE

5.1. Introduction

During the past two decades, the rapid economic growth in China results in a significant increases in the pollutant emissions [Streets et al., 2000, 2003; Richter et al., 2005]. These emissions lead to the formation of elevated concentrations of pollutants (e.g., O_3 and CO) near the surface mostly over East China, which hosts the economic engine of the country and most of the major cities [e.g., Wei et al., 1999; Ma et al., 2002; H. Wang et al., 2006; Zhao and Y. Wang, 2009; Zhao et al. 2009a]. Pollutant distributions are strongly affected by atmospheric circulations. In East Asia, summer monsoon is a major atmospheric system affecting air-mass transport, convection, and precipitation in China [Hoskins and Rodwell, 1995; Rodwell and Hoskins, 2001; Ding et al., 2005].

Surface observations in limited locations showed that the ground O_3 levels over East China could be strongly perturbed by the monsoonal flow with clean oceanic air-mass transported from the tropical Pacific in summer [e.g., Tanimoto et al., 2005; Z. Wang et al., 2006; Li et al, 2007; He et al., 2008]. Tanimoto et al. [2005] analyzed the surface O_3 seasonality observed at the Acid Deposition Monitoring Network in East Asia

[4] This chapter is for "Impact of East Asian summer monsoon on the air quality over China: The View from space" to be submitted to Atmospheric Chemistry and Physics in 2009. Authors are C. Zhao, Y. Wang, Q. Yang, R. Fu, and Y. Choi.

(EANET) sites and Li et al. [2007] analyzed observations at three mountain sites in central East China. Both found a late spring/early summer maximum followed by a summer minimum in surface O_3 concentrations over East China. The rapid decrease of surface ozone in May-June period in Southeast China results from the onset of East Asian Monsoon in the region.

In contrast to East China, surface observations at Mount Waliguan (WLG) (36.3^{o}N and 100.5^{o}E) station, located in a remote region on the northeastern boundary of the Qinghai-Tibetan plateau over West China, has a clear summer maximum [e.g., Zhu et al., 2004; T. Wang et al., 2006]. Several mechanisms were proposed. Zhu et al. [2004] analyzed the surface O_3 measurements at the WLG station with a 3-D chemical transport model and concluded that high O_3 in summer over West China is due to monsoonal transport from East China and long-range transport from South/Central Asia and even Europe. On the other hand, analysis of back trajectories and surface measurements of O_3, CO and NO_y by T. Wang et al. [2006] and Ding and T. Wang [2006] suggested that downward transport of the upper tropospheric and stratospheric air masses is the main contributor to high summer O_3 over West China.

A number of studies making use of recently available satellite measurements examined the impacts of East Asian monsoon systems (including India monsoon) on tropospheric composition, particularly in the upper troposphere [e.g., Randel and Park, 2006; Fu, et al., 2006; Jiang, et al., 2007; Park, et al., 2007]. Randel and Park [2006] found that convection associated with the Asian monsoon transport air mass of low O_3 and high water vapor from the marine boundary layer into the upper troposphere based on the Aura AIRS data. Jiang et al. [2007] showed that deep convection associated with the

Asian monsoon lofts boundary layer air with high CO concentrations into the upper troposphere through analysis of the Aura MLS data.

In this work, we investigate the impact of the East Asian summer monsoon on the air quality over China using the O_3 and CO measurements from several satellite instruments, the MOPITT instrument on board the NASA Terra satellite, and the Ozone Monitoring Instrument (OMI), the Microwave Limb Sounder (MLS), and the Tropospheric Emission Spectrometer (TES) onboard the NASA Aura satellite. We examine the observed temporal and spatial variations of O_3 and CO distributions and their relationships to the onset and migration of monsoon circulation over China in summer 2006. To further interpret the satellite measurements, we apply the Regional chEmical and trAnsport Model (REAM) driven by assimilated meteorology by the Weather Research and Forecasting (WRF) model to simulate monsoon impact on regional circulation and pollutant distributions.

5.2 Satellite Measurements

5.2.1 GPCP 1-Degree Daily precipitation dataset

The 1-Degree Daily (1DD) precipitation data are available from the GPCP Global Merge Development Center in the NASA/GSFC Laboratory for Atmospheres. The data are estimated at one-degree daily resolution from multi-satellite observations [Huffman et al., 2001]. The current dataset extends from October 1996 to present. The primary product in the 1DD dataset is a combined observation-only dataset.

5.2.2 MOPITT Tropospheric CO columns

The MOPITT instrument on board the NASA Terra satellite is capable of globally CO monitoring. The satellite passes over the equator at around 10:45 am and 22:45 pm local time, and the horizontal resolution of MOPITT is 22x22 km^2. The measurements at nighttime are excluded in the study due to their large uncertainties. When compared with the measurements, the REAM model results are processed with the MOPITT retrieval averaging kernels [Deeter et al., 2003].

5.2.3 TES CO and O_3

TES is onboard the NASA Aura satellite [Beer et al., 2001], which passes over the equator at 1:45 pm local time. The nadir horizontal resolution of TES is 5x8 km^2. TES CO and O_3 data are obtained from the NASA Langeley Atmospheric Science Data Center (ASDC). This analysis uses TES data taken during the summer 2006 in global survey mode, the sampling for which is one observation every 160 km with 16 orbits per survey, over a time period of 12 hours [Beer, 2006]. For O_3, only those data for which the degrees-of-freedom of signal for the lower troposphere below 700 hPa is 0.2 or larger are selected to ensure that the estimate is sensitive to the boundary layer. Furthermore, the O_3 data with "C-Curve" shape are screened [TES user-guide v3.1]. When compared with the measurements, the REAM results are processed with TES retrieval averaging kernels for CO and O_3 respectively to account for the different sensitivities and a priori information of TES retrievals to different pressure levels [Jones et al., 2003]. The resulting transformed model profile can then be directly compared with TES retrievals without bias associated with the TES a priori information and vertical resolution [Zhang et al., 2006; Jourdain et al., 2007; Worden et al., 2007].

5.2.4 OMI-MLS Tropospheric O_3 columns

OMI and MLS are onboard the NASA Aura satellite, which passes over the equator at 1:45 pm local time. The nadir horizontal resolutions of OMI and MLS are 13x24 km^2 and 30x150 km^2, respectively. The tropospheric O_3 columns are derived using a residual method by estimating the stratospheric O_3 columns using MLS O_3 profiles above 215 hPa and subtracting that amount from OMI level 2 total column O_3 [Yang et al., 2007]. The MLS data are used for the derivation of OMI-MLS tropospheric O_3 columns. The mid-latitude stratospheric O_3 columns between 215 hPa and the tropopause are obtained by SAGE II mapping; the altitudes of the tropopause are taken from the NCEP reanalysis data [Yang et al., 2007]. The coincidence criteria for MLS stratospheric columns with OMI total column measurements are 1.25^o x 1.25^o on the same day. The tropospheric O_3 columns are derived in free cloud condition in this study. The detailed validation of the OMI-MLS tropospheric column O_3 products was performed by Yang et al. [2007].

5.3 Model Description

The REAM model driven by MM5 assimilated meteorological fields (using the NCEP reanalysis) is described by Choi et al. [2008a]. In this work, we use the modified REAM that is driven by WRF assimilated meteorological fields based on NCEP reanalysis as Zhao et al. [2009b]. Previously, this model was applied to investigate a number of tropospheric chemistry and transport problems at northern mid latitudes [Choi et al., 2005 and 2008a,b; Jing et al., 2006; Y. Wang et al., 2006; Guillas et al., 2007; Zhao et al., 2009a] and in the polar regions [Zeng et al., 2003 and 2006; Y. Wang et al., 2007].

The REAM model has a horizontal resolution of 70 km with 23 vertical layers below 10 hPa. The time steps for transport and chemistry are 5 minutes and 1 hour, respectively. Most meteorological inputs in REAM are updated every 30 minutes except those related to convective transport, which are updated every 5 minutes. The horizontal domain of WRF has 5 extra grids beyond that of REAM on each side to minimize potential transport anomalies near the boundary. Initial and boundary conditions for chemical tracers in REAM are obtained from the global simulation for the same period using the GEOS-CHEM model with assimilated meteorology (GEOS-4) [Bey et al., 2001]. For our analysis period, the lateral boundary CO columns from GEOS-CHEM simulations are lower than the MOPITT measurements (likely due to an underestimation of biomass burning emissions). We therefore scale the lateral boundary GEOS-CHEM results such that the resulting lateral boundary CO columns are consistent with MOPITT observations.

Biogenic emission algorithms and inventories are adapted from the GEOS-CHEM model [Y. Wang et al., 1998]. The lightning NO_x emission is parameterized as Choi et al. [2008b]. The anthropogenic emissions of tracers other than NO_x are taken from a recent bottom-up Asian emission inventory developed by *Streets et al.* for 2006 INTEX-B campaign (The detail can be obtained from http://www.cgrer.uiowa.edu/EMISSION_DATA_new/index_16.html). Anthropogenic NO_x emissions for 2006 are obtained by scaling the NO_x emissions derived by for 2007 over East Asia with an 8% annual rate of increase in China [Zhao and Wang, 2009]. The NO_x and CO emissions from biomass burning are obtained from the Global Fire Emissions Database, Version 2 (GFEDv2.1) [Randerson, et al., 2005].

5.4 Results and Discussion

5.4.1 Onset of the East Asian summer monsoon over East China

In order to access the monsoon impact on the air quality over East China, the examination of the dates and regions of the East Asian summer monsoon onset is necessary. The monsoon index, based on considerations of thermodynamics and dynamics from different aspects, such as pressure, ocean-land temperature contrast, wind field, precipitation, and so on, has been widely used to objectively delimit the monsoon extent and quantify its variability in monsoon regions. There have been a lot of studies putting the effort to define proper indices of the East Asian summer monsoon onset and each index places emphasis on some specific physical processes and represents its own meanings different to others [e.g., Li et al., 2002; Huang et al., 2004; Zhang et al., 2004].

In this study, following the principles from B. Wang and Lin [2002] and Zhang et al. [2004], we define the East Asian summer monsoon index to determine the monsoon regions and investigate the onset process of the monsoon using a criteria of: 1) a zonal vertical wind shear with low-level (e.g., 850 hPa) southerlies and upper level (e.g, 300 hPa) northerlies; 2) a period mean of rainfall > 6 mm/day. Based on this index, the monsoon onset is not determined only by rainfall, but also based on the establishment of a monsoon-related circulation, which is characterized by a change in the zonal vertical shear. Ding et al. [2005] summarized the East Asian summer monsoon onset as a process with several stages and each stage with the time scale less than one month. So we define the index on the basis of grid-by-grid calculations with half-monthly mean of the wind fields and rainfall.

Figure 5.1 shows the half-monthly index of the East Asian summer monsoon onset over East China from May to August 2006. The red dots in the figure indicate the location with the monsoon onset. The stages of the East Asian summer monsoon onset are very clear. East Asian summer monsoon reaches South China since the second half of May, and then initiates the rainy season over Southeast and East-central China in June. It advances northward up to Northeast China and becomes dominant over the entire of East China in July. The monsoon retreats back from Northeast China since the first half of August, and wanes in the end of August. The processes of the East Asian summer monsoon onset in 2006 are generally consistent with previous studies summarized by Ding et al. [2005].

East Asian summer monsoon onset is always accompanied by the occurrence of heavy rainfall. Figure 5.2 shows GPCP observed and WRF simulated time-latitude cross-section of 5-day average daily precipitation over East China (110-120^{o} E) from May to August in 2006. The heavy rainfall over Southeast China commences in early May, which is not driven by the monsoon [Zhang et al., 2004; Ding et al., 2005]. The monsoon driven steep rise in precipitation starts from mid May over Southeast China. This rainy episode over Southeast China continues into mid June. Afterwards, it rapidly shifts to East-central China and lasts for ~20 days. From July 5th, the rainy season revives over Southeast China, with a gap of a time period of 15 days between the first and this rainy episode that is mainly caused by typhoons, the movement of the ITCZ and other tropical disturbances in the monsoonal air flow [Ding et al., 2005]. From mid July, the rain belt moves to Northeast China, the northernmost position of summer monsoon rainfall. This rainy season persists over Northeast China for around one month. In the mid August, the

rainy season comes to the end, with the major monsoon driven rainy season disappearing. Since then, most part of East China is dominated by a dry spell [Ding et al, 2005]. WRF successfully simulates the observed precipitation pattern. The photochemical processing within the boundary layer is significantly constrained during the rainy season (section 5.4.3).

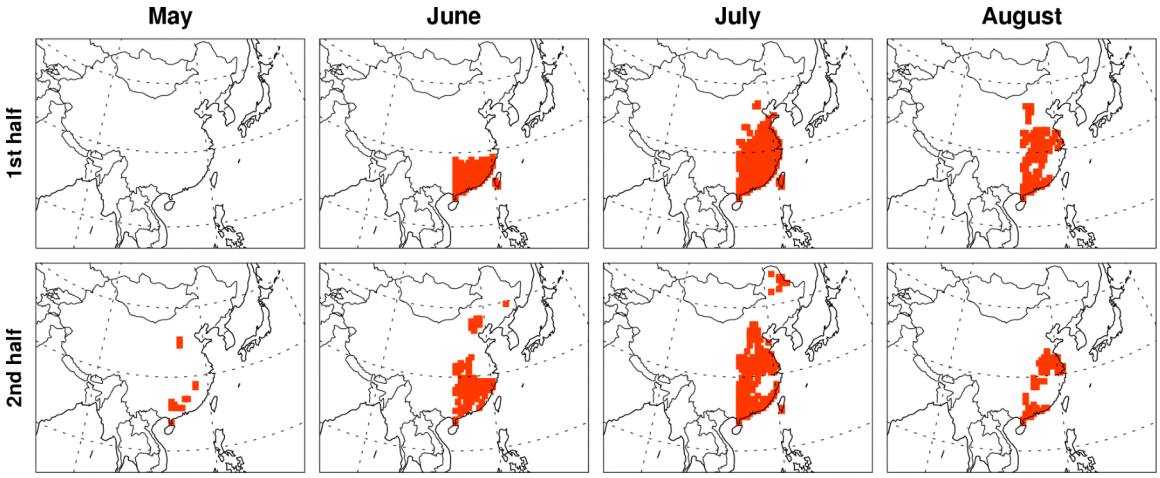

Figure 5.1 Advance of the East Asian summer monsoon onset over East China denoted by the monsoon indices (red squares) from May to August in 2006. The indices are calculated on the basis of half month.

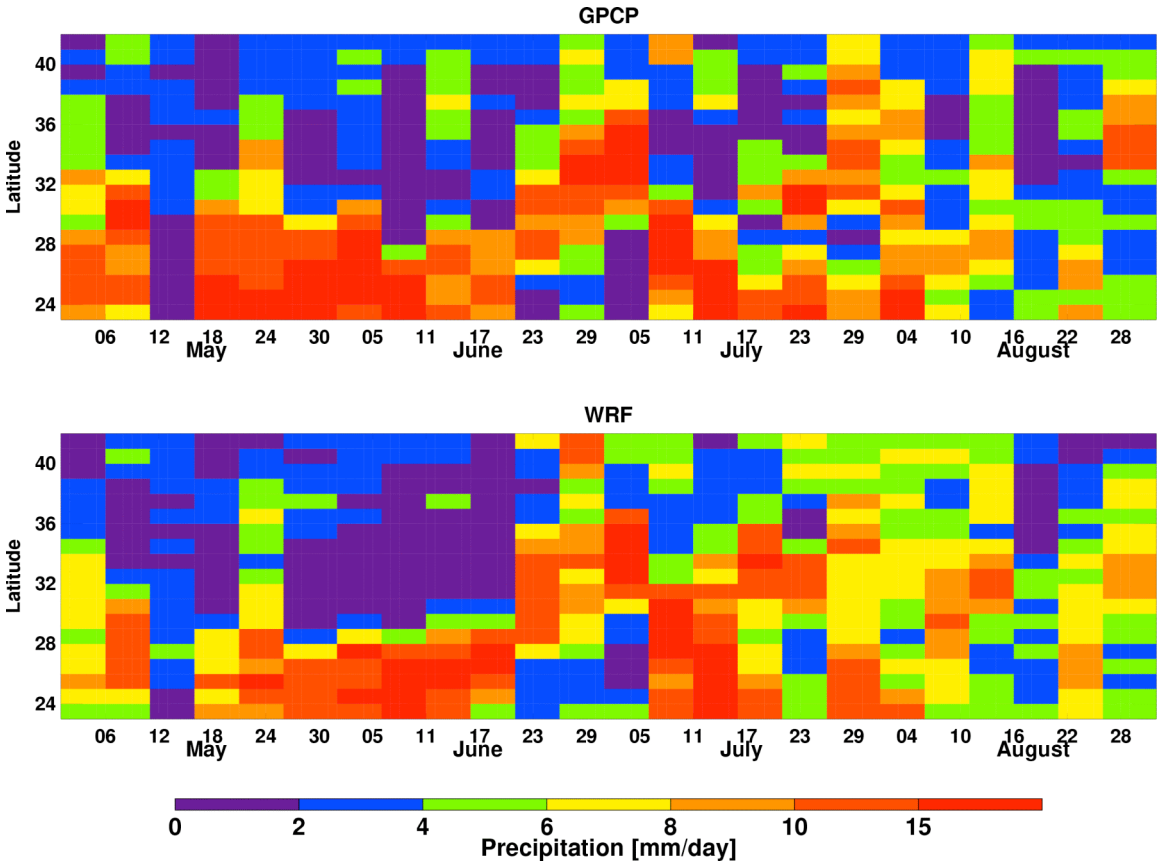

Figure 5.2 Time-latitude cross section of GPCP satellite observed and WRF simulated 5-day average of daily precipitation over East China (110^{o}-120^{o} E) from May to August in 2006.

5.4.2 Impact of East Asian summer monsoon on tropospheric CO

Figure 5.3 shows the monthly mean tropospheric CO columns retrieved from MOPITT and the corresponding model simulations from May to August in 2006. The REAM model successfully captures the variations of the tropospheric CO columns measured by MOPITT with the correlation coefficient of 0.7-0.75 and the mean bias within 5%. Both the measurements and the model simulations indicate the high CO columns with the mean of 2.3×10^{18} molecules/cm^{-2} over East China, Korea, Japan, and North Pacific Ocean in May due to the CO emissions from the anthropogenic sources and the fires over Siberia. When the monsoon comes in and becomes dominant over Southeast China in June (Fig. 5.1), the enhancement of CO columns disappears over the region due to the mixing with the monsoonal inflow of the oceanic air with lower CO concentrations. Following the northward migration of the monsoon (Fig. 5.1), the CO columns over East-central and Northeast China are also significantly reduced in July (Fig. 5.1). During the northward advance of the monsoon in June and July, the mean CO columns over East China decrease by up to 35%. The high CO columns re-emerge over East China in August when the monsoonal inflow becomes weaker (Fig. 5.1).

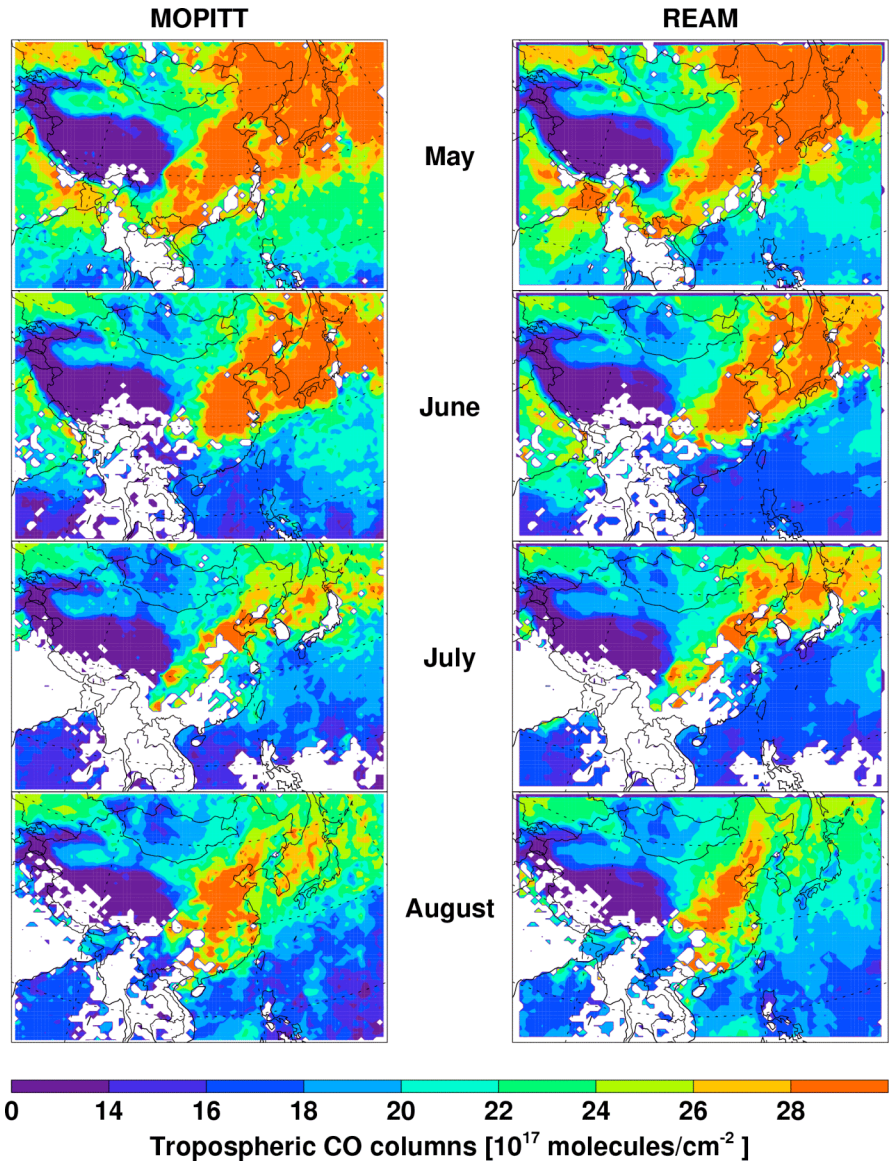

Figure 5.3 Monthly mean tropospheric CO columns retrieved from MOPITT and the corresponding REAM simulations from May to August in 2006. The model results have been processed with the MOPITT averaging kernel.

Figure 5.4 shows the comparison of TES retrieved and model simulated vertical distribution of CO mixing ratios from May to August in 2006 of the longitudinal mean of 110-120^{o} E between 20^{o}N and 40^{o} N latitude; this is the region covering East China. All data are interpolated to a latitudinal grid of 2 degrees and vertical grid of 100 hPa from 1000 to 300 hPa. The simulated CO concentrations are generally consistent with the measurements, but the mean is lower up to ~10%, probably from the underestimation of the anthropogenic CO emissions over China. The distribution of the CO concentrations and its variation from May to August is consistent with the MOPITT measurements (Fig. 5.3). The boundary layer CO concentrations drop by ~25% from 160 ppbv in May to ~120 ppbv in June and July over Southeast China, and increase to 140 ppbv in August. The monsoon driven decrease of the CO concentrations mainly occurs in the boundary layer. The boundary layer CO concentrations in Northeast China are much higher than that in Southeast due to the higher anthropogenic CO emissions over the Northeast.

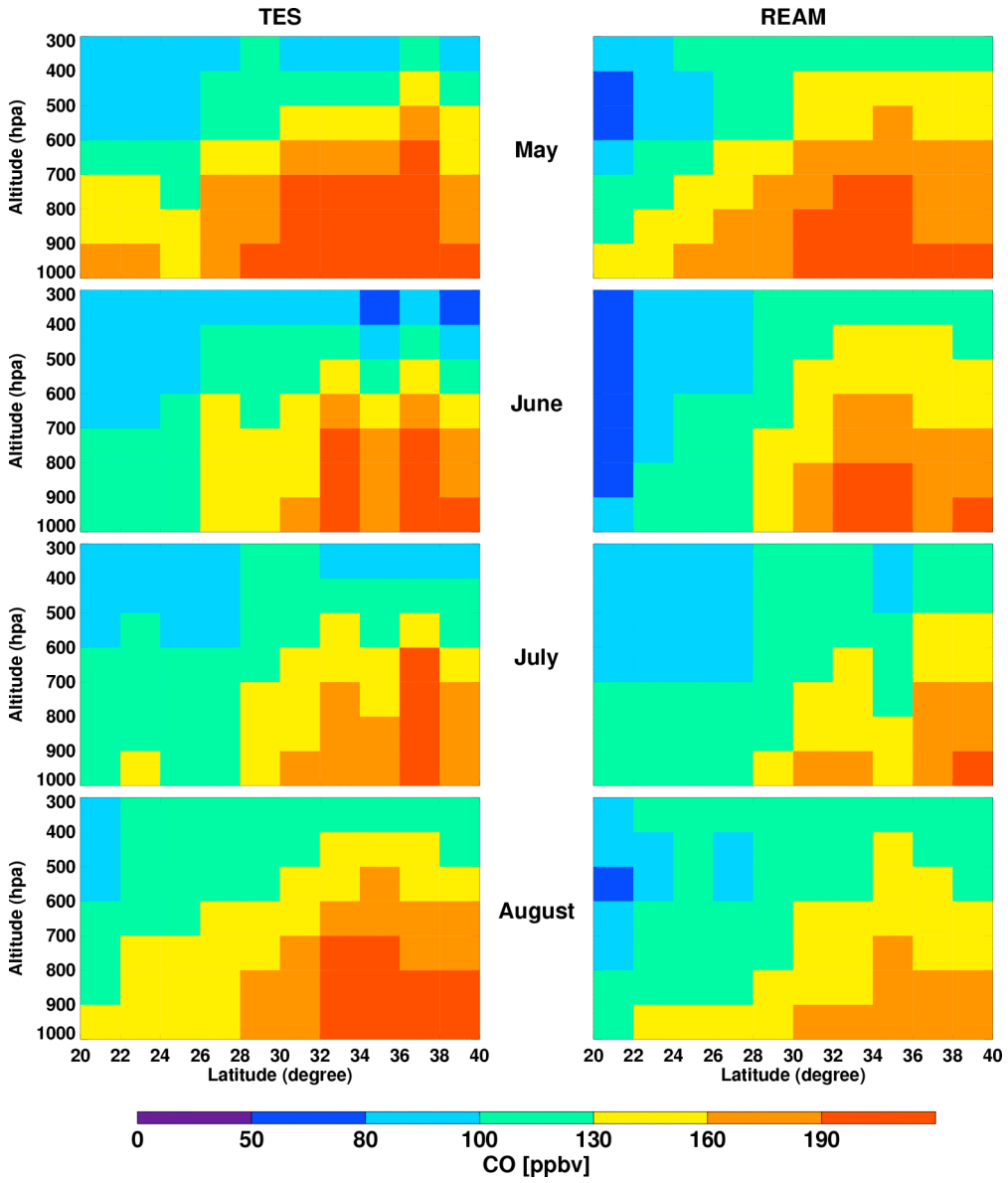

Figure 5.4 Latitude-altitude cross section of TES retrieved and REAM simulated monthly mean CO concentration distributions from May to August in 2006 over East China (110°-120° E) at 20°-40° latitude from surface to 300 hPa. The model results have been processed with the TES CO averaging kernel.

5.4.3 Impact of East Asian summer monsoon on tropospheric O_3 over East China

East Asian summer monsoon affect the O_3 concentrations over East China through bringing into the clean oceanic air and constraining the photochemical production of O_3 in the boundary layer. Figure 5.5 shows the REAM simulated time-latitude cross-section of 5-day average daytime O_3 production rate in the boundary layer over East China (110-120^o E) from May to August in 2006. Over the southeastern China, the boundary layer photochemical O_3 production is significantly constrained by the monsoon driven precipitation from May to mid June. However, during the same period over the east-central and northeastern China, the boundary layer photochemical O_3 production is fast, fostering a large amount of O_3 pollutant over the regions. The boundary layer O_3 production over the east-central and northeastern China becomes weaker in July and early August due to the northward advance of the monsoon driven rainfall. The large amount boundary layer O_3 production revives over East China since mid August after the monsoon driven rainy season disappearing.

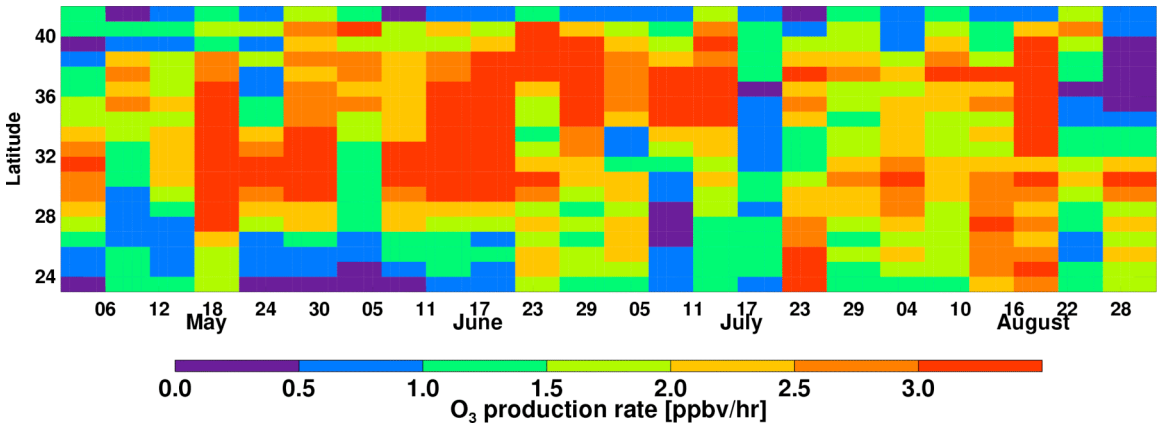

Figure 5.5 Time-latitude cross section of REAM simulated 5-day average of daytime O_3 production rate in the boundary layer over East China (110^o-120^o E) from May to August in 2006.

The constraint of the boundary layer O_3 concentrations by the monsoon onset is shown in TES 825hPa O_3 measurements. Figure 5.6 shows the time series of the 10-day average O_3 concentrations over Southeast and Northeast China at 825 hPa from TES and the corresponding REAM simulations. Only the averages with at least 3 available measurements are shown. Over Southeast China, the TES observed O_3 concentration reaches up to 60 ppbv in late May, rapidly drops to 40 ppbv in June and July due to the monsoon onset, and restores to 50 ppbv in August. The high O_3 concentration in late May results from the recirculation of the large amount of O_3 fostered over the east-central and northeastern China (Fig. 5.5) [Zhao et al., 2009a]. The monsoon impact on the boundary layer O_3 over Southeast China is evident. Over Northeast China, even though the average O_3 concentration is lower in July than June and August, the summer monsoon impact is not as evident as that over Southeast China. The standard deviation of the TES measured O_3 is up to 20 ppbv, but most is attributed to the uneven spatial distribution of the boundary layer O_3. REAM generally captures the feature of the measurements, and the biases are within the standard deviations of the measurements.

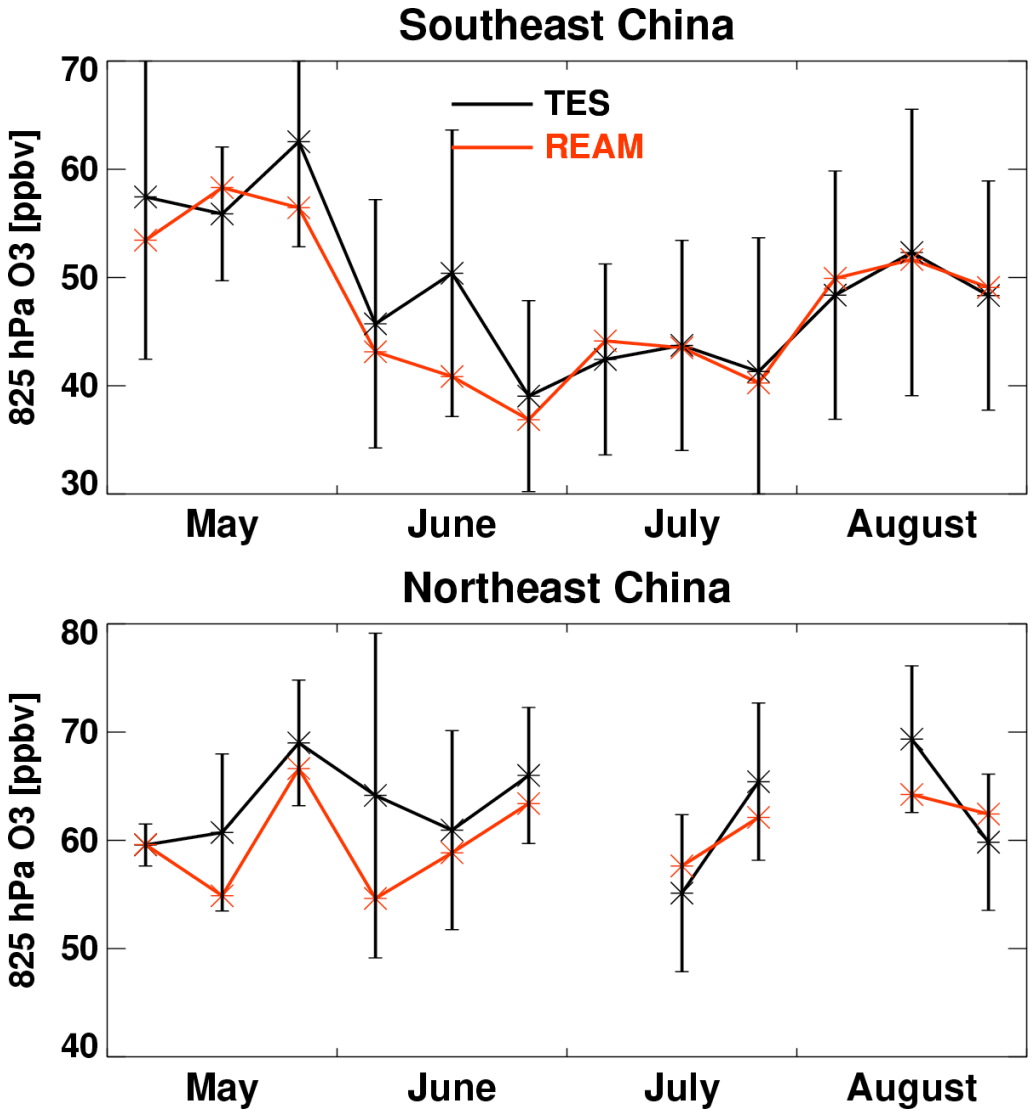

Figure 5.6 Time series of the 10-day average O_3 concentrations over Southeast and Northeast China at 825 hPa from TES and the corresponding REAM simulations. Star symbols show the observed and simulated means. The vertical bars show the standard deviations of the observations. The model results have been processed with the TES O_3 averaging kernel.

Figure 5.7a and 5.7b show the half-monthly mean tropospheric O_3 columns derived from OMI-MLS measurements and the corresponding model simulations from May to August in 2006. The OMI-MLS O_3 columns indicate high tropospheric O_3 columns over the entire of East China from May to mid June. The tropospheric O_3 enhancement is constrained over Southeast China since mid June and extending to Northeast China in July. The tropospheric O_3 enhancement over East China re-emerges since mid August. REAM captures the general patterns of observed tropospheric O_3 distributions over East Asia and the monsoon driven variation of the patterns. The correlation coefficient between the model simulations and the measurements is 0.7-0.9 and the difference is within ~10%. The model simulates lower tropospheric O_3 columns because REAM-simulated upper tropospheric O_3 concentrations tend to be low, which is propagated from GEOS-CHEM through the specified upper boundary condition [Choi et al., 2008a,b]. The bias in the upper boundary condition likely leads to some underestimates of the stratospheric contribution to the tropospheric O_3 columns.

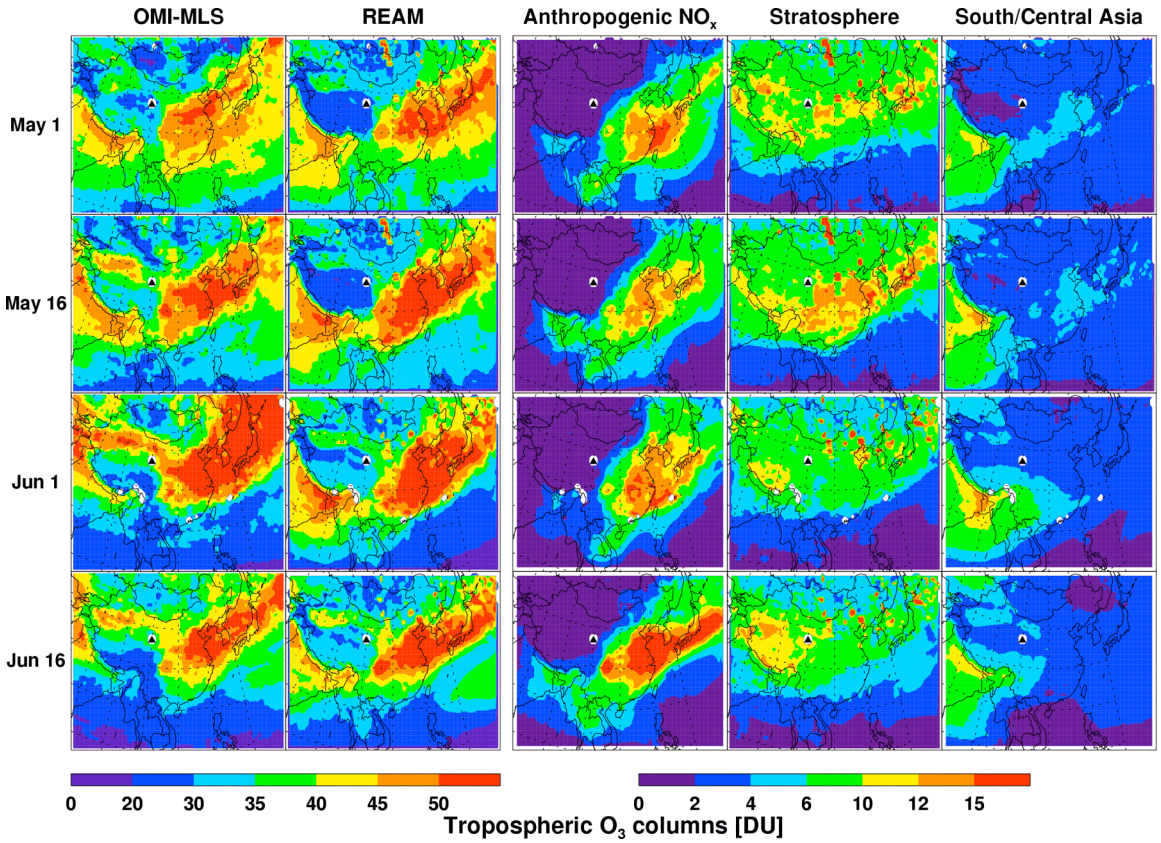

Figure 5.7a Half-monthly mean tropospheric O_3 columns from May to June in 2006 derived from OMI-MLS satellite measurements (first column), REAM simulations (second column), production due to anthropogenic NO_x emissions over East Asia (third column), transported from the stratosphere (last column), and transported from South/Central Asia. The black triangle represents for the WLG station.

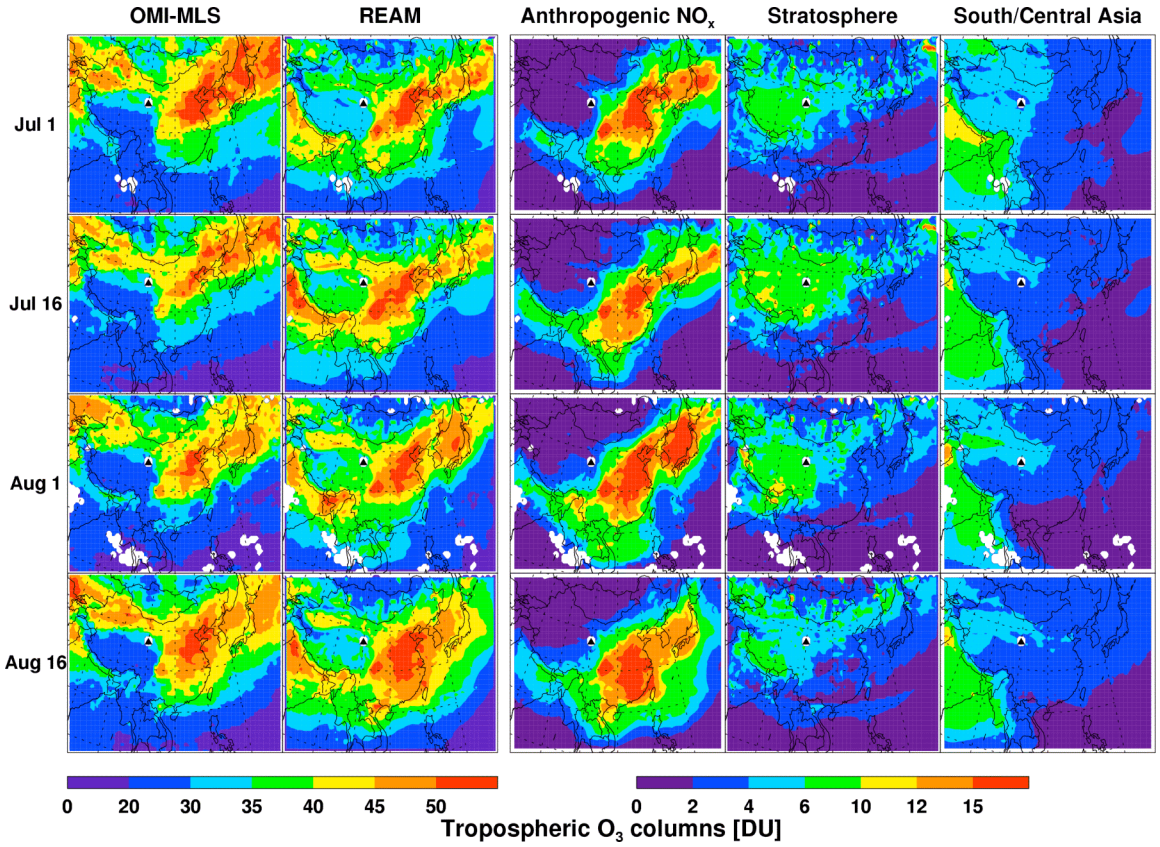

Figure 5.7b Same as Figure 5.7a but for July and August in 2006.

Three sensitivity simulations are conducted to explain the observed and simulated tropospheric O_3 distributions. One is the simulation without anthropogenic NO_x emissions over East Asia, which turns off most of the photochemical production of tropospheric O_3 over East Asia. The second one is the simulation without the stratospheric contributions. To calculate the effect of the stratospheric O_3, we did in the same way as Choi et al. [2008b], in which we run tagged tracer simulations using GEOS-CHEM to compute the fractions of O_3 transported from the stratosphere. We remove the stratospheric contributions in the REAM sensitivity simulation by using only the tropospheric portions of initial conditions and lateral and upper boundary conditions for O_3. The third one is the simulation without the transport of the O_3 from South/Central Asia, in which the anthropogenic NO_x emissions over South/Central Asia in the REAM and GEOS-CHEM simulations are turned off. We estimate the anthropogenic NO_x and stratospheric contributions and O_3 transported from South/Central Asia by subtracting O_3 in the sensitivity simulations from the standard one and the results are shown in Figure 5.7a and 5.7b (the rightmost three columns).

The photochemical produced tropospheric O_3 columns over East China, in particular Northeast China, generally increase from May to August (Fig. 5.7a and b, the third column). The constraint of the boundary layer photochemical O_3 production by the monsoon onset over East China is not apparent in term of the tropospheric columns because the constrained photochemical O_3 production in the boundary layer is overwhelmed by the enhancive O_3 production in the free troposphere, where the impact of precipitation and cloud is limited, driven primarily by increasing solar insolation and water vapor from spring to summer. However, the produced O_3 cannot accumulate in

summer, in particular from mid June to early August, because of the export by the strong monsoon driven southerly flow. The contribution from stratospheric intrusion to tropospheric O_3 columns over East China is largest and comparable to the photochemical production in May, and decreases to the smallest in August. Transport of O_3 from the stratosphere decreases from May to August as wave propagation from the troposphere to stratosphere weakens in summer [e.g., Y. Wang et al., 1998 and references therein]. The impact of the O_3 transported from South/Central Asia is much smaller than the other two contributors in May and June, but comparable, if not larger, versus stratospheric intrusion in July and August. The South/Central Asia O_3 is mostly transported through Southwest China in May and June, but through Northwest China in July and August, because the transport is largely driven by India summer monsoon, which starts in May and June over South India, but moves to North India and Central Asia in July and August.

The tropospheric O_3 columns enhancement over the entire of East China from May to mid June is attributed to the combination of the regional fast photochemical O_3 production and stratospheric O_3 intrusion. In July, the tropospheric O_3 columns drop down to the minimum over East China due to the monsoonal inflow and the constrained photochemical processing in the boundary layer. The O_3 enhancement re-emerges since mid-August due to the revived fast boundary layer photochemical production of O_3 along with the retreat of the monsoon. The monsoon impact on tropospheric O_3 is more significant over Southeast China than over Northeast China.

5.4.4 Summer tropospheric O_3 enhancement over West China

Previously, Zhu et al. [2004] and T. Wang et al. [2006] found the high O_3 over West China in late spring and summer based on the surface measurements at the WLG

station over West China [e.g., Zhu et al, 2004; T. Wang et al. 2006]. A band of tropospheric O_3 enhancement over West China (36-42^{o}N, 80-100^{o}E) is also observed by the OMI-MLS O_3 columns from May to August in 2006 (Fig. 5.7a,b). The band of high tropospheric O_3 columns is mostly at the north of 35^{o}N because of the Himalayas and the Tibetan plateau south of 35^{o}N. The REAM model generally captures the band of high tropospheric O_3 columns over West China but underestimates the enhancement.

Figure 5.8 shows the time series of the REAM simulated tropospheric O_3 columns and surface O_3 concentrations due to the transport of the O_3 from East Asia, South/Central Asia, and stratosphere at the WLG station and over West China from May to August in 2006. In term of tropospheric columns, the O_3 transported from stratosphere is the dominant source both at the WLG station and over West China. The O_3 transported from East Asia is lower than that from South/Central Asia over West China, but comparable at the WLG station because the WLG station is closer to the polluted regions of East China. The O_3 transported from South/Central Asia increases from May to August due to the north migration of the India summer monsoon. While the REAM simulated lower tropospheric O_3 columns over West China may result from the underestimate of the stratospheric contribution to the tropospheric O_3 columns, it may also results from the underestimate of the O_3 transported from South/Central Asia particularly in July and August. In term of surface O_3 concentrations, the three contributors are comparable at the WLG station and over West China. The peaks of the surface O_3 concentrations at the WLG station reflect the pollution events in polluted regions nearby.

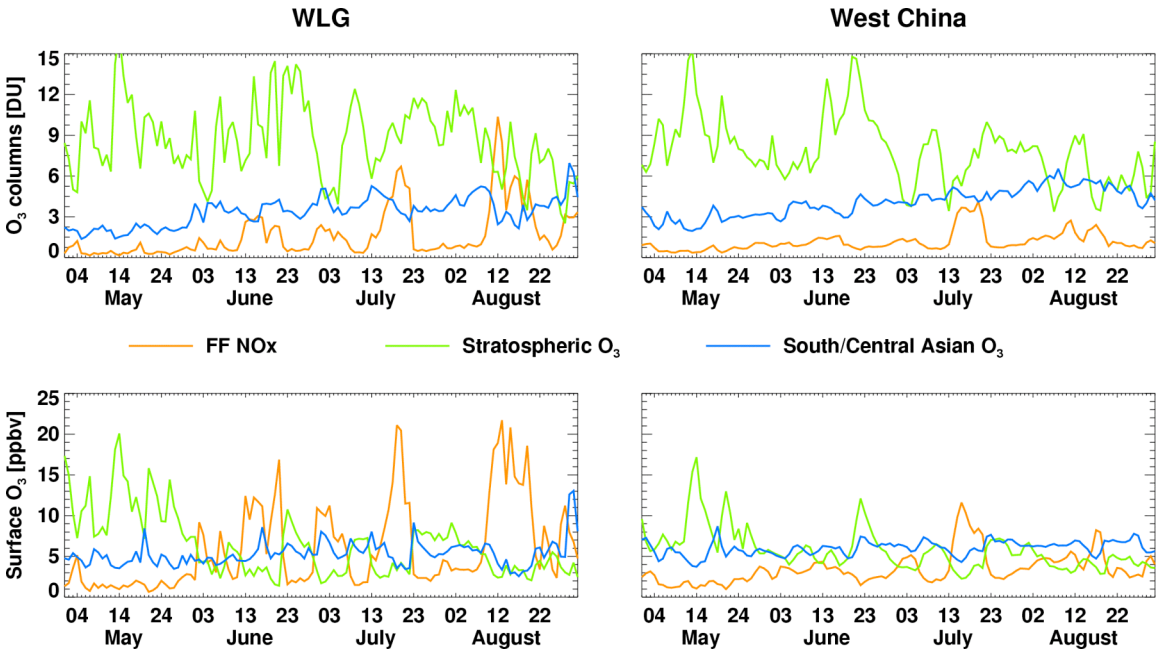

Figure 5.8 Time series of REAM simulated contributions from anthropogenic NO_x emissions over East Asia, stratosphere intrusion, and transport from South/Central Asia to daytime tropospheric O_3 columns and surface O_3 for May-August 2006 at the WLG station and over West China (36-42°N, 80-100°E).

5.5 Conclusions

Tropospheric O_3 columns retrieved from OMI and MLS measurements, CO columns from MOPITT, and lower tropospheric O_3 and CO concentrations from TES from May to August in 2006 are analyzed using the Regional chEmical and trAnsport Model (REAM) to investigate the impact of the East Asian summer monsoon on the air quality over China. The large perturbation of the air pollutant distributions over China by the onset of East Asian summer monsoon is observed by the satellite measurements and simulated by the REAM model. In monsoon-affected areas, ventilation by convection is faster and boundary layer photochemical processing is slower. Both MOPITT and TES measurements and REAM simulations show that CO enhancements over East China disappear with the onset of the monsoon and re-emerge afterwards. The monsoon impact is more significant on the CO concentrations in the boundary layer than in the free troposphere.

Both the TES 825 hPa O_3 concentrations and OMI-MLS tropospheric O_3 columns show a monsoon driven bimodal distribution of tropospheric O_3 concentrations: high O_3 in the pre-monsoon period, rapid decrease of O_3 during monsoon, and O_3 recovery after monsoon. The analysis of the corresponding REAM model simulations shows that the pre-monsoon tropospheric O_3 enhancement over East China is attributed to the combination of regional fast photochemical O_3 production and stratospheric intrusion. The monsoon season tropospheric O_3 minimum over East China results from the incursion of monsoonal inflow, which transports marine air masses with low O_3 concentrations. The moist air mass leads to convective ventilation and formation of clouds, which slows down boundary layer photochemical processing. The O_3

enhancement re-emerges after mid-August when monsoon ends. While the observed and simulated summer column enhancement of tropospheric O_3 over West China is dominated by the stratospheric O_3 intrusion, surface O_3 over West China is attributed to O_3 transported from polluted East Asia and South/Central Asia, and the stratosphere.

CHAPTER 6

CONCLUSION AND FUTURE RESEARCH

6.1 Summary of Main Findings

A Regional chEmical trAnsport Model (REAM) was developed and used to study the distribution of air pollutants in the troposphere on a regional scale using diverse satellite measurements as well as in-situ surface and aircraft measurements. REAM was applied for North America and East Asia, two of the most polluted regions in the world. REAM was used to assess the uncertainties in modeling the impact of convection and lighting processes on the production and distribution of tropospheric chemical tracers over North America and to investigate the meteorological and anthropogenic impact on the distribution of air pollutants over East Asia, in particular China.

6.1.1 Uncertainties in modeling the impact of convection transport and lightning NO_x production on tropospheric chemical tracers over North America

To assess the model uncertainties in parameterizations of convection transport and lightning NO_x production, two different cumulus convective parameterizations, KF-eta and Grell, were incorporated into REAM from the meteorological models, WRF and MM5, respectively. The entrainment and detrainment are found to significantly affect the US air pollutant outflows over West Atlantic Ocean in the free troposphere; KF-eta with entrainment and detrainment results in more outflow at 3-9 km than the Grell scheme. Using the C_2H_6/C_3H_8 ratio as the chemical indicator affected by this outflow, we found that WRF-REAM with KF-eta scheme shows larger decreases (up to a factor of 2) of

C_2H_6/C_3H_8 ratio at 3-9 km due to convective outflow, and hence it is in closer agreement with the INTEX-NA observations than MM5-REAM with Grell scheme. Larger mass fluxes, as well as entrainment and detrainment in the KF-eta scheme in WRF-REAM, also lead to more scavenging of soluble HNO_3 in the free troposphere than MM5-REAM. The simulated median profile of HNO_3 by WRF-REAM is in closer agreement with the measurements than that of MM5-REAM, although the observed variation is larger than the model difference.

WRF with KF-eta simulates lower convective cloud top height than MM5 with Grell scheme, partly resulting from the inclusion of entrainment and detrainment in the KF-eta scheme. Consequently, WRF-REAM simulates less lightning NO_x than MM5-REAM and the maximum lightning NO_x altitude of 12 km in WRF-REAM is lower than 15 km in MM5-REAM. Measurements of tropospheric NO_2 columns from SCIAMACHY provide a qualitative comparison, which suggests that WRF-REAM results are closer to the observations. Evaluation using the ISCCP cloud top height measurements from GOES satellites clearly demonstrated that MM5 simulated convective cloud tops are too high over the southeastern US and western North Atlantic.

It's interesting to note that the large model difference in lightning NO_x occurs mostly above 12 km, where no in-situ measurements were available from INTEX-NA. The two models show similar agreement with upper tropospheric in-situ NO_2 and O_3 measurements. Over the observation regions of INTEX-NA, the two models show similar results for the effects of lightning NO_x in the upper troposphere: (1) lightning enhances upper tropospheric NO_2 concentrations by a factor of >5 (~100 ppt) and NO_2 columns by a factor of >1.5 over the ocean; (2) lightning and surface emissions contribute ~70%

(40%) and ~10% (10%), respectively, to the upper tropospheric NO_x (NOy); and (3) lightning NO_x increases upper tropospheric O_3 concentrations by up to 20 ppbv with an average of 10 ppbv.

6.1.2 Air quality studies over East Asia

East Asia, in particular China, contributes significantly to the global NO_x budget. China NO_x emission inventories, based on the bottom-up approach, are thought to be quite uncertain. A new daily assimilated inversion method was developed using the REAM model to constrain the surface NO_x emissions over East Asia based on OMI NO_2 measurements. The iterative nature of the assimilated inversion accounts for the chemical feedbacks of NO_x emission changes and reduces the dependence of the a posteriori emissions on the a priori emissions, resulting in significant improvements over the previous monthly-mean inversion result. The daily assimilated inversion increases the spatial covariance (R^2) and decreases the RMSE between observed and simulated NO_2 columns compared with the widely-used monthly-mean inversion results. The assimilated a posteriori NO_x emissions from fossil fuel combustion over East Asia are 9.5 Tg N/yr, 13% lower than the a priori value of 10.9 Tg N/yr. While the total emission change is small (less than the 17% uncertainty in the assimilated a posteriori inventory), significant spatial distribution changes were found, especially over East China. The a priori fossil fuel NO_x emission inventory tends to overestimate the emissions over the economically developed areas and underestimate over the underdeveloped areas in East China. While the dichotomy of a prior inventory bias may indicate an issue with the bottom-up statistics used to derive the inventory, it may also reflect in part fossil fuel NO_x emission

reductions resulting from the urban-centric air quality controls and enforcements in China.

The estimated East Asia NO_x emission inventory shows that the anthropogenic NO_x emission in China is 35% higher than in the US and that they are concentrated over three connected plains in the east. The analysis of an episode of highly elevated ozone over East China indicate that the geographically flat East China plains coupled with high anthropogenic NO_x emissions lead to a large amount of O_3 pollutant. During the episode, the East China plains were under a high pressure system, which suppressed the ventilation of pollutants from the boundary layer. Simulated ozone concentrations over a major fraction of East China reached high levels, all the way down to the Pearl River Delta region on the southern border. The convergence of high pollutant emissions and large population over the vast stretch of the geographically flat plains of East China makes the region susceptible to high-ozone exposure. The high-O_3 concentrations during the episode extended over an area > 1 million km^2, which hosts a population of > 800 million people. Model sensitivity simulations indicate that ozone concentrations are very responsive to NO_x emission reductions in terms of high ozone areas and hence population exposure.

The convergence of pollutants (e.g., O_3) over the East China plains occurs mostly in the late spring and early summer before the onset of the East Asian summer monsoon. During the summer monsoon season, the pollutant levels are limited. Tropospheric O_3 columns retrieved from OMI and MLS measurements, CO columns from MOPITT, and tropospheric O_3 and CO concentrations from TES were analyzed using the REAM model to investigate the impacts of the East Asian summer monsoon on the air quality over

China. The strong constraint of the air pollutant levels over China by the East Asian monsoon onset was observed by satellite measurements and simulated by the REAM model. Pollutant levels are limited as a result of the faster convective ventilation and scavenging but restrained boundary layer photochemical processing during the monsoon season.

All the satellite measurements and REAM simulations show the regions with enhancements of CO and O_3 over East China disappear with the onset of the monsoon, but re-emerge afterwards. The monsoon impact is more significant on the CO concentrations in the boundary layer than in the free troposphere. The OMI-MLS tropospheric O_3 columns show the pre-monsoon O_3 enhancements and monsoon season O_3 decreases over East China. The analysis of the corresponding REAM model simulations shows that the pre-monsoon tropospehric O_3 enhancement over East China is attributed to the stratospheric intrusion and regional photochemical production; whereas the monsoon season tropospheric O_3 decrease results from the incursion of monsoon inflow. The moist air mass leads to convective ventilation and formation of clouds, which slows down boundary layer photochemical processing. The O_3 enhancement re-emerges since mid-August when monsoon ends. While the observed and simulated summer column enhancement of tropospheric O_3 over West China is dominated by the stratospheric O_3 intrusion, surface O_3 over West China is attributed to O_3 transported from polluted East Asia and South/Central Asia, and the stratosphere.

6.2 Recommendations for Future Research

6.2.1 Lightning NO_x production

The lightning effect deserves further study because of its significant impact on the distribution of tropospheric chemical tracers. Lightning NO_x is a big source of the upper tropopheric O_3, which is more sensitive to the radiative forcing change. Also, the reduced anthropogenic emissions over the US will make the lightning NO_x become a more dominant source of NO_x in the free troposphere over the US. Therefore, improving the accuracy of the lightning parameterization is very important. Lightning-flash frequency can be further constrained with the combination of the surface in-situ and satellite observations. The change in lightning NO_x production driven by the changing climate is also very interesting and deserves additional study.

6.2.2 NO_x inversion from satellite measurements

The assimilated inversion method introduced in Chapter 3 can be applied to estimate the NO_x emissions for a long term and over different regions using satellite measurements. With the advantage of the assimilated inversion that considers the chemical feedbacks and is a priori independent, the derived NO_x emissions can be used to analyze the annual increasing rate of the NO_x emissions over China. The assimilated inversion can be also applied over the US to constrain the bottom-up estimated NO_x emission.

6.2.3 Long-term variation of the East Asian summer monsoon and its implication for regional climate change

The factors that influence the East Asian summer monsoonal flow and precipitation are of central importance for understanding climate change in the region. It is commonly believed that greenhouse-gas-induced global warming can weaken the winter East Asia monsoon but strengthen the East Asia summer monsoon, as stronger

warming occurs over high-latitude continent as opposed to the low-latitude oceans. However, the measurements show that the results are not as straightforward as this because of atmospheric aerosol loading. These changes may also feedback to enhance the impact of human activity in these regions, as a less windy climate has also consequences for air quality. Investigation of the change in the East Asian summer monsoon onset and its impact on the air quality can help to further understand the complicated interaction between regional climate change and air quality.

APPEDIX A

AUXILIARY MATERIALS FOR CHAPTER 2

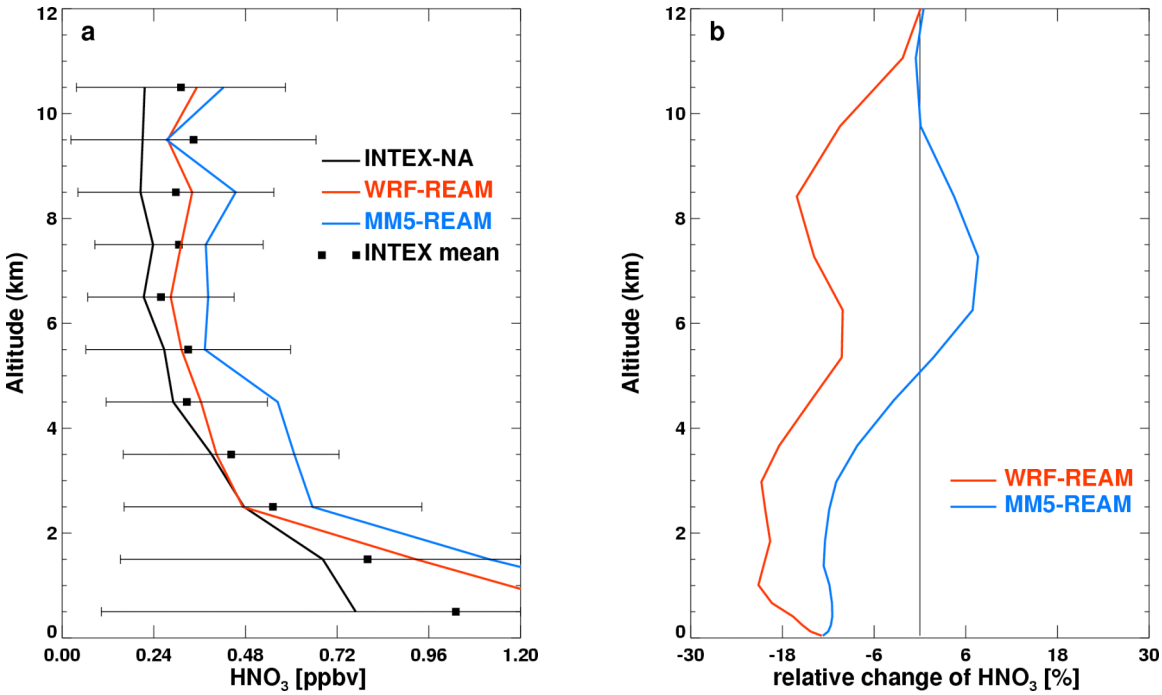

Figure A.1 Vertical profiles of HNO_3 from aircraft measurements and REAM standard simulations, and the mean convection driven relative changes of the concentrations of HNO_3 from REAM simulations during summer (July and August) 2004.

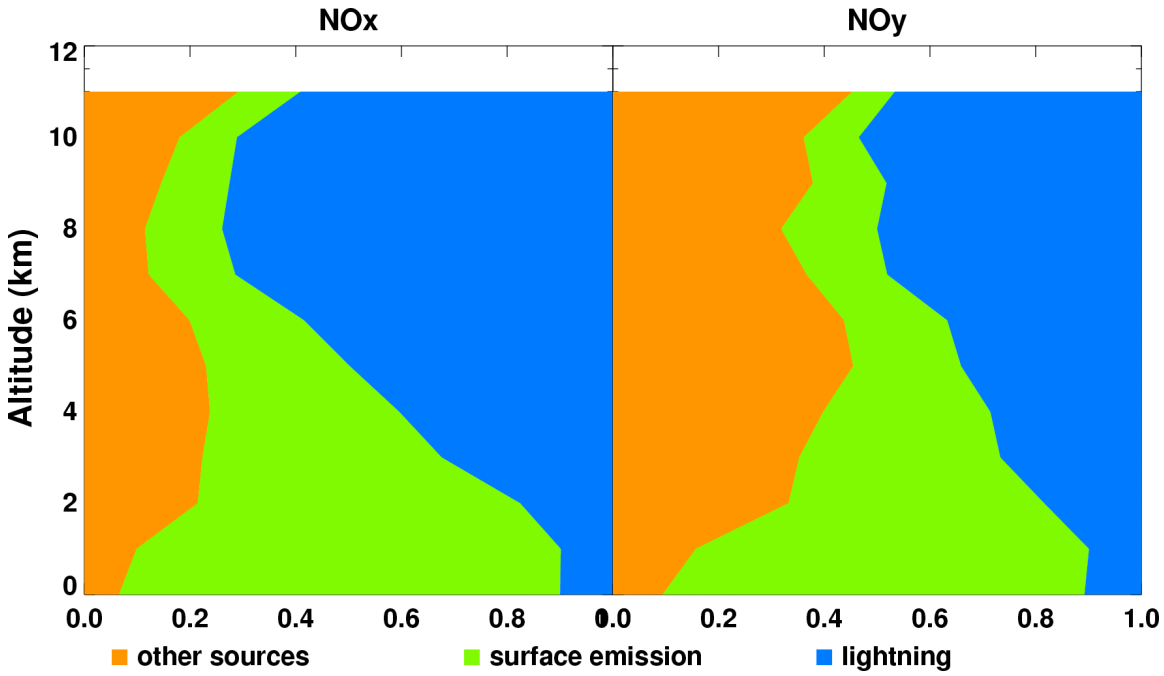

Figure A.2 The relative contributions of surface emissions (anthropogenic and soil NO_x), lightning, and other sources (e.g., transport from boundary, aircraft emission, and stratosphere downward inflow) to NO_x ($NO+NO_2$) and NO_y (NO_x+HNO_3+PAN) from WRF-REAM simulations during INTEX-NA. MM5-REAM has the similar results.

APPEDIX B

AUXILIARY MATERIALS FOR CHAPTER 3

B.1 Assessment of model errors in simulating tropospheric NO_2 columns

We estimate model errors by comparing the simulated tropospheric NO_2 columns with different meteorological fields assimilated by MM5 and WRF, respectively. The same a priori NO_x emissions are used. Figure B.1 shows the monthly mean absolute relative model errors over East Asia. The errors are < 30% over most regions of East Asia with an average of 11%. The errors are within the range of 5-15% over most regions over East China, where the significant changes in the spatial distribution of the a posteriori from priori NO_x emissions are found.

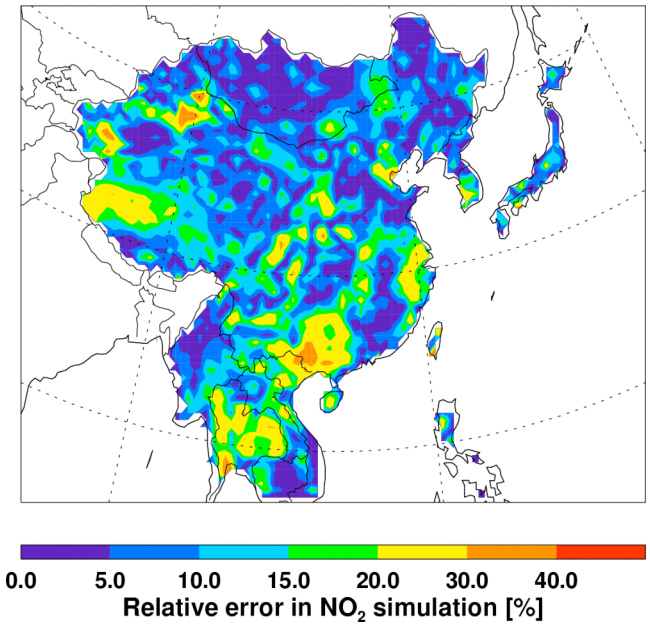

Figure B.1 Monthly-mean absolute relative model errors of tropospheric NO_2 columns between MM5 and WRF driven REAM over East Asia for July 2008.

B.2 Description of the daily assimilated inversion method

In the daily assimilated inversion, we adopt the framework by Martin et al. [2003] on a daily basis following these steps. (1) Invert the satellite observations of tropospheric NO_2 columns with a 3-D CTM model simulation to obtain the top-down estimates. (2) Compute the a posteriori results by combine the resulting top-down NO_x emission estimates with a priori estimates from a bottom-up inventory, weighted by the relative errors in the two estimates. Assuming a lognormal distribution of errors on E_a (a priori NO_x emission) and E_t (top-down NO_x emission), the a posteriori results are obtained:

$$\ln E = \frac{(\ln E_t)(\ln \varepsilon_a)^2 + (\ln E_a)(\ln \varepsilon_t)^2}{(\ln \varepsilon_a)^2 + (\ln \varepsilon_t)^2} \tag{1}$$

and

$$(\ln \varepsilon)^{-2} = (\ln \varepsilon_a)^{-2} + (\ln \varepsilon_t)^{-2} \tag{2}$$

where E is the a posteriori NO_x emission, ε is the relative error of E, ε_a is the relative error of E_a, and ε_t is the relative error of E_t computed from retrieval and model representation errors [Martin et al., 2003]. (3) Apply the a posteiori emissions in the regional CTM after the inversion to compute column NO_2. (4) At the time of OMI measurements in the next day, use the a posteriori emissions and errors computed from the previous as the priori values and repeat the process. (5) Repeat the process till the end of the month. Compute the average of the a posteriori emissions (and their errors) of the last week as the a posteriori result of the assimilated inversion.

B.3 Convergence of the daily assimilated a posteriori emissions

Figure B.2 shows the time series of daily a posteriori emissions over East China in July 2007. We show the total a posteriori emission of the whole region, as well as the totals over the regions with either overestimation or underestimation over East China. The monthly mean inversion results are constant since it is a single inversion. The initial values of the daily inversion results are the a priori emission values. As we discussed in the paper, the total emission over East China does not change significantly after the inversion. As a result, we do not find large changes in its time series. For regions with either overestimates or underestimates, the emission correction in the monthly inversion is not as much as the assimilated daily inversion. The emission decreases (increases) from 6.0 (3.0) Tg N/yr to 3.4 (5.4) Tg N/yr in the assimilated inversion compared to 4.8 (4.0) Tg N/yr in the monthly inversion. The convergence time scale is ~10 days.

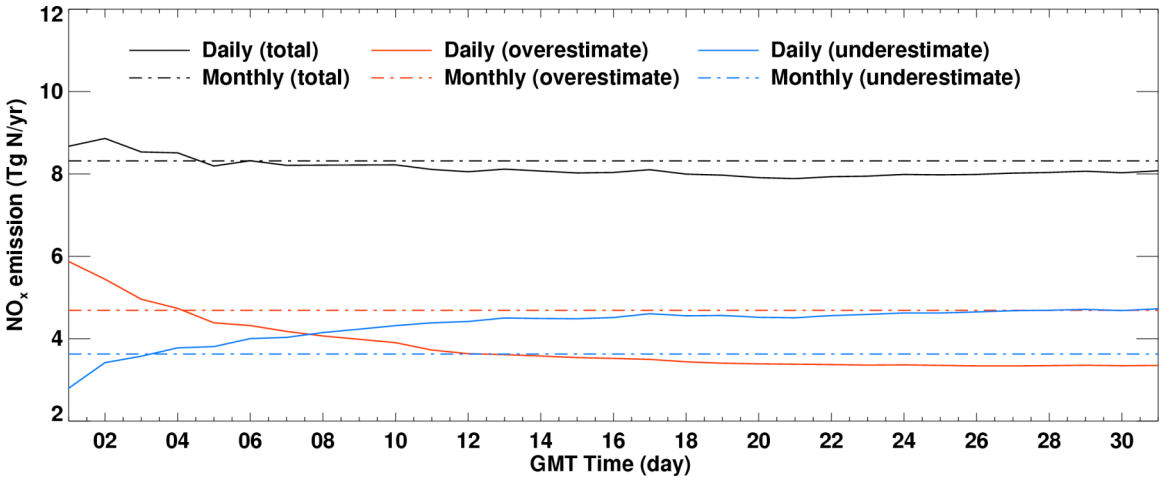

Figure B.2 Time series of the a posterior total NO_x emissions over the whole East China (black), and overestimated (red) and underestimated (green) regions of East China. Results are shown for the monthly (dash line) and daily assimilated (solid line) a posteriori emissions.

B.4 Apportionment of surface NO_x emissions

The least-squares regression is applied to linearly partition the a posteriori emissions based on the a priori fossil fuel and soil emissions, i.e., $E_{posteriori} = aE_{priori}^{fuel} + bE_{priori}^{soils}$. The regression is applied to the monthly mean result over the grids where the ratio of a priori fossil fuel/ a posteriori total emission is < 0.9. We obtain a posteriori monthly mean soil emissions by scaling the a priori emissions by the factor of *b* over the entire domain. The rest of the emissions are assigned as a posteriori fossil fuel emissions. In sensitivity tests, the threshold ratio of a priori fossil fuel/ a posteriori total emission (for the least-squares regression) is changed from 0.9 to 0.5 and 0.3. A lower emission ratio implies a larger contribution from soil emissions. The resulting factor of *b* does not change significantly with a range of 2.4-2.7. In the manner, we obtain the a posteriori soil NO_x emissions of 1.6 TgN/yr for July, a factor of 2.4 higher than the a priori value of 0.68 TgN/yr. It accounts for ~14% of the total a posteriori emissions. Subtracting the soil emissions, we obtain the a posteriori fossil fuel emissions, the total of which is estimated as 9.5 TgN/yr over East Asia, 13% less than the a priori value of 10.9 TgN/yr.

Y.X. Wang et al. [2007] also found a need to increase soil emissions based on GOME NO_2 measurements. The magnitude of increase is larger in that study; they found that 43% of total surface emissions in summer are from soils. Two factors may have contributed to the difference between these two studies. First, the period of the previous study is 1997-2000. Fossil fuel NO_x emissions have probably doubled in China from 1998 to 2007 [e.g., Zhang et al., 2007; Stavrakou et al., 2008]. Second, in the Y.X. Wang et al. study, they found a large underestimate in the a priori emissions. Using more recent

emission inventories and accounting for the annual fossil fuel emission increase, the total a posteriori emissions do not differ significantly from the a priori inventory in our study. It is therefore unnecessary to attribute a large fraction of surface emissions to soils in summer 2007. Our result corroborates the finding by Stavrakou et al. [2008], who used GOME measured NO_2 columns as by Y.X. Wang et al [2007].

B.5 NASA Versus KNMI in tropospheric NO_2 retrieval

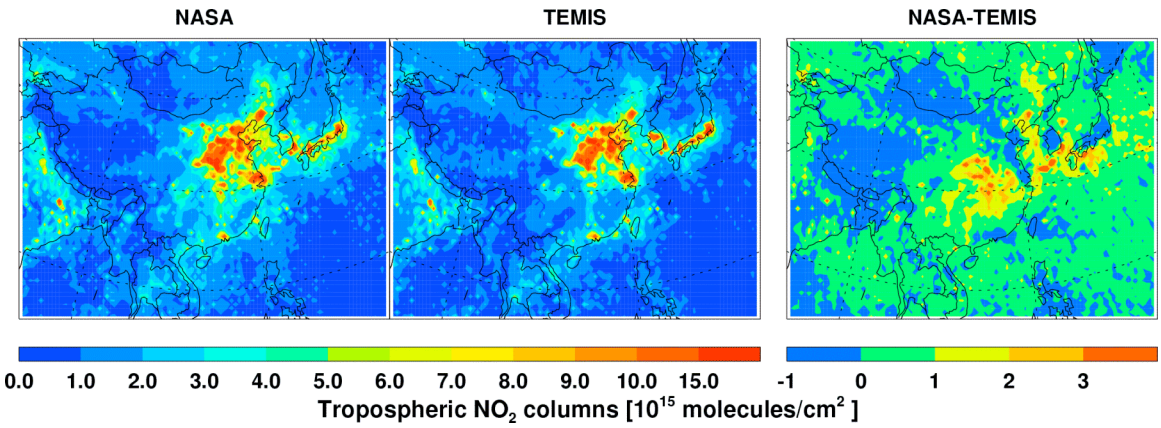

Figure B.3 Monthly mean tropospheric NO_2 columns over East Asia for summer (June, July, and August) in 2007 retrieved by NASA and KNMI (TEMIS) from OMI measurements. Only OMI data with cloud fractions of < 30% are used. The difference between the two retrievals is shown in the third column.

B.6 Annual and monthly variation of OMI NO2

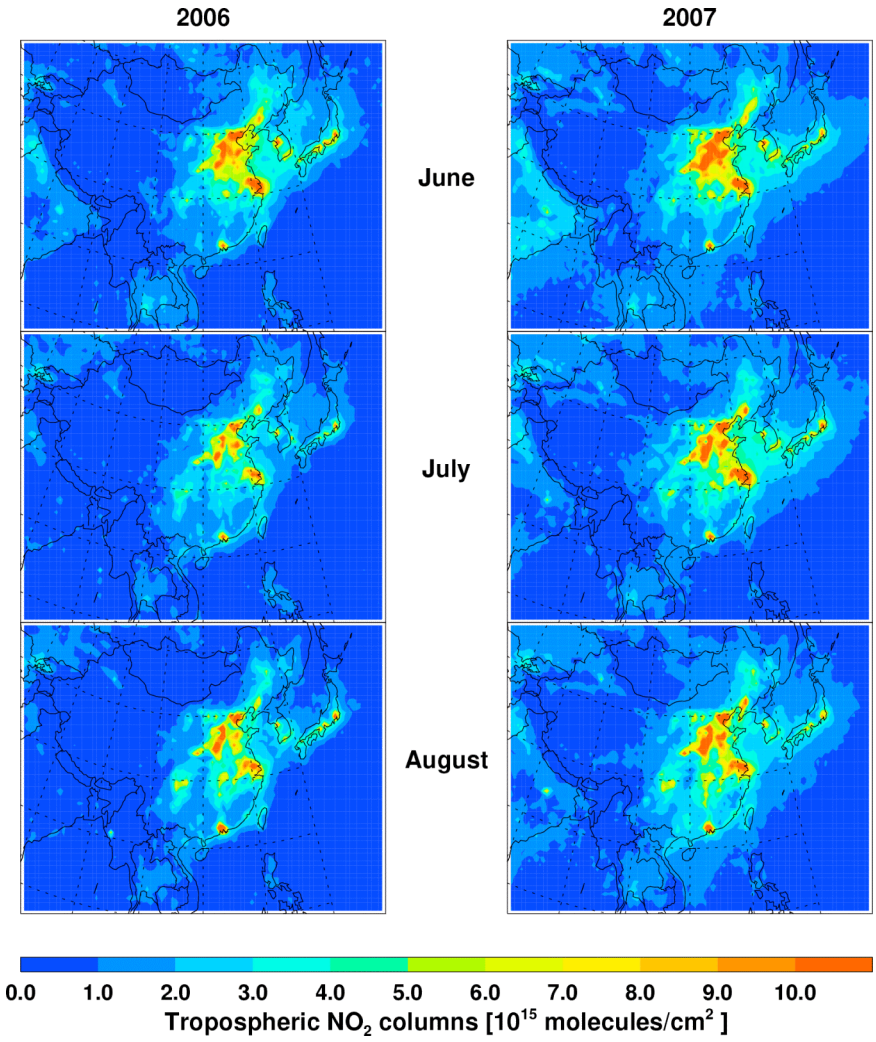

Figure B.4 Monthly mean tropospheric NO_2 columns over East Asia for summer (June, July, and August) in 2006 and 2007 retrieved by NASA from OMI measurements. Only OMI data with cloud fractions of < 30% are used.

APPENDIX C

AUXILIARY MATERIALS FOR CHAPTER 4

C.1 REAM model description

In this work, the REAM model has a horizontal resolution of 70 km with 23 vertical layers reaching 10 hPa, 20 of which are below 100 hPa. The National Center of Atmospheric Research/Penn State MM5 is used to simulate meteorological fields using four-dimensional data assimilation (FDDA) [Stauffer et al., 1991]. The photochemistry module and the algorithms for dry and wet deposition and emissions from vegetation and soils are adopted from the GEOS-CHEM model [Bey et al., 2001]. The altitude-dependent cloud optical depth is calculated using MM5 liquid water content [Stephens et al., 1978]. The UV surface albedo distribution, for photolysis rate calculations, is obtained from TOMS observations [Herman et al., 1997]. The transport scheme is by Walcek et al. [2000]. The convection scheme by Grell [1993] is implemented to be consistent with the meteorological model. The lightning NO_x emission is parameterized by Choi et al. [2005]. Twenty-four chemical tracers describing tropospheric O_3 chemistry [Bey et al., 2001] were transported.

C.2 REAM model evaluations

C.2.1 Tropospheric NO_2 columns

The tropospheric NO_2 columns retrieved from the OMI instrument [Bucsela et al., 2006] onboard the NASA Aura satellite are used to confirm that the anthropogenic NO_x emissions in the model do not have significant biases. As the OMI tropospheric NO_2

columns are not available for June 2004, we evaluate the emissions for June 2005 (scaled from the emissions for June 2004 with 8% increasing rate). The retrieved tropospheric NO_2 columns and its uncertainties are obtained as in Chapter 3 from two independent products: near-real time (NRT) tropospheric NO_2 columns retrieved by KNMI/NASA [Boersma et al., 2007] and OMI standard product at NASA Goddard Earth Sciences Data and Information Services Center (GES-DISC) [Bucsela et al., 2006]. We obtain the "best-estimates" of tropospheric NO_2 columns by averaging the columns from KNMI and GES-DISC weighted by their uncertainties. We use two methods to estimate the errors in the combined OMI columns. The first method is to estimate the errors as the root mean square of the uncertainties of the two retrievals. The second method is to estimate the error as the deviations of KNMI and GES-DISC retrievals from their means. We take the larger of the two estimates as the uncertainty for the combined OMI columns, which is around 40% over the polluted regions and reaches a factor of 1.5 over the ocean and clean continent such as western China. Only the OMI tropospheric NO_2 column data with cloud fractions of < 30% are used in the study. The comparison is shown in Figure B.1. The model successfully reproduces the satellite measurements, and the mean bias and correlation coefficient between simulated and observed tropospheric NO_2 columns over China is 0.25×10^{15} molecules/cm^2 (~10%) and 0.89 respectively. The model bias is within the uncertainty of satellite measurements.

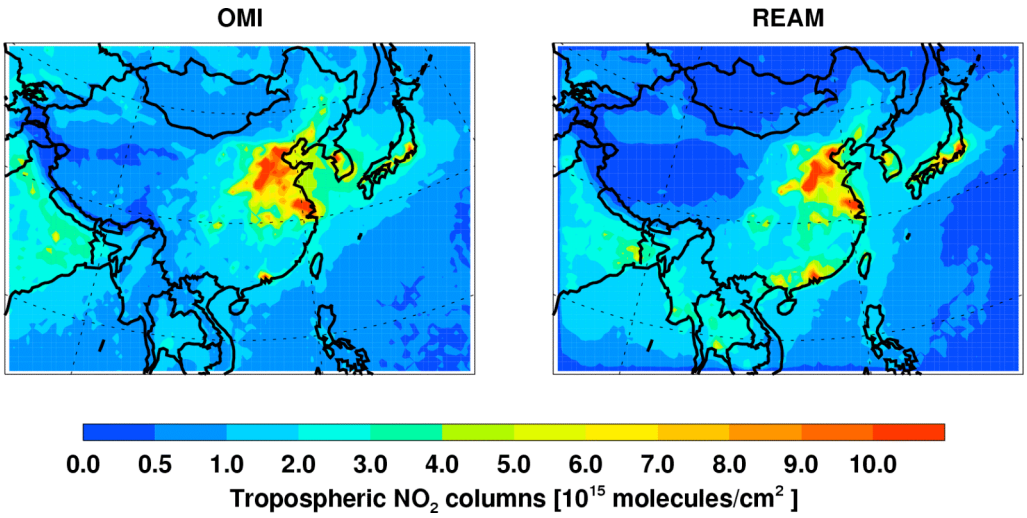

Figure C.1 Monthly mean tropospheric NO_2 columns over East Asia for June 2005 from OMI measurements (left), and the corresponding REAM results. Only OMI data with cloud fractions of < 30% are used.

C.2.2 Ozone

Hourly ozone observations at Mt. Tai and Huang in May 2004 are compared to the REAM simulation results (Fig. C.2). The data at Mt. Hua are not available for May 2004. The standard model generally captures the high ozone concentrations, and the correlation coefficients between the simulation and measurements are 0.49 and 0.53 for Mt. Tai and Huang respectively. The VOC simulation at Mt. Tai improves the comparison, and the correlation coefficient increases to 0.59. The VOC simulation does not significantly change the simulation at Mt. Huang, so only the standard simulation results are shown.

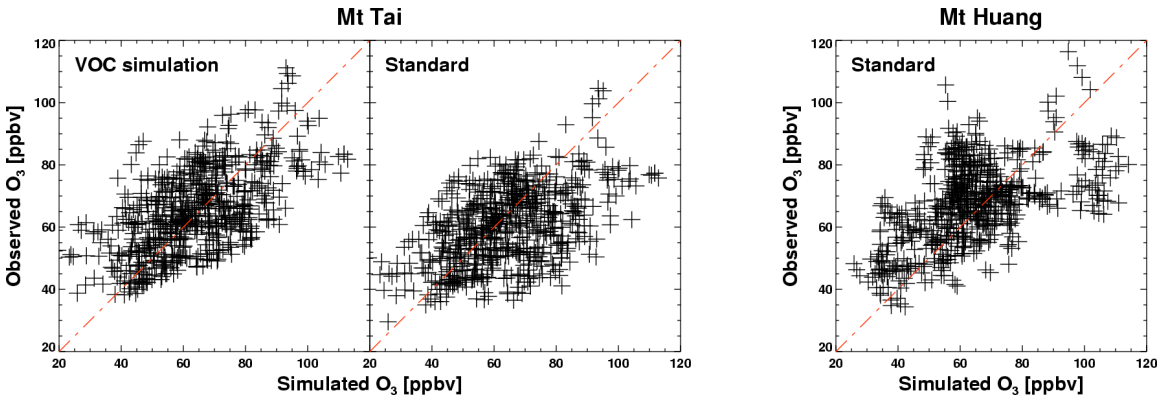

Figure C.2 Observed and simulated hourly ozone concentrations from the measurements and REAM simulations at Mt. Tai and Huang for May 2004. Simulated ozone concentrations in the VOC simulation at Mt. Huang are similar to the standard simulation. The ozone measurements were previously published by Z. Wang et al. [2006].

Table C.1 Statistics of model performance evaluation for hourly ozone for May 2004

		N_Obs[1]	Obs_Mean[1] (ppbv)	Sim_Mean[1] (ppbv)	Mean_Bias[1] (ppbv)	Mean_Error[1] (ppbv)	R[1]	MNB %	MNGE %	APPA %
Mt.Tai	VOC[2]	648	63.74	63.77	0.03	11.41	0.59	4.44	19.96	-6.58
	STD[2]			58.93	-4.82	12.53	0.49	-3.13	20.39	-15.59
Mt.Huang	VOC	648	63.99	66.52	2.53	12.85	0.53	8.48	21.15	2.99
	STD			66.02	2.01	12.65	0.53	7.49	20.60	2.40

[1] N_Obs denotes the number of observations. Obs_Mean denotes the observed mean. Sim_Mean denotes the simulated mean. Mean_Bias denotes the mean of the bias of the model simulations. Mean_Error denotes the mean of the absolute bias of the model simulations. R denotes the correlation coefficient.

[2] VOC denotes the VOC simulations. STD denotes the standard simulations.

Three statistical measures recommended by the U.S. EPA [US EPA] are used here, Mean Normalized Bias (MNB), Mean Normalized Gross Error (MNGE), and Average Peak Prediction Accuracy (APPA) (Table C.1). The REAM model errors for ozone simulations are within the EPA recommended criteria of ±15, ±30, and ±20% for MNB, MNGE, and APPA, respectively. Model shows good performance in simulating the ozone peaks during the episodes. The standard model tends to have a low bias at Mt. Tai. The VOC simulation improves the model performance at Mt. Tai. The mean bias is reduced from -4.82 to 0.03 ppbv and the APPA is improved from -15.59% to -6.58%.

C.3 Assessment of the impact of MGLY emissions on model simulations

Figure C.3a shows the difference of simulated surface MDA8 O_3 concentrations over China between the VOC and standard simulations for June 9-14, 2004. The change of the ozone concentration over the most regions of East China is < 10 ppbv, except for the VOC-sensitive areas such as the vicinity of Beijing where the ozone enhancement reaches 10-15 ppbv. Among the three mountain sites, only Mt. Tai locates in the regions with ozone enhancement of 10-15 ppbv. Figure C.3b shows the simulated mean daytime ratios of CH_2O/NO_y for June 2004 over China in the standard simulation, which is similar to the VOC simulation result (Fig. 4.4).

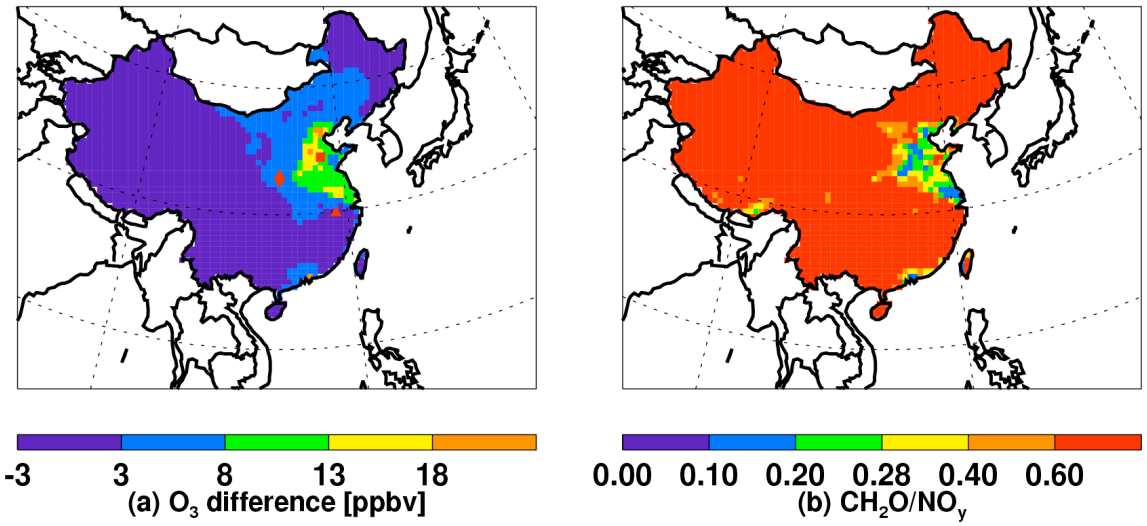

Figure C.3 (a) Changes of surface MDA8 O_3 concentrations over China for June 9-14, 2004 due to the added MGLY emissions. The red square, diamond, and triangle symbols represent the locations of Mt. Tai, Hua, and Huang, respectively. (b) Simulated mean daytime ratios of CH_2O/NO_y for June 2004 over China in the standard simulation.

REFERENCES

Allen, D. J., Pickering, K. E., Stenchikov, G., Thompson, A., and Kondo, Y.: A three-dimensional total odd nitrogen (NO_y) simulations during SONEX using a stretched-grid chemical transport model, *J. Geophys. Res.*, 105, 3851, doi: 10.1029/2002JD002066, 2000.

Allen, D. J. and Pickering, K. E.: Evaluation of lightning flash rate parameterizations for use in a global chemical transport model, *J. Geophys. Res.*, 107, 4711, doi:10.1029/2002JD002066, 2002.

Altshuller, A. P. Measurements of the products of atmospheric photochemical reactions in laboratory studies and in ambient air-relationships between ozone and other products. *Atmos. Env.*, 17, 2383-2427, 1983.

Beer, R., Glbavich, T.A., and Rider, D.M.: Tropospheric emission spectrometer for the Earth Observing System's Aura satellite, Appl. Opt., 40, 2356–2367, 2001.

Beer, R. and TES on the Aura Mission: Scientific objectives, measurements and analysis over view, IEEE Trans. Geosci. Remote. Sens., 44, 1102–1105, 2006.

Benkovitz, C. M., et al.: Global gridded inventories for anthropogenic emissions of sulfur and nitrogen, J. Geophys. Res., 101, 29239-29253, 1996.

Bertram, T. H., Perring, A. E., Wooldridge, P. J., Crounse, J. D., Kwan, A. J., Wennberg, P. O., Scheuer, E., Dibb, J., Avery, M., Sachse, G., Vay, S. A., Crawford, J. H., McNaughton, C. S., Clarke, A., Pickering, K. E., Fuelberg, H., Huey, G., Blake, D. R., Singh, H. B., Hall, S. R., Shetter, R. E., Fried, A., Heikes, B. G., and Cohen, R. C.: Direct Measurements of the Convective Recycling of the Upper Troposphere, *Science*, 315, 816-820, 2007.

Bey, I., Jacob, D. J., Yantosca, R. M., Logan, J. A., Field, B. D., Fiore, A. M., Li, Q., Liu, H., Mickley, L. J., and Schultz, M. G.: Global modeling of tropospheric chemistry with assimilated meteorology: Model description and evaluation, *J. Geophys. Res.*, 106, 23073-23096, 2001.

Boersma, K. F., et al.: Near-real time retrieval of tropospheric NO_2 from OMI, *Atmos. Chem. Phys.*, 7, 2103-2118, 2007.

Boersma, K. F., et al.: Validation of OMI tropospheric NO_2 observation during INTEX-B and application to constrain NO_x emissions over the eastern United States and Mexico, *Atmos. Environ.*, 42, 4480-4497, 2008.

Bucsela, E. J., et al.: Algorithm for NO_2 vertical Column Retrieval From the Ozone Monitoring Instrument, *IEEE Trans. Geo. Rem. Sens.*, 44(5), 1245-1258, Special Issue on the EOS Aura Mission, 2006.

Bucsela, E. J., et al.: Comparison of tropospheric NO_2 in situ aircraft measurements with near-real-time and standard product data from OMI, *J. Geophys. Res.*, 113, doi:10.1029/2007JD008838, 2008.

Choi, Y., Wang, Y., Zeng, T, Martin, R. V., Kurosu, T. P., and Chance, K.: Evidence of lightning NO_x and convective transport of pollutants in satellite observations over North America, *Geophys. Res. Lett.*, 32, doi:10.1029/2004GL021436, 2005.

Choi, Y., Wang, Y., Zeng, T., Cunnold, D., Yang, E., Martin, R., Chance, K., Thouret, V. and Edgerton, E.: Springtime transitions of NO_2, CO, and O_3 over North America: Model evaluation and analysis, *J. Geophys. Res.*, 113, D20311, doi:10.1029/2007JD009632, 2008a.

Choi, Y., Wang, Y., Yang, Q., Cunnold, D., Zeng, T., Shim, C., Luo, M., Eldering, A., Bucsela, E., and Gleanson, J.: Spring to summer northward migration of high O_3 over the western North Atlantic, *Geophys. Res. Lett.*, 35, L04818, doi:10.1029/2007GL032276, 2008b.

Collins, W. J., Derwent, R. G., Johnson, C. E., and Stevenson, D. S.: A comparison of two schemes for the convective transport of chemical species in a Lagrangian global chemistry model, *Q. J. R. Meteorol. Soc.*, 128, 991-1009, 2002.

Cooper, O. R., Stohl, A., Trainer, M., Thompson, A. M., Witte, J. C., Oltmans, S. J., Morris, G., Pickering, K. E., Crawford, J. H., Chen, G., Cohen, R. C., Bertram, T. H., Wooldridge, P., Perring, A., Brune, W. H., Merrill, J., Moody, J. L., Tarasick, D., Nedelec, P., Forbes, G., Newchurch, M. J., Schmidlin, F. J., Johnson, B. J., Turquety, S., Baughcum, S. L., Ren, X., Fehsenfeld, F. C., Meagher, J. F., Spichtinger, N., Brown, C. C., Mckeen, S. A., McDermid, I. S., and Leblanc, T.: Large upper tropospheric ozone enhancements above midlatitude North America

during summer: In situ evidence from the IONS and MOZAIC ozone measurement network, *J. Geophys. Res.*, 111, doi:10.1029/2006JD007306, 2006.

Deeter, M., Emmons, L., Francis, G., Edwards, D., Gille, J., Warner, J., Khattatov, B., Ziskin, D., Lamarque, J., Ho, S., Yudin, V., Attie, J., Packman, D., Chen, J., Mao, D., and Drummond, J.: Operational carbon monoxide retrieval algorithm and selected results for the MOPITT instrument. J. Georphys. Res., 108, 4399, doi:10.1029/2002JD003186, 2003.

Ding, A., and T. Wang, Influence of stratosphere-to-troposphere exchange on the seasonal cycle of surface ozone at Mount Waliguanin, western China, Geophys. Res. Lett., 33, L03803, doi:10.1029/2005GL024760, 2006.

Ding, Y. and Chan, J.: The East Asian summer monsoon: an overview. Meteorol. Atmos. Phys., 89, 117-142, doi:10.1007/s00703-005-0125-z, 2005.

Doherty, R. M., Stevenson, D. S., Collins, W. J., and Sanderson, M. G.: Influence of convective transport on tropospheric ozone and its precursors in a chemistry-climate model, *Atmos. Chem. Phys.*, 5, 3205-3218, 2005.

Emanuel, K.A.: Atmospheric convection, Oxford University Press (New York), 580 pp, 1994.

Fehsenfeld, F. C., Ancellet, G., Bates, T. S., Goldstain, A. H., Hardesty, R. M., Honrath, R., Law, K. S., Lewis, A. C., Leaitch, R., McKeen, S., Meagher, J., Parrish, D. D., Pszenny, A. A. P., Russel, P. B., Schlager, H., Seinfeld, J., Trainer, M., Talbot, R., and Zbinden, R.: International Consortium for Atmospheric Research on Transport and Transformation (ICARTT): North America to Europe: Overview of the 2004 summer field study, *J. Geophys. Res.*, 111, doi:10.1029/2006JD007829, 2006.

Folkins, I., Bernath, P., Boone, C., Donner, L. J., Eldering, A., Lesins, G., Martin, R. V., Sinnhuber, B. M., and Walker, K.: Testing convective parameterizations with tropical measurements of HNO_3, CO, H_2O, and O_3: Implications for the water vapor budget, *Geophys. Res. Lett.*, 111, doi:10.1029/2006JD007325, 2006.

Fu, R., Hu, Y., Wright, J., Jiang, J., Dickinson, R., Chen, M., Filipiak, M., Read, W., Waters, J., and Wu, D. (2006): Short circuit of water vapor and polluted air to the global stratosphere by convective transport over the Tibetan Plateau. Proceeding of the National Academy of Sciences of the United States of America, 103, 5664-5669, 2006.

Fu, T.-M.; Jacob, D. J.; Wittrock, F.; Burrows, J. P.; Vrekoussis, M. Global budgets of atmospheric glyoxal and methylglyoxal, and implications for formation of secondary organic aerosols. *J. Geophys. Res.,* 113, D15303, 2008.

Gao, J., Wang, T., Ding, A., Liu, C.: Observational study of ozone and carbon monoxide at the summit of mount Tai (1534 m a.s.l.) in central-eastern China. Atmos. Env., 39, 4779-4791, 2005.

Granier, C., J.F. Lamarque, A. Mieville, J.F. Muller, J. Olivier, J. Orlando, J. Peters, G. Petron, G. Tyndall, S. Wallens (2005): POET, a database of surface emissions of ozone precursors, available online at http://www.aero.jussieu.fr/projet/ACCENT/POET.php.

Grell, G. A.: Prognostic evaluation of assumptions used by cumulus parameterizations, *Mon. Weather Rev.*, 121, 764-787, 1993.

Grell, G. A.: A description of the fifth-generation Penn State/NCAR mesoscale model (MM5), *NCAR Tech. Note*, June, 1995.

Grell, G. A. And Devenyi, D.: A generalized approach to parameterizing convection combining ensemble and data assimilation techniques, *Geophys. Res. Lett.*, 29, doi: 10.1029/2002GL015311, 2002.

Grewe, V., Brunner, D., Dameris, M., Grenfell, J. L., Hein, R., Shindell, D., and Staehelin, J.: Origin and variability of upper tropospheric nitrogen oxides and ozone at northern mid-latitudes, *Atmos. Envir.*, 35, 3421-3433, 2001.

Guillas, S., Bao, J., Choi, Y., Wang, Y., Khaing, H., Nesbit, C., and Huey, G.: downscaling of chemical transport ozone forecasts over Atlanta, *Atmos. Environ.*, 42, 1338-1348, 2008.

He, Y., Uno, I., Wang, Z., Pchanart, P., Li, J., and Akimoto, H.: Significant impact of the East Asia monsoon on ozone seasonal behavior in the boundary layer of Eastern China and the west Pacific region. Atmos. Chem. Phys., 8, 7543-7555, 2008.

Herman, J. R. and Celarier, E. A. Earth surface reflectivity climatology at 340-380 nm from TOMS data, *J. Geophys. Res.*, 102, 28003-28011, 1997.

Hess, P.G.: A comparison of two paradigms: The relative global roles of moist convective versus nonconvective transport, *J. Geophys. Res.*, 110, doi:10.1029/2004JD005456, 2005.

Hoskins, B. J. and Rodwell, M. J.: A model of the Asian summer monsoon 1. The global-scale. J. Atmos. Sci., 52, 1329-1340, 1995.

Huang, G.: An index measuring the interannual variation of the East Asian summer monsoon-The EAP index. Adv. Atmos. Sci., 21, 41-52, 2004.

Hudman, R. C., Jacob, D. J., Turquety, S., Leibensperger, E. M., Murray, L. T., Wu, S., Gilliland, A. B., Avery, M., Bertram, T. H., Brune, W., Cohen, R. C., Dibb, J. E., Flocke, F. M., Fried, A., Holloway, J., Neuman, J. A., Orville, R., Perring, A., Ren, X., Ryerson, T. B., Sachse, G. W., Singh, H. B., Swanson, A., and Wooldridge, P. J.: Surface and lightning sources of nitrogen oxides over the United States: magnitudes, chemical evolution, and outflow, *J. Geophys. Res.*, 112, doi:10.1029/2006JD007912, 2007.

Huffman, G.J., Adler, R.F., Morrissey, M., Bolvin, D.T., Curtis, S., Joyce, R., McGavock, B., Susskind, J.: Global Precipitation at One-Degree Daily Resolution from Multi-Satellite Observations. J. Hydrometeor., 2, 36-50, 2001.

Intergovernmental Panel on Climate Change: IPCC FOURTH ASSESSMENTREPORT: CLIMATE CHANGE 2007. Available at http://www.ipcc.ch/ipccreports/assessments-reports.htm.

Jiang, J, Livesey, N, Su, H., Neary, L., McConnell, J., and Richards, N.: Connecting surface emissions, convective uplifting, and long-range transport of carbon monoxide in the upper troposphere: New observations from the Aura Microwave Limb Sounder. Georphys. Res. Lett., 34, L18812, doi:10.1029/2007GL030638, 2007.

Jing, P., Cunnold, D., Choi, Y., and Wang, Y.: Summertime tropospheric ozone columns from Aura OMI/MLS measurements versus regional model results over the United States, *Geophys. Res. Lett.*, 33, doi:10.1029/2006GL026473, 2006.

Jones, D. B. A., Bowman, K. W., Palmer, P. I., Worden, J., Jacob, D., Hoffman, R., Bey, I., Yantosca, R.: Potential of observations from the Tropospheric Emission Spectrometer to continental sources of carbon monoxide, J. Geophys. Res., 108(D24), 4789, doi: 10.1029/2003JD003702, 2003.

Jourdain, L., Worden, H. M., Worden, J. R., Bowman, K., Li, Q., Eldering, A., Kulawik, S., Osterman, G., Boersma, K., Fisher, B., Rinsland, C., Beer, R., and Gunson, M.: Tropospheric vertical distribution of tropical Atlantic ozone observed by TES during the northern African biomass burning season, Geophys. Res. Lett., 34, L04810, doi:10.1029/2006GL028284, 2007.

Kain, J. S.: The Kain-Fritsch Convective Parameterization: An Update, *J. Appl. Meteo.*, 43, 2003.

Kaufman, Y. J., et al. (1998): Potential global fire monitoring from EOS-MODIS, *J. Geophys. Res.*, 103, 32215-32238.

Kiley, C. M. and Fuelberg, H. E.: An examination of summertime cyclone transport processes during Intercontinental Chemical Transport Experiment (INTEX-NA), *J. Geophys. Res*., 111, doi:10.1029/2006JD007115, 2006.

Kumar, S.; Chock, D. P. An update on oxidant trends in the south coarse air basin of California. *Atmos. Env.*, 18, 2131-2134, 1984.

Labrador, L., Kuhlmann, R. V., and Lawrence, M. G.: Strong sensitivity of the global mean OH concentration and the troposphere's oxidizing efficiency to the source of NO_x from lightning, *Geophys. Res. Lett.*, 31, doi:10.1029/2003GL019229, 2004.

Labrador, L. J., Kuhlmann, R. V., and Lawrence, M. G.: The effects of lightning-produced NO_x and its vertical distribution on atmospheric chemistry: sensitivity simulations with MATCH-MPIC, *Atmos. Chem. Phys.*, 5, 1815-1834, 2005.

Lam, K. S.; Wang, T. J.; Chan, L. Y.; Wang, T.; Harris, J. Flow patterns influencing the seasonal behavior of surface ozone and carbon monoxide at a coastal site near Hong Kong. *Atmos. Env.*, 35, 3121-3135, 2001.

Lamarque, J. F., Brasseur, G. P., and Hess, P. G.: Three-dimentional study of the relative contributions of the different nitrogen sources in the troposphere, *J. Geophys. Res.*, 101, 22,955-22,968, 1996.

Lamsal, L. N., et al.: Ground-level nitrogen dioxide concentrations inferred from the satellite-borne Ozone Monitoring Instrument, *J. Geophys. Res.*, 113, doi:10.1029/2007JD009235, 2008.

Levy, H., Moxim, W. J., Klonecki, A. A., and Kasibhatla, P. S.: Simulated tropospheric NO_x: Its evaluation, global distribution and individual source contributions, *J. Geophys. Res.*, 104, 26,279-26,306, 1999.

Li, J. and Zeng, Q.: A unified monsoon index. Geophys. Res. Lett., 29, 1274, doi:10.1029/2001GL013874, 2002.

Li, J., Wang, Z., Akimoto, H., Gao, C., Pochanart, P., and Wang, X.: Modeling study of ozone seasonal cycle in lower troposphere over East Asia. J. Geophys. Res., 112, D22S25, doi:10.1029/2006JD008209, 2007.

Li, Q., Jacob, D. J., Park, R., Wang, Y., Heald, C. L., and Hudman, R.: North American pollution outflow and the trapping of convectively lifted pollution by upper-level anticyclone, *J. Geophys. Res.*, 110, doi:10.1029/2004JD005039, 2005.

Ma, J. and Liu, H.: Summertime tropospheric ozone over China simulated with a regional chemical transport model: 1. Model description and evaluation. J. Geophy. Res., 107, doi:10.1029/2001JD001354, 2002.

Ma, J., et al.: Comparison of model-simulated tropospheric NO_2 over China with GOME-satellite data, *Atmos. Env.*, 40, 593-604, 2006.

Martin, R. V., et al.: Global inventory of nitrogen oxide emissions constrained by space-based observations of NO_2 columns, *J. Geophys. Res.*, 108, doi:10.1029/2003JD003453, 2003.

Martin, R. V., Sioris, C. E., Chance, K., Ryerson, T. B., Bertram, T. H., Wooldridge, P. J., Cohen, R. C., Neuman, J. A., Swanson, A., and Flocke, F. M.: Evaluation of space-based constraints on global nitrogen oxide emissions with regional aircraft measurements over and downwind of eastern North America, *J. Geophys. Res.*, 111, doi:10.1029/2005JD006680, 2006.

Martin, R. V., Sauvage, B., Folkins, I., Sioris, C. E., Boone, C. Bernath, P., and Ziemke, J.: Space-based constraints on the production of nitric oxide by lightning, *J. Geophys. Res.*, 112, doi:10.1029/2006JD007831, 2007.

North American Research Strategy for Tropospheric Ozone (NARSTO), *An Assessment of Tropospheric Ozone Pollution - A North American Perspective* (2000). Available at http://www.narsto.org/section.src?SID=7.

Ott, L. E., Pickering, K., Stenchikov, G., Lin, R., Ridley, B., Lopez, J., Loewenstain, M., and Richard, E.: Trace gas transport and lightning NO_x production during a CRYSTAL-FACE thunderstorm simulated using a 3-D cloud-scale chemical transport model, *Eos Trans. AGU, 84(46)*, Fall Meet. Suppl., Abstract AE32A-0156, 2003.

Park, M., Randel, W, Gettelman, A., Massie, S., Jiang, J.: Transport above the Asian summer monsoon anticyclone inferred from Aura Microwave Limb Sounder tracers. J. Geophys. Res., 112, D16309, doi:10.1029/2006JD008294, 2007.

Pickering, K. E., Wang, Y., Tao, W., Price, C., and Muller, J.: Vertical distributions of lightning NO_x for use in regional and global chemical transport models, *J. Geophys. Res.*, 103, 31202-31216, 1998.

Prather, M. J. and Jacob, D. J.: A persistent imbalance in HO_x and NO_x photochemistry of the upper troposphere driven by deep tropical convection, *Geophys. Res. Lett.*, 24, 3189-3192, 1997.

Prather, M. J.: Atmospheric Chemistry and Greenhouse Gases, in: Climate Change 2001: The Scientific Basis, Contribution of WG1 to the Third Assessment report of the IPCC, edited by: *Houghton, J. T., et al., Cambridge University Press, England*, 2001.

Price, C. and Rind, D.: What determines the cloud-to-ground lightning fraction in thunderstorms? *J. Geophys. Res.*, 98, 463-466, 1993.

Price, C., Penner, J., and Prather, M.: NO_x from lightning: 1. global distribution based on lightning physics, *J. Geophys. Res.*, 102, 5929-5941, 1997.

Randel, W. and Park, M.: Deep convective influence on the Asian summer monsoon anticyclone and associated tracer variability observed with Atmospheric Infrared Sounder (AIRS). J. Geophys. Res., 111, D12314, doi:10.1029/2005JD006490, 2006.

Randerson, J. T., Van der Werf G. R., Giglio, L., Collatz, G. J., Kasibhatla., P. S.: Global Fire Emissions Database, Version 2 (GFEDv2.1). Available at http://daac.ornl.gov/ from Oak Ridge National Laboratory Distributed Active Archive Center, Oak Ridge, Tennesse, U.S.A. doi:10.3334/ORNLDAAC/849.

Richter, A., Burrows, J. P., Nub, H., Granier, C., Niemeier, U.: Increase in tropospheric nitrogen dioxide over China observed from space. *Nature*, 437, doi:10.1038/nature04092, 2005.

Rodwell, M. J. and Hoskins, B. J.: Subtropical anticyclones and summer monsoons. J. Climate, 14, 3192-3211, 2001.

Rossow, R. W. and Schiffer, R. A.: ISCCP cloud data products, *Bull. Am. Meteorol. Soc.*, 72, 2-20, 1991.

Sillman, S. The use of NO_y, H_2O_2, and HNO_3 as indicators for ozone-NOx-hydrocarbon sensitivity in urban locations. *J. Geophys. Res.*, 100, 14175-14188, 1995.

Singh, H. B., Brune, W. H., Crawford, J. H., Jacob, D. J., and Russell, P. B.: Overview of the summer 2004 Intercontinental Chemical Transport Experiment-North America (INTEX-NA), *J. Geophys. Res.*, 111, doi:10.1029/2006JD007905, 2006.

Singh, H. B., Salas, L., Herlth, D., Kolyer, R., Czech, E., Avery, M., Crawford, J. H., Pierce, R. B., Sachse, G. W., Blake, D. R., Cohen, R. C., Bertram, T. H., Perring, A., Wooldridge, P. J., Dibb, J., Huey, G., Hudman, R. C., Turquety, S., Emmons, L. K., Flocke, F., Tang, Y., Carmichael, G. R., and Horowitz, L. W.: Reactive nitrogen distribution and partitioning in the North American troposphere and lowermost stratosphere, *J. Geophys. Res.*, 111, doi:10.1029/2006JD007664, 2007.

Skamarock, W. C., Klemp, J. B., Dudhia, J., Gill, D. O., Barker, D. M., Wang, W., and Powers, J. G.: A Description of the Advanced Research WRF Version 2, *NCAR Tech. Note*, June, 2005.

Stauffer, D. R.; Seaman, N. L.; Binkowski, F. S. Use of four-dimensional data assimilation in a limited-area mesoscale model part II: effects of data assimilation within the planetary boundary layer. Mon. Weather Rev., 119, 734-754, 1991.

Stavrakou, T., et al.: Assessing the distribution and growth rates of NOx emission sources by inverting a 10-year record of NO2 satellite columns, *Geophys. Res. Lett.*, 35, doi:10.1029/2008GL033521, 2008.

Stephens, G. L.; Paltridge, G. W.; Platt, C. M. R. Radiation profiles in extended water clouds III: observations. *J. Atmos. Sci.*, 35, 2133-2141, 1978.

Streets, D. G. and Waldhoff, S. T.: Present and future emissions of air pollutants in China: SO_2, NO_x, and CO. *Atmos. Env.*, 34, 363-374, 2000.

Streets, D. G., Bond, T. C., Carmichael, G. R., Fernandes, S. D., Fu, Q., He, D., Klimont, Z., Nelson, S. M., Tsai, N. Y., Wang, M. Q., Woo, J.-H, Yarber, K. F.: An inventory of gaseous and primary aerosol emissions in Asia in the year 2000. *J. Geophy. Res.*, 108, doi:10.1029/2002JD003093, 2003.

Tanimoto, H., Sawa, Y., Matsueda, H., Uno, I., Ohara, T., Yamaji, K., Kurokawa, J., and Yonemura, S.: Significant latitudinal gradient in the surface ozone spring maximum over East Asia, Geophys. Res. Lett., 32, L21805, doi:10.1029/2005GL023514, 2005.

Tie, X., Zhang, R., Guy, Brasseur, Emmons, L. K., and Lei, W.: Effects of lightning on reactive nitrogen and nitrogen reservoir species in the troposphere, *J. Geophy. Res.*, 106, 3167-3178, 2001.

Tie, X.; Chandra, S.; Ziemke, J. R.; Granier, C.; Brasseur, G. P. Satellite Measurements of Tropospheric Column O_3 and NO_2 in Eastern and Southeastern Asia: Comparison with a Global Model (MOZART-2). *J. Atmos. Chem.*, 56, 105-125, 2007.

Turquety, S., Logan, J. A., Jacob, D. J., Hudman, R. C., Leung, F. Y., Heald, C. L., Yantosca, R. M., Wu, S., and Emmons, L. K.: Inventory of boreal fire emissions for North America in 2004: Importance of peat burning and pyroconvective injection, *J. Geophys. Res.*, 112, doi:10.1029/2006JD007281, 2007.

U.S. EPA, *Analysis in attainment demonstrations for guidance on the use of models and other the 8-hour ozone NAAQS.* Draft Final Report, EPA-454/R-99-004, 2005.

Walcek, C. J. Minor flux adjustment near mixing ratio extremes for simplified yet highly accurate monotonic calculation of tracer advection. *J. Geophys. Res.*, 105, 9335-9348, 2000.

Wang, B. and Lin, H.: Rainy season of the Asian-Pacific summer monsoon. *J Climate*, 15, 386-396, 2002.

Wang, H., Zhou, L., Tang, X.: Ozone concentrations in rural regions of the Yangtze Delta in China. *J. Atmos. Chem.*, 54, 255-265, 2006.

Wang, T., Wong, H., Tang, J., Ding, A., Wu, W., and Zhang, X.: On the origin of surface ozone and reactive nitrogen observed at a remote mountain site in the northerastern Qinghai-Tibetan Plateau, western China. J. Geophys. Res., 111, D08303, doi:10.1029/2005JD006527, 2006.

Wang, Y., Jacob, D. J., and Logan, J. A.: Global simulation of tropospheric O_3-NO_x-hydrocarbon chemistry: 1. Formulation, *J. Geophys. Res*., 103, 10713-10725, 1998.

Wang, Y., Liu, S. C., Yu, H., and Sandholm, S. T.: Influence of convection and biomass burning on tropospheric chemistry over the tropical Pacific, J. Geophys. Res., 105, 9,321-9,333, 2000.

Wang, Y., Liu, S. C., Wine, P. H., Davis, D. D., Sandholm, S. T., Atlas, E. L, Avery, M. A., Blake, D. R., Blake, N. J., Brune, W. H., Heikes, B. G., Sachse, G. W., Shetter, R. E., Singh, H. B., Talbot, R. W., and Tan, D.: Factors controlling tropospheric O_3, OH, NO_x, and SO_2 over the tropical Pacific during PEM-Tropics B, *J. Geophys. Res*., 106, 32,733-32,747, 2001.

Wang, Y., Choi, Y., Zeng, T., Ridley, B., Blake, N., Blake, D., and Flocke, F.: Late-spring increase of trans-Pacific pollution transport in the upper troposphere, *Geophys. Res. Lett.*, 33, doi:10.1029/2005GL024975, 2006.

Wang, Y., Choi, Y., Zeng, T., Davis, D., Buhr, M., Huey, G., and Neff, W.: Assessing the photochemical impact of snow NO_x emissions over Antarctica during ANTCI 2003, *Atmos. Environ.*, 41, 3944-3958, 2007.

Wang, Y.X., et al.: Seasonal variability of NO_x emissions over east China constrained by satellite observations: Implications for combustion and microbial sources, *J. Geophys. Res.*, 112, doil:10.1029/2006JD007538, 2007.

Wang, Z., Li, J., Wang, X., Pochanart, P., Akimoto, H.: Modeling of Regional High Ozone Episode Observed at Two Mountain Sites (Mt. Tai and Huang) in East China. J. Atmos. Chem., 55, 253-272, 2006.

Wei, F., Teng, E., Wu, G., Hu, W., Wilson, W., Chapman, R., Pau, J., and Zhang, J.: Ambient concentrations and elemental compositions of PM_{10} and $PM_{2.5}$ in four Chinese cities. Environ. Sci. Tech., 33(23), 4188-4193, 1999.

Worden, H., Logan, J. A., Worden, J. R., Beer, R., Bowman, K., et al.: Comparisons of Tropospheric Emission Spectrometer (TES) ozone profiles to ozonesodes: methods and initial results, J. Geophys. Res., 112, D03309, doi:10.1029/2006JD007258, 2007.

Yang, Q., Cunnold, D, Wang, H, Froidevaux, L., Claude, H., Merrill, J., Newchurch, M., and Oltmans, S.: Midlatitude tropospheric ozone columns derived from the Aura Ozone Monitoring Instrument and Microwave Limb Sounder measurements, J. Geophys. Res., 112, D20305, doi:10.1029/2007JD008528, 2007.

Yienger, J. J., et al.: Empirical model of global soil-biogenic NO_x emissions, *J. Geophys. Res.*, 100, 11447-11464, 1995.

Zeng, T., Wang, Y., Chance, K., Browell, E. V., Ridley, B. A., and Atlas, E. L.: Widespread persistent near-surface ozone depletion at northern high latitudes in spring, *Geophys. Res. Lett.*, 30(24), doi:10.1029/2003GL018587, 2003.

Zeng, T., Wang, Y., Chance, K., Blake, N., Blake, D., and Ridley, B.: Halogen-driven low altitude O_3 and hydrocarbon losses in spring at northern high latitudes, *J. Geophys. Res.*, 111, doi:10.1029/2005JD006706, 2006.

Zhu, B., Akimoto, H., Wang, Z., Sudo, K., Tang, J., and Uno, I.: Why does surface ozone peak in summertime at Waliguan? Geophys. Res. Lett., 31, L17104, doi:10.1029/2004GL020609, 2004.

Zhao, C.; Wang, Y.; Zeng, T.: East China plains: A “basin” of ozone pollution. Environ. Sci. Tech., In press, 2009a.

Zhao, C.; Wang, Y.; Choi, Y.; Zeng, T.: Impact of convective transport and lightning NOx production over North America: Dependence on cumulus parameterizations, Atmos. Chem. Phys. Discuss., 9, 2319-2380, 2009b.

Zhao, C. and Wang, Y.: Assimilated inversion of NOx emissions over East Asia using OMI NO2 column measurements. In press, Geophys. Res. Lett., 2009.

Zhang, L., Jacob, D. J., Bowman, K. W., and et al.: Ozone-CO correlations determined by the TES satellite instrument in continental outflow regions, Geophys. Res. Lett., 33, L18804, doi:10.1029/2006GL026399, 2006.

Zhang, Q., et al.: NO_x emission trends for China, 1995-2004: The view from the ground and the view from space, *J. Geophys. Res.*, 112, doi:10.1029/2007JD008684, 2007.

Zhang, Z., Chan, J., Ding, Y.: Characteristics, evolution and mechanisms of the summer monsoon onset over Southeast Asia. *Int. J. Climatol.* 24, 1461-1482, 2004.

VITA

CHUN ZHAO

Chun Zhao was born in Langxi, China in March 1983. He attended the University of Science and Technology of China (USTC) in 2001, where he received his bachelor degrees in both Atmospheric Science and Business Management in 2005. Right after he finished his undergraduate study, he jointed Dr. Yuhang Wang's research group at Georgia Institute of Technology to start a Ph.D. program in Atmospheric Chemistry in August 2005. During that period, his studies have concentrated on the development and application of chemical transport models.